Università degli Studi di
Trento

Dipartimento di Fisica

Thesis submitted to the
Doctoral School in Physics – XXIX cycle
by

Simone Serafini

in candidature for the degree of

Philosophiae Doctor – Dottore di Ricerca

Dynamics of Vortices and their Interactions in Bose-Einstein Condensates

Supervisor: prof. Gabriele Ferrari

Referees: prof. Frédéric Chevy and prof. Nicholas G. Parker

Dynamics of Vortices and their Interactions in Bose-Einstein Condensates

Simone Serafini

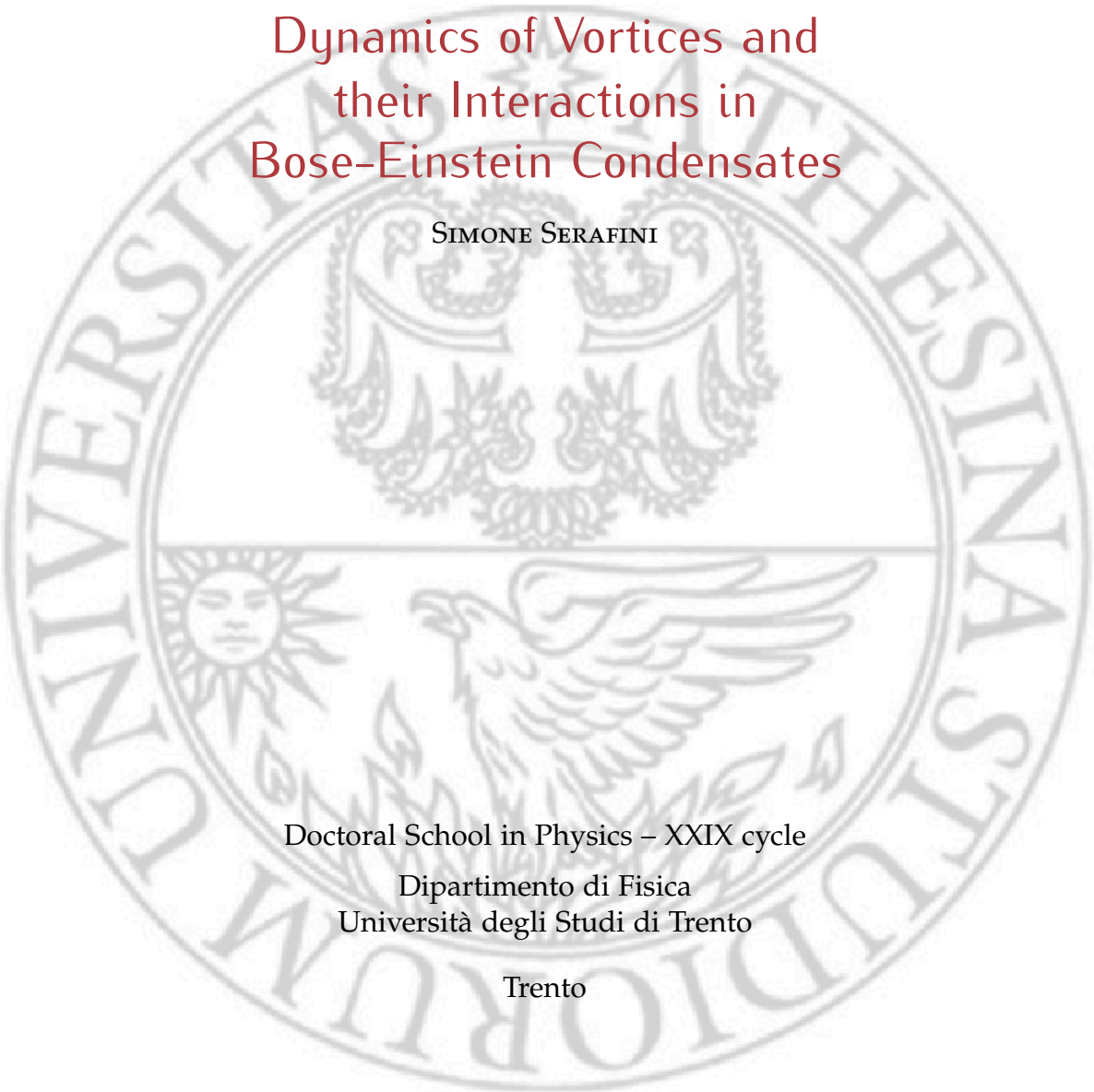

Doctoral School in Physics – XXIX cycle

Dipartimento di Fisica
Università degli Studi di Trento

Trento

Simone Serafini: *Dynamics of Vortices and their Interactions in Bose-Einstein Condensates*
Thesis Doctoral School in Physics – XXIX cycle,

SUPERVISOR:
prof. Gabriele Ferrari
REFEREES:
prof. Frédéric Chevy
prof. Nicholas G. Parker

Trento

a.a. 2015/2016

ai miei genitori,
alla mia nonna,
a Viola

CONTENTS

INTRODUCTION

The topic of the present thesis concerns vortex physics in Bose-Einstein condensates. Vortices play a central role in many phenomena both in quantum and in classical regime, so that the study of both have to learn something from the other. Vortices in fluid motion were observed since ancient time, but their first description in the context of ideal fluids was given by Helmholtz and Kelvin in the second half of XIX century. A first golden age of vorticity appears during the first years of XX century, when the first airplanes were built and aerodynamics became a central discipline in engineering, the role of vortices is indeed fundamental for understanding the physics of planes. A second golden age took place when turbulent systems became the subject of intense research since the second half of XX century.

The main drawback of studying classical turbulence is the high complexity of the equation describing the fluid motion. A turbulent fluid is far from the ideal and tractable situations. The chemistry Nobel laureate sir Cyril Hinshelwood, indeed, observed that "... fluid dynamicists were divided into hydraulic engineers who observed what could not be explained, and mathematicians who explained things that could not be observed." (Lighthill 1956). But actually there is a physical situation where the model of an ideal irrotational compressible isentropic fluid is a suitable description. Such a situation is the case of a *superfluid*, which is a purely quantum situation. Surprisingly in the field of vorticity the quantum case is simpler than the classical one. Superfluidity was observed by Kapitza 1938 and Allen et al. 1938, who showed that helium can flow without viscosity below a critical temperature. Superfluidity and superconductivity represent the main puzzles for the physicists in the first half of XX century.

Macroscopic quantum physics: BECs

The developement of quantum mechanics during the past century poses a huge number of puzzles and weird effects, whose interpretation and understanding is often counterintuitive and paradoxical. One of these weird behaviours was Bose-Einstein Condensation, theoretically discovered by Bose and Einstein in 1924, which occurs when the effects of quantum statistics plays a major role in the description of a system, revealing the fact that at a sufficiently low temperature all the particles of a Bose gas or liquid occupy the lowest energy level, sharing the same wavefunction: *a system composed by a macroscopic number of particles behave, when its energy is sufficiently low, as a giant unique matter wave*. BEC was proposed to play a key role in weird behaviour systems like superconductivity and superfluidity, which are not at all interpretable in the framework of classical physics. For about seventy years BEC remained just a useful model for theories,

because of the difficulty to achieve, manipulate and probe this phenomenon in a clean system. The possibility to observe directly and clearly Bose-Einstein condensation implies to access to quantum mechanical effects on a macroscopic scale, thus the possibility to have a unique testbed for the whole framework of quantum physics, which is the foundation for the whole XX century physics. This possibility became reality in 1995 when BEC condensation was experimentally achieved in a dilute gas of neutral atoms thanks to the impressive development of laser cooling and trapping techniques in the last thirty years of XX century. BEC is possible in a gas of neutral atoms gas as a metastable state, playing on the interplay of particle density n and temperature T that define the *quanticity* of a system, *i.e.* the *phase-space density*: $\mathcal{D} = n\lambda_T^3 \propto NT^{3/2}$, where $\lambda_T = \sqrt{2\pi\hbar^2/mk_BT}$ is the de Broglie wavelength.

Analogies and similarities across different physical systems and their descriptions are the most powerful and exciting tools in scientific research. Indeed Feynman, in his extraordinary lectures (R. Feynman et al. 1963), recognized the importance of analogies not only as a useful tool to access new physics, but also as the unique way in which the discovered physics can be learned and taught. Dealing with the traditional superfluids the theory of vortices in ideal fluids could be tested. Later, when BEC was achieved in atomic gases, thanks to the high degree of control on such systems, vorticity became an important research field of ultracold-matter physics.

The thesis

My thesis focuses on the experimental study of vortices in Bose-Einstein Condensates, with particular attention to the interaction processes between them. So far vortex-vortex interaction was studied in BECs either in rotating systems with the observation of regular Abrikosov lattices or in flat condensates across the Berezinskii-Kosterlitz-Thouless transition. In both cases the geometrical constraints allowed just a planar interaction among aligned or anti-aligned vortices.

The present study instead is carried out in an axisymmetric cigar-shaped BEC. This geometry is especially suitable for investigating vortex interactions. Indeed vortices are oriented perpendicularly to the BEC axis to minimize their length, hence energy, and, because of the cylindrical symmetry, the orientation of a vortex in the radial plane has no constraints. These facts permit interactions to occur with different incoming relative angles between the vortex lines and with different relative velocities. The strong confinement acting along the radial axis enhances also interesting effects due to the boundaries. Vortices in prolate structures are also known as *solitonic vortices* for the reason I will explain. Atomic BECs are particularly suited to study vorticity because of their tunability in terms of shape and dimensions, which are crucial to explore inhomogeneous superfluids in presence of boundaries. On the contrary, all the length scales are fixed by na-

ture in experiments on superfuid helium and investigations are carried on in a homogeneous regime.

Vortex reconnections and interactions play a fundamental role in the dynamics of fluids and turbulent flows, both in the classical and quantum regime. Studying vortices in a clean system like ultracold gases can therefore help, as a bottom-up approach, to understand the physics in a wider context, including superfluid helium, polariton condensates, fluid dynamics and turbulence, neutron stars and cosmological models.

The first part of the thesis provides an overview of the state-of-the-art in the field of vorticity in Bose-Einstein Condensates. I will introduce the phenomenon of BEC from a theoretical point of view, referring to its mean-field description through the Gross-Pitaevskii equation. Such a description is particularly suited for introducing the formalism of vortex physics because of its analogies with the equation of hydrodynamics. After that I will define the vortex as an excitation of a BEC which lies in the non-linear regime and has a topological nature.

In the second chapter I will give an overview on the actual experimental techniques developed for the investigation on vorticity in BECs. I will make a comparative description of the actual vortex production techniques, distinguishing between deterministic and stochastic ones. Then I will introduce the subject of vortex detection. Both the production and the imaging technique, taking also into account the geometry of the system, fix the range in which vortex physics can be studied.

The second part of the thesis is devoted to the description of the experiments I performed. The apparatus will be described focusing on the laser and the vacuum system. I will then describe the procedure to obtain BEC with a controlled average number of stochastic vortices. Imaging of stochastic vortices with the aim to probe their dynamics must be done through real-time and weakly-destructive techniques, thus I will firstly describe the application of a slightly modified known technique, which I call *Microwave-Pulse Minimally Destructive* (μw-PMD) imaging. This technique consists of the uniform coherent extraction of a small part of the condensate via μ-wave radiation into an untrapped state exploiting the non-degenerate Zeeman internal levels. The outcoupled atom cloud only is then resonantly imaged after a short expansion. These actions are repeated many times, removing each time the same small amount of atoms from the trapped condensate. This technique allows precise study on the dynamics of single vortices but is not optimal for studying vortex interactions. The main drawbacks of μw-PMD are: strong interaction of the outcoupled atoms with the original condensate, excitation of collective oscillation modes and a complete loss of information about the orientation of the nodal line in the radial plane. For this reason we

developed a new technique, named *Radiofrequency-Sweep Minimally Destructive* (rf-SMD) imaging. The rf-SMD exploits the effects of gravitational potential energy on the atomic levels to implement a resonant radiofrequency-transfer to a magnetically untrapped state. The transition to the new state affects atoms near a surface that crosses horizontally the condensate. Such a surface is then moved across the sample from the top to the bottom by chirping the radiofrequency in a finite time. The repetition of this action produces bunches of atoms that fall under the effect of gravity, in analogy to a pulsed atom laser. After some time of flight, atoms are resonantly imaged. The new technique permits to improve the frame rate and to reduce the perturbations on the trapped sample, but the most important feature is the possibility to extract information about the radial orientation of the vortex from the radially integrated absorption profile. This feature results from the interference of atoms extracted at different times because of the moving outcoupling surface; the interference also depends on the local direction of the superfluid velocity field with respect to the direction of the outcoupling surface. This effect is maximal for vortices aligned to the imaging axis and leads to an accumulation (higher density) or depletion (lower densities) of atoms in the falling atomic cloud.

In the last part of the thesis I will report the results of the experiments. The first result on which I report is the first experimental characterization of solitonic vortices. The solitonic vortex is the least energetic non-linear excitation allowed in the case of prolate geometries, hence having long lived existence. The solitonic part of this structure is given by its phase pattern, which shows a non-uniform gradient concentrated in a radial plane; far from the defect the phase is uniform. This structure for a vortex in a cigar-shaped BEC comes from the effect of boundaries. The characterization is performed through a simultaneous triaxial absorption imaging after a free expasion. Such a technique permits to highlight both the vortex nodal line, and the planar depletion characterizing the solitonic vortex. The planar depletion is due to the peculiar vortex phase pattern and it also brings information about the direction of the velocity field, which is translated in a Z- or S-shaped twist with a hollow core appearing in the density profile after the expansion. Such a relation was demonstrated theoretically, through a numerical simulation of the free expansion, and experimentally, through an interferometric technique. The interferometric technique consists of a coherent splitting of the condensate, then the two copies are overlapped, obtaining information on the phase pattern through a homodyne detection.

After the characterization of the "static" properties of the solitonic vortex, I report the characterization of its dynamical behaviour. A vortex in a cigar-shaped trap is expected to precess along an equipotential elliptic orbit. The period of motion is directly proportional to

the period of the axial harmonic potential and depends on the local chemical potential along the precession line $\mu_{\rm loc}(\chi) = (1-\chi^2)\mu$, where χ is the ratio of the maximum axial amplitude with the axial Thomas-Fermi radius and μ is the peak chemical potential, which depends on the atom number. We used the μw-PMD imaging technique and, exploiting the variable atom number in the condensate during the sampled period, we measured the dependence of the vortex oscillation period as a function of the amplitude of the oscillation and of the atom number, within the same experimental run.

After observing signatures of vortex interactions, we developed the new aforementioned rf-SMD technique. The application of such a technique leads to an impressive capability to observe vortex paths with a detailed resolution also in the vicinity of their intersection. In order to have a closer insight into vortex interactions the results of the experiments were compared to numerical simulations of interacting vortices; simulations were provided by Luca Galantucci and Carlo Barenghi from Newcastle University, with whom a collaboration on this topic was set. The cigar-shaped confinement suppresses the long-range part of the vortex-vortex interaction, that becomes thus appreciable only when the two vortices come at a relative distance of the order of the transverse Thomas-Fermi radius. When vortices are in the regime to feel each other, their dynamics is mainly determined by their relative entrance orientation and their individual entrance axial velocities. Single vortices are free to rotate in the radial plane because their energy does not depend on it. Thus, when two vortices approach, they tend to arrange themselves in the preferred anti-parallel configuration, favoured by energy conservation: a radial motion is then activated by interactions. The interplay between the axial precessional motion and the interaction-activated radial motion determines the outcome of the scattering. If the axial impact velocities are sufficiently high, the two vortices may reconnect, a phenomenon already observed numerically and experimentally. When instead the axial velocities are small, an unexpected behaviour appears: vortices tend to align in the anti-parallel configuration and bounce. This new behaviour happens because the radial motion makes the vortices to pass the radial centre of the condensate, reversing their axial motion because of the reversed velocity field induced by the inhomogeneous density imposed by the sample boundary. In an intermediate regime, simulations show the occurence of a double reconnection process; such a process was here observed for the first time in a dynamical simulation. The case of bouncing vortices is clearly pointed out by the experiment as non intersecting vortex trajectories. We study the dynamics of hundreds of different experimental realizations and we show the expected enhanced probability of rebound for the case of lower relative axial velocities and when vortices are anti-aligned just before the avoided intersection; this information is accessible thanks

to the novel imaging technique we developed. The visibility of the vortex trajectory is also an important information coming from the experiment because it is an indication of the vicinity of the vortex to the boundary. Indeed a statistical analysis shows that in cases of intersections concerning a fast vortex, *i.e.*, with a large amplitude, a dramatic change in visibility of one or both of the outcoming vortices is more likely. The combination of the information carried by all these signals, *i.e.*, the axial projection of the trajectory, the asymmetry of the vortex signal in the outcoupled bunch of atoms and its visibility, allows us to draw a clear picture of the dynamics occuring during the interaction.

To conclude some perspectives and improvements to the methodology will be discussed.

Part I

THEORETICAL BACKGROUND

In the first part of this thesis I will introduce the fundamentals of Bose-Einstein Condensation and its theoretical framework and then I will focus on the phenomenon of vorticity, both from a theoretical and experimental point of view, to describe the state of the art of its investigation.

1 VORTICITY IN BOSE-EINSTEIN CONDENSATES

CONTENTS

In the present chapter I will briefly introduce the phenomenon of Bose-Einstein Condensation and I will describe its simplest model, *i.e.*, the *mean-field approach*. Within this formalism it is possible to point out some analogies with classical hydrodynamics. The first part of the chapter is devoted to the description of the ground-state properties of a Bose-Einstein Condensate (BEC), the introduction of the *Thomas-Fermi limit* and to the definition of some important quantities like the *healing length* and the *chemical potential*. In the central part I will describe BEC excitations. Linear excitations, *phonons*, are briefly described in order to introduce, through the dispersion relation due to Bogoliubov (which derivation is not included), the concept of *superfluidity*. Then non-linear topological excitations are introduced showing in particular the role of vortices in this framework. Some general concepts regarding classical vortices and topology are addressed across the chapter. The properties of quantization of the vortex velocity field are derived in the last part of the chapter.

1.1 BOSE–EINSTEIN CONDENSATION

The Bose-Einstein Condensate is a particular phase of matter whose theoretical prediction dates back to 1924, when the Indian physicist Satyendra Nath Bose proposed a new derivation of Planck's law for black body radiation based on the maximization of the entropy of a gas of indistinguishable photons. Bose sent his work to Einstein, who generalized it to an ideal gas of indistinguishable atoms. When the temperature of a gas of bosonic particles is lowered, quantum effects become more and more evident. This concept is qualitatively depicted in the popular Ketterle's cartoon reported in figure 1.1 (from Ketterle, Durfee, et al. 1999). At high temperatures the

gas can be completely described with classical physics as an ensemble of "billiard balls". The "quanticity" of a system is measurable comparing the *de Broglie wavelength* λ_T of its constituents, which is inversely proportional to the square root of the temperature, with the characteristic length scales of the system, as the mean interparticle distance d and the range of the particle-particle interaction r_0. When $r_0 \ll \lambda_T \ll d$ the gas is still described by a Maxwell-Boltzmann distribution like a classical gas, but collisions have to be treated quantum-mechanically. When the temperature reaches a critical value T_c, the de Broglie wavelength becomes equal to the mean interparticle distance, leading to the overlap of the particles' matter waves, which now interfere strongly. When temperature goes below T_c, and hence $\lambda_T > d$, such an interference leads to the setting of a "giant matter wave" due to a constructive interference of all the waves describing particles in the groud state. The system below T_c starts to macroscopically occupy its ground state, hence populating the *Bose-Einstein Condensate* (BEC). In this regime all the particles behave as a single one because of the macroscopic occupation of the single-particle ground state. This effect is purely statistical, *i.e.*, it depends only on the quantum statistics of the constituents, and not on the interparticle interaction. Indeed condensation occurs also in ideal non-interacting gases.

BEC in nature

The phenomenon of Bose-Einstein condensation was proposed as being the fundamental mechanism occurring in many unexplained phenomena observed during the pioneering era of quantum mechanics, like supefluidity and superconductivity. Such effects are macroscopic but cannot be explained with classical concepts. Bose-Einstein condensation is also expected to appear in astrophysical objects like neutron stars (Migdal 1959). In the recent years also condensates of quasi-particles were proposed and observed, like excitons (Nikuni et al. 2000), magnons (Demokritov et al. 2013) and polaritons, reviewed in Carusotto et al. 2013. The most evident signature of Bose-Einstein condensation occurs in neutral atomic gases, first obtained in 1995 by M. H. Anderson et al. 1995 and K. B. Davis et al. 1995 thanks to the impressive improvements in the experimental techniques for atomic manipulation, like laser cooling, magnetic and optical trapping and the ability to control internal

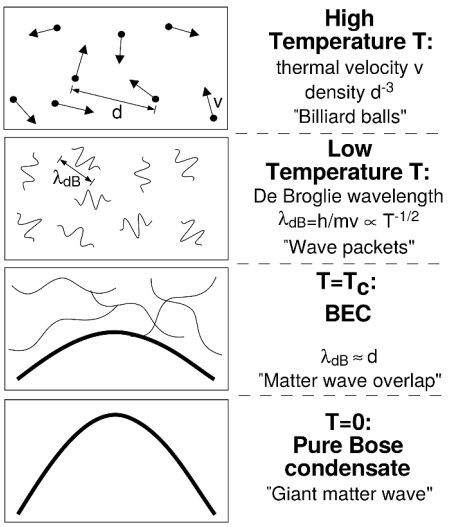

Figure 1.1: The popular Ketterle's cartoon sketching the BEC transition.

atomic states (a good overview is given in Cohen-Tannoudji et al. 2011). In the following I will consider only atomic gases, with which the experimets in this thesis are carried on. In chapter 3 I will describe the experimental procedure to obtain BEC in an atomic sample.

Atomic BECs in experiments

A very promising research area in the Bose-Einstein Condensation studies is the one which uses BECs to simulate complex quantum phenomena of condensed matter or even high-energy physics. Such an approach is called *quantum simulation*, and it was proposed originally by R. P. Feynman 1982. It exploits the high level of tunability and accessibility of atomic gases to map hamiltonians describing complex systems to a quantum hardware. At the end of an evolution time of such a quantum hardware, predictions regarding the complex system can be formulated scaling the results of a measure performed on the simulator. Many reviews on this topic exist and many experiments have been succesfully performed and many are proposed. A useful review is given by Georgescu et al. 2014, which treats also other quantum hardwares, and by Bloch, Dalibard, et al. 2012.

1.1.1 Mean-Field Description of a BEC

In the following I will focus on the case of an interacting atomic gas at $T = 0$, to which I will refer simply as Bose-Einstein Condensate. The case of an interacting gas is generally described through the mean-field description based on the *Gross-Pitaevskii equation* (GPE) (in the following sections I will refer to Cohen-Tannoudji et al. 2011, Dalfovo et al. 1999 and L. Pitaevskii et al. 2016). This description relies on a variational approach for calculating the condensate wave function starting from the non-interacting ground state of N bosons and including in the hamiltonian a two-body interaction term. The N-body wave function of non-interacting bosons is simply the product of N wave functions of the ground state of the trap $|\phi_0\rangle$:

$$|\psi\rangle = |\phi_0(1)\rangle \otimes |\phi_0(2)\rangle \otimes \cdots \otimes |\phi_0(N)\rangle.$$

The hamiltonian in the presence of interaction can be written in the following way:

$$H = \sum_{i=1}^{N} \left[\frac{\vec{p}_i^2}{2m} + V_t(\vec{r}_i) \right] + \frac{1}{2} \sum_i \sum_{j \neq i} V(\vec{r}_i - \vec{r}_j),$$

where a two-body interaction term V is added to the single-particle hamiltonian in the trap V_t. The variational approach consists in iteratively adjusting the starting wave function in order to minimize the energy functional

$$E_{tot}[\phi, N] = \langle H \rangle = \frac{\langle \psi | H | \psi \rangle}{\langle \psi | \psi \rangle}.$$

Minimization has to be performed with the constraint of the conservation of the norm of the wave function, hence of the number of particles. This can be done through the Lagrange multipliers method, yielding the following equality for the energy functional differentiation:

$$\delta(\langle\psi|H|\psi\rangle - \mu\langle\psi|\psi\rangle) = 0.$$

This approach leads to the following Schrödinger-like equation:

$$-\frac{\hbar^2}{2m}\nabla^2\phi(\vec{r}) + V_t(\vec{r})\phi(\vec{r}) + (N-1)\left[\int d^3r' V(\vec{r}-\vec{r}')|\phi(\vec{r}')|^2\right]\phi(\vec{r}) = \mu\phi(\vec{r}), \quad (1.1)$$

where the evolution of each atom is determined by the trapping potential and by the mean field in its position due to the other $N-1$ atoms. The interaction potential acts in the low-energy limit only through the lowest term in the partial wave expansion of the cross-section of the scattering process between two atoms. In this limit the cross-section for identical bosons is approximated as $\sigma_B \approx 8\pi a^2$, where the *s-wave scattering length* a is introduced[1]. The exact interaction potential is difficult to calculate, but because of the behaviour in the low-energy limit just described, it is convenient to introduce a *pseudo-potential* V_{pseudo}, easy to manipulate in calculations but reproducing the low-energy limit of the true potential. It can be shown that the contact potential

$$V_{\text{pseudo}}(\vec{r}-\vec{r}') = \frac{4\pi\hbar^2 a}{m}\delta(\vec{r}-\vec{r}') = g\delta(\vec{r}-\vec{r}') \quad (1.2)$$

reproduces the desired behaviour. In the following I will consider $V(\vec{r}-\vec{r}') = V_{\text{pseudo}}(\vec{r}-\vec{r}')$. The mean-field approach is valid only when the correlations between atoms at short distances can be neglected, hence the gas has to be dilute: $n|a|^3 \ll 1$, ensuring the applicability of the pseudo-potential approach. In this thesis I will consider only the case of repulsive interaction between the constituents, *i.e.*, $a > 0$.

Gross-Pitaevskii equation

With the assumption introduced above we obtain the so called *Gross-Pitaevskii equation* (GPE):

$$-\frac{\hbar^2}{2m}\nabla^2\phi(\vec{r}) + V_t(\vec{r})\phi(\vec{r}) + (N-1)g|\phi(\vec{r})|^2\phi(\vec{r}) = \mu\phi(\vec{r}). \quad (1.3)$$

Given the usual large atom number, the term $N-1$ can be replaced by N. One can show that the Lagrange multiplier μ is nothing else than the variation of the total energy when the number of particle varies by a unit, hence μ is the chemical potential.

1 a is the amplitude of the first term in the partial wave expansion of the scattering problem in the low-energy limit.

The healing length

The presence of repulsive atom-atom interactions introduces an important length scale, called *healing length*. This characteristic length can be seen as a "recovery" length of the condensate, *i.e.*, the distance in which the density goes from 0 to the local equilibrium value n; the healing length is indeed the characteristic size of vortices and solitons. The definition of the healing length is:

$$\xi = \sqrt{\frac{1}{8\pi n a}}, \tag{1.4}$$

derived balancing the kinetic and interaction energy.

Harmonic trapping

Usually a BEC is obtained in contactless traps (magnetic trap, optical trap), where the trapping force is linear with the displacement. The potential energy due to these kinds of traps is therefore harmonic and is characterized by the trapping frequencies along the coordinate directions $\omega_{x,y,z}/2\pi$:

$$V_t(x,y,z) = \frac{1}{2}m\omega_x^2 x^2 + \frac{1}{2}m\omega_y^2 y^2 + \frac{1}{2}m\omega_z^2 z^2. \tag{1.5}$$

The characteristic length is the *oscillator length* $a_{\text{ho}} = \sqrt{\hbar/m\tilde{\omega}}$, where $\tilde{\omega} = (\omega_x\,\omega_y\,\omega_z)^{1/3}$ is the geometrical mean of the trapping frequencies. In the following, harmonic confinement is assumed.

The Thomas-Fermi limit

When the contribution to the total energy coming from interactions is large with respect to the contribution from the kinetic energy, the GPE can be reduced to an algebraic equation:

$$V_t(\vec{r}) + Ng|\phi(\vec{r})|^2 = \mu. \tag{1.6}$$

This regime is known as *Thomas-Fermi* (TF) limit. One can show that this description is accurate to describe the BEC ground state when $N\,a/a_{ho} \gg 1$. From equation 1.6 one derives the spatial density of a trapped BEC $n(\vec{r}) = N|\phi(\vec{r})|^2$:

$$n(\vec{r}) = \frac{\mu - V_t(\vec{r})}{g}, \tag{1.7}$$

from which the shape of the confined condensate can be determined: for example in a harmonic confining potential the density profile has the shape of an inverted parabola up to the chemical potential, while it vanishes where the potential energy exceeds μ. Integrating the density profile and imposing the normalization, we obtain the chemical potential:

$$\mu = \frac{\hbar\tilde{\omega}}{2}\left(15\,\frac{N\,a}{a_{\text{ho}}}\right)^{2/5}; \tag{1.8}$$

the central density is therefore $n = \mu/g$. The size of the condensate is given by the *Thomas-Fermi radii*:

$$\mathscr{R}_{x,y,z} = \sqrt{\frac{2\mu}{m\omega_{x,y,z}}} \propto N^{1/5}. \tag{1.9}$$

The local chemical potential can be written as

$$\mu_{\text{loc}}(x,y,z) = \mu\left(1 - \frac{x^2}{\mathscr{R}_x^2} - \frac{y^2}{\mathscr{R}_y^2} - \frac{z^2}{\mathscr{R}_z^2}\right). \tag{1.10}$$

1.1.2 Time-dependent GPE and Hydrodynamic Analogue

The generalization to time-dependent problems of the GPE can be obtained through a generalized time-dependent Schrödinger equation:

$$i\hbar\frac{\partial}{\partial t}\phi(\vec{r},t) = -\frac{\hbar^2}{2m}\nabla^2\phi(\vec{r},t) + V_t(\vec{r},t)\phi(\vec{r},t) + Ng|\phi(\vec{r},t)|^2\phi(\vec{r},t). \tag{1.11}$$

If the trapping potential does not depend on time, the general solution to equation (1.11) can be found through the ansatz $\phi(\vec{r},t) = \phi(\vec{r})\exp(-i\mu t/\hbar)$, recovering in this way the stationary GPE for $\phi(\vec{r})$.

Hydrodynamic formulation

The treatment of the dynamics of a BEC through the time-dependent Gross-Pitaevskii equation can be interpreted in light of hydrodynamic equations. In the following I will consider the wavefunction to be normalized to the number of particles, $\int d^3r|\phi(\vec{r},t)|^2 = N$. With such a normalization the square modulus of the wavefunction gives directly the spatial density of the BEC $n(\vec{r},t) = |\phi(\vec{r},t)|^2$ and the GPE does no longer depend explicitly on N. The wavefunction can be rewritten in terms of its modulus and phase

$$\phi(\vec{r},t) = \sqrt{n(\vec{r},t)}\, e^{iS(\vec{r},t)}, \tag{1.12}$$

which is known as *Madelung transformation*. This representation of the wavefunction permits the immediate interpretation of the phase gradient in term of a simple physical quantity: indeed calculating the quantum current density $\vec{j} = \frac{\hbar}{2mi}(\phi^*\vec{\nabla}\phi - \phi\vec{\nabla}\phi^*)$ and interpreting it as a particle current density $\vec{j} = n\vec{v}$, one obtains the following relation between the velocity field and the phase gradient:

$$\vec{v}(\vec{r},t) = \frac{\hbar}{m}\vec{\nabla}S(\vec{r},t). \tag{1.13}$$

The GPE can be rewritten in the Madelung representation as two coupled equations for the density and the velocity field:

$$\frac{\partial}{\partial t}n + \vec{\nabla}\cdot(\vec{v}n) = 0 \tag{1.14a}$$

$$m\frac{\partial}{\partial t}\vec{v} = -\vec{\nabla}\left(V_t + gn - \frac{\hbar^2}{2m\sqrt{n}}\nabla^2\sqrt{n} + \frac{mv^2}{2}\right). \tag{1.14b}$$

Equation (1.14a) is analogous to the continuity equation for the flux of a fluid, while equation (1.14b) is an Euler-like equation for the evolution of its velocity field.

Quantum pressure

In the coupled equations (1.14) the only term containing explicitly $\hbar$ is called *quantum pressure*. Its physical meaning is strictly related to the Heisenberg uncertainity principle: where the density gradient is steeper the confinement is stronger, hence a broader kinetic energy is necessarily generated. Quantum pressure plays a central role in the physics of vortices, being the term responsible for the appearence of the healing length in BEC description. Such a length is the typical transverse dimension of a vortex line.

Hydrodynamics in Thomas-Fermi limit

In the time-dependent problem the Thomas-Fermi limit cannot be obtained simply neglecting the kinetic term in the Gross-Pitaevskii equation. Indeed, considering for example a ballistic expansion of the condensate, the kinetic energy term, which is small at the beginning, becomes rapidly dominant through the conversion of interaction energy into kinetic one. The TF limit is then obtained considering separately the contribution to kinetic energy given by the density gradient and by the phase gradient, respectively the last two terms in the right-hand side of equation (1.14b). For large values of $N\,a/a_{\mathrm{ho}}$ (TF limit), the quantum pressure term arising from the density gradient can be neglected, leading to the following hydrodynamic equations:

$$\frac{\partial}{\partial t} n + \vec{\nabla} \cdot (\vec{v} n) = 0 \tag{1.15a}$$

$$m \frac{\partial}{\partial t} \vec{v} = \vec{\nabla} \left(-\frac{m v^2}{2} - V_t - g n \right). \tag{1.15b}$$

The first one is the same continuity equation as before, while the Euler-like equation does no longer show any quantum term (no terms depend explicitly on Planck constant). Equations (1.15) describe the motion of a trapped BEC as the motion of a fluid in a trapping potential and in a pressure field due to the density of the other particles.

Irrotationality

An important point is that the velocity field is *irrotational*, *i.e.*, $\vec{\nabla} \times \vec{v} = 0$, because the velocity field is given by the gradient of the quantum phase. Hence velocity is a conservative field and the phase of the wavefunction acts as a potential. No friction occurs in an interacting BEC, the reasons for that are explained in the following section.

1.2 EXCITED STATES OF BEC

1.2.1 Linear Excitations, Dispersion Relation and Superfluidity

The hydrodynamic description permits to describe the elementary excitations of the condensate as normal modes of vibration of the wavefunction. A wave equation can be derived from equations (1.14),

after a linearization with respect to the variations δn and $\delta\vec{v}$ from the equilibrium solution $n_{\text{eq}}(\vec{r}) = [\mu - V_t(\vec{r})]/g$ and $\vec{v}_{\text{eq}}(\vec{r}) = \vec{0}$:

$$\frac{\partial^2 \delta n(\vec{r},t)}{\partial t^2} = \vec{\nabla}\cdot\left[c^2(\vec{r})\vec{\nabla}\delta n(\vec{r},t)\right], \tag{1.16}$$

where $c^2(\vec{r}) = \frac{g}{m}n_{\text{eq}}(\vec{r}) = \frac{\mu_{\text{loc}}(\vec{r})}{m}$. The quantity $c(\vec{r})$ is the local sound velocity. These modes must be seen in this framework as classical waves, without quantized structure.

Bogoliubov dispersion relation

A more refined description of a BEC, based on a second quantization approach, is known as the *Bogoliubov approach*, for which I refer to Dalfovo et al. 1999. Such a formalism permits to interprete BEC excitations as quasi-particles characterized by the Bogoliubov dispersion relation:

$$\hbar\omega_k^B = \sqrt{\frac{\hbar^2k^2}{2m}\left(\frac{\hbar^2k^2}{2m} + 2\mu\right)}. \tag{1.17}$$

In the dispersion relation (1.17) two regimes can be identified observing that $2\mu = 2gn = 8\pi\hbar^2 na/m = \hbar^2/(m\xi^2)$:

- $k \ll \frac{1}{\xi}$, *i.e.*, the long-wavelength limit: the kinetic term is negligible with respect to the chemical potential and the dispersion relation becomes linear with k:

$$\omega_k^B \simeq ck \quad \text{with} \quad c = \sqrt{\frac{\mu}{m}}; \tag{1.18}$$

  in this regime excitations are phonons propagating through the condensate at the sound velocity c, in analogy to what is obtained with the hydrodynamic approach;

- $k \gg \frac{1}{\xi}$: dispersion relation is approximated as:

$$\hbar\omega_k^B \simeq \frac{\hbar^2k^2}{2m} + \mu, \tag{1.19}$$

  recovering the free-particle dispersion law shifted by the chemical potential. In this regime an elementary excitation is close to an ordinary particle propagating in the condensate with an energy modified by the interaction with the condensed atoms (mean-field energy).

Superfluidity

The Bogoliubov dispersion relation plays a central role in the microscopic interpretation of *superfluidity*. A superfluid is characterized by a vanishing viscosity, thus it flows without dissipation. The first experimental evidence of such a phenomenon dates back to 1938 with the experimental observations by Allen et al. 1938; Kapitza 1938. The criterion for having superfluidity was proposed by Landau and it is based on the calculation of the energy exchange between a moving

microscopic probe (e.g. a point-like particle of mass M and velocity $\vec{v}$) and the surrounding fluid. The particle experiences friction forces if and only if it interacts with the fluid, creating an excitation $(\hbar\vec{k}, \hbar\omega_k^B)$ according to (1.17). Imposing energy and momentum conservation one obtains the following condition for transferring energy from the particle to the fluid:

$$\vec{v} \cdot \vec{k} = \omega_k^B + \frac{\hbar k^2}{2M} \geq \omega_k^B, \tag{1.20}$$

from which the Landau criterion can be derived:

$$v > v_c = \min_k \frac{\omega_k^B}{k}. \tag{1.21}$$

If the right-hand term of (1.21) is different from zero, for sufficiently small velocities the particle does not transfer energy to the fluid, flowing through it without drag. Thus if $v_c \neq 0$ the fluid is said to be a superfluid. In the case of the interacting BEC, from the Bogoliubov dispersion relation (1.17) one obtains that the critical velocity is the speed of sound: $v_c = c$; this behaviour comes from the linearity of the dispersion relation for long-wavelength excitations. A distinction between superfluidity and condensation has to be stressed. Indeed the two phenomena are independent and one can occur without the other: in the case of a non-interacting gas (experimentally achievable by tuning to zero the scattering length via the Fano-Feshbach mechanism) the dispersion relation shows a quadratic behaviour for $k \to 0$ and hence the critical velocity vanishes; in this case we have condensation without superfluidity. On the other hand a system with reduced dimensionality does not undergo the BEC continuous phase transition because of the lack of long-range order, nevertheless such systems can show superfluidity thanks to a non-vanishing critical velocity. For example in two-dimensional uniform systems there is no BEC transition but interactions introduce a different kind of phase transition, known as *Berezinskii-Kosterlitz-Thouless* (BKT) transition, which separates a superfluid phase ($T < T_{\text{BKT}}$) from a normal one ($T > T_{\text{BKT}}$).

1.2.2 Non-linear Topological Excitations

The interacting BEC is therefore a superfluid, the motion of which is governed by the relation linking velocity and gradient of the phase of the wavefunction (equation (1.13)). The velocity field of particles admits a potential, which is the phase of the wavefunction, and hence it is irrotational. Irrotationality introduces strong constraints on the superfluid motion when it is rotating around an axis or carrying angular momentum: the formation of *quantized vortices* is triggered. Quantized vortices are topological defects in the wavefunction, which is then singular in the vortex core. Such a behaviour is required in order to maintain a finite energy when the irrotational velocity field

diverges when approaching the vortex core. In the following section I will describe the structure of quantum vortices from a topological point of view, showing the necessity of the quantization of the velocity flux.

1.2.2.1 *Some Useful Concepts*

Before entering in the description of vortex states in a BEC, it is useful to introduce some ideas from classical hydrodynamics and mathematics. In the following paragraphs I will introduce the two main types of vortex in classical hydrodynamics: *rotational* and *irrotational* vortex. Such a distinction provides a usefool tool for discriminating classical from quantum vorticity. Then I will introduce some basic ideas of topology, a branch of mathematics which is central in the framework of quantum vorticity to justify the irrotationality of the superfluid.

VORTICITY A *vortex* is a region in a fluid in which the particles are rotating around a straight or curved line. A useful quantity for describing the behaviour of vortices is the *vorticity*, which is a vector coding the local rotary motion at a point in the fluid with respect to a reference system moving with the fluid. Mathematically, vorticity is defined as

$$\vec{\omega} = \vec{\nabla} \times \vec{v}, \tag{1.22}$$

not to be confused with the angular velocity $\vec{\Omega}$. Vorticity is twice the angular velocity of a local probe traveling along the fluid relative to its center of mass. Basing on the properties of vorticity one can distinguish two main kinds of vortex, see figure 1.2:

- *rigid-body* or *rotational vortex*: the fluid rotates like a rigid body, with uniform angular velocity. The velocity increases linearly with the distance from the vortex line and vorticity is finite:

  $$\vec{\omega} = \vec{\nabla} \times \vec{v} = \vec{\nabla} \times (\vec{\Omega} \times \vec{r}) = 2\vec{\Omega}. \tag{1.23}$$

  Hence the local probe revolves around its center while orbiting around the vortex core with an angular velocity which is the half of vorticity and directed in the same way as the vortex spin;

- *irrotational* or *free vortex*: the velocity field is inversely proportional to the distance from the core, leading to a null vorticity:

  $$\vec{v} = \left(-\frac{\alpha y}{r^2}, \frac{\alpha x}{r^2}, 0\right) \Rightarrow \vec{\Omega} = \left(0, 0, \frac{\alpha}{r^2}\right) \Rightarrow \vec{\omega} = 0. \tag{1.24}$$

  Thus the local probe keeps always its orientation while orbiting around the vortex core.

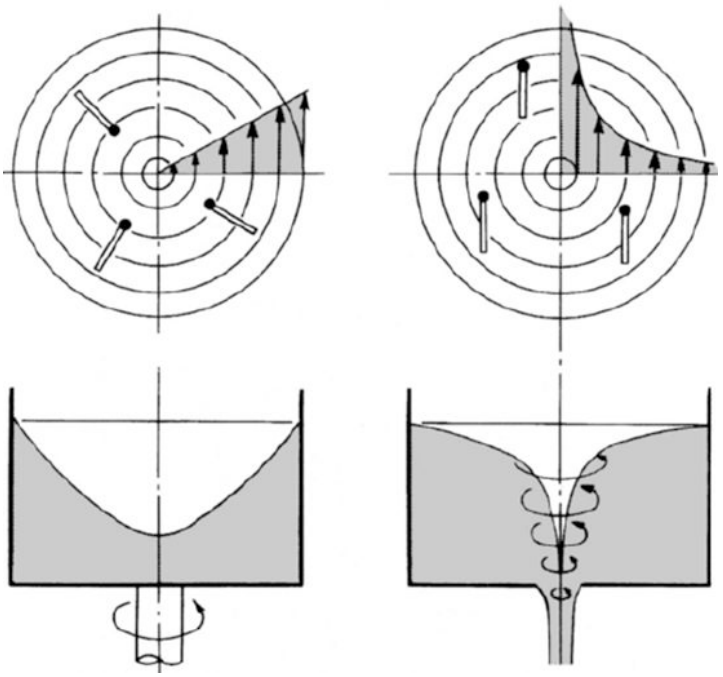

Figure 1.2: Velocity field in the case of a rotational (left) and an irrotational (right) vortex. A local probe is depicted by the stick.

In the case of an irrotational vortex the circulation of the velocity field $\Gamma = \oint d\vec{r} \cdot \vec{v}(\vec{r})$ is null when the integration contour does not enclose the vortex core because of the applicability of the Stokes' theorem, while it has a fixed value for any contour which encloses the vortex core. At the vortex core the singularity of the velocity field forbids the application of Stokes' theorem. In the classical framework a pure irrotational vortex does not exist because of the finite viscosity of a real ordinary fluid; a realistic model for a free vortex is the Rankine vortex, where an irrotational pattern occurs outside the core of the vortex while a rigid-body pattern describes the motion inside the core.

Toward quantum vorticity

What makes quantum vorticity different from classical vorticity is the intrinsic irrotational nature of the superfluid flow (given the relation (1.13)), which is given by the total absence of fricton in a superluid flow. Another difference is given by the quantization of the velocity field around the vortex core, required by the topological properties of the wavefunction of the system for describing vortices in the quantum picture. A word about topology to clarify its role is spent in the next paragraph.

TOPOLOGY Topology investigates properties of spaces, like *connection, compactness and continuity*, reducing them to fundamental groups independently of their particular shape. All geometrical objects in the plane or in the space are topological spaces, but also more abstract objects have topological properties, for example quantum-mechanical wavefunctions are topological spaces. Topological spaces are classi-

fied according to the relations between them: the key concept is the continuous mapping between two spaces. A continuous map is a transformation that transforms an object (topological space) into another "without cutting and pasting" it. In the case where such a transformation is possible between two objects, these are said to be *homomorphic*, and the transformation is called *homomorphism*. A weaker relation is the *homotopy*, which is a continuous transformation permitting some "stretching" of the object: for example the letters "O" and "Q", interpreted as topological objects for their shapes, are two not homomorphic topological spaces, but a homotopy between the two exists. Through homotopy topological spaces can be reduced to *fundamental groups of the topology*, which simply code the "number of holes" characterizing topological spaces belonging to a specific topology.

The concepts of topology find a large field of application in quantum mechanics: wavefunctions, being topological objects, can describe states differing in their topological charge (number of holes), giving access to exotic *topological states*. The role of topological phases of matter is now subject of numerous researches, culminating with the award of the 2016 Nobel prize for Physics to John Michael Kosterlitz, Duncan Haldane and David Thouless.

1.2.2.2 *Vortices in BEC*

A vortex in a Bose-Einstein Condensate is described by a solution of the Gross-Pitaevskii equation that carries angular momentum. To investigate the fundamental properties of a quantum vortex we consider for simplicity a homogeneous condensate and we treat the problem in cylindrical coordinates $(r_\perp, \varphi, z)$, where z is the axis along which the vortex core lie. A wavefunction carrying angular momentum along z has to be eigenfunction of the equaton:

$$\hat{L}_z \Psi = \hbar l \, \Psi, \tag{1.25}$$

where $\hat{L}_z = -i\hbar\partial/\partial\varphi$ is the z projection of the angular momentum operator. A function which is general solution of equation (1.25) can be written in the form

$$\Psi(r_\perp, \varphi, z) = \psi(r_\perp, z)\, e^{il\varphi}, \tag{1.26}$$

where we consider Ψ in the Madelung form, thus $\psi(r_\perp, z) = \sqrt{n}$. The GP equation (1.3) for the wavefunction $\psi(r_\perp, z)$ becomes:

$$-\frac{\hbar^2}{2m}\frac{1}{r_\perp}\frac{\partial}{\partial r_\perp} r \frac{\partial \psi}{\partial r_\perp} + \frac{\hbar^2 l^2}{2m r_\perp^2}\psi + g\psi^3 - \mu\psi = 0, \tag{1.27}$$

which can be rewritten in adimensional units introducing the normalized coordinate $\eta = r_\perp/\xi$, where ξ is the healing length, and the adimensional function $f(\eta)$ as $\psi = \sqrt{n} f(\eta)$:

$$\frac{1}{\eta}\frac{\partial}{\partial \eta}\eta\frac{\partial f}{\partial \eta} + \left(1 - \frac{l^2}{\eta^2}\right) f - f^3 = 0. \tag{1.28}$$

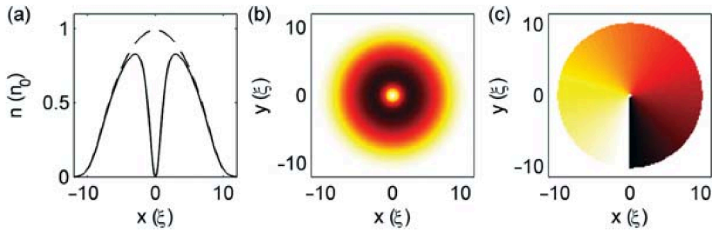

Figure 1.3: Density **(a-b)** and phase **(c)** profile of a vortex as calculated integrating the 2D Gross-Pitaevskii equation, from N. G. Parker et al. 2007.

The solutions of equation (1.28) are non-analytic, but from their asymptotic behaviour we reveal the importance of the quantum pressure term due to the density gradient:

$$f(\eta \to \infty) \to 1 \;\Rightarrow\; n = \psi^2 \to n_{bulk} \tag{1.29}$$

$$f(\eta \to 0) \sim \eta^{|l|} \;\Rightarrow\; n = \psi^2 \to 0, \tag{1.30}$$

i.e., the density of the superfluid tends to zero approaching the vortex core, while it assumes a constant bulk values n_{bulk} far away from the vortex. The length-scale that governs this behaviour is, as expected, the healing length. In figure 1.3 the density and phase profile of a condensate with a vortex are shown.

Vortex stability: topology, thermal instability, reconnection and Kelvin waves

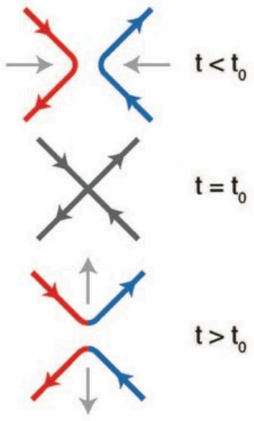

Figure 1.4: Sketch of the reconnection process, from Fonda et al. 2014.

The singularity of the wavefunction along the vortex core means that the vortex solution and the ground-state solution of the GPE are topologically distinct, being not connected by any homotopy. Such a property makes the vortex a stable structure because it is *topologically protected*: while a classical vortex can disappear everywhere in the fluid through thermal dissipation, a quantum vortex can be removed from a system only at its boundaries where density vanishes in confined systems. For example a vortex in a harmonically trapped system precesses around the center of the trap scattering with thermal excitations due to finite temperature. Such losses of energy make the vortex to drift radially toward the edges of the condensate.

Other important vortex dissipation mechanisms are *reconnections* and the excitation of *Kelvin waves*. A reconnection can occur when two vortices approach and cross: they can undergo an exchange of their tails, as depicted schematically in picture 1.4. Such processes will be more deeply addressed in the following chapters. Reconnections can introduce radial distortion of the vortex filament which can trigger the formation of Kelvin waves, *i.e.*, the transverse vibrating modes of a vortex line. Both Kelvin waves

Velocity field

and reconnections are responsible for the emission of sound waves in the condensate, dissipating in this way vortex energy.

The relation between the phase of the wavefunction and velocity (equation (1.13)), together to the wavefunction (1.26) gives the following components of the velocity field:

$$v_{r_\perp} = 0 \tag{1.31}$$

$$v_z = 0 \tag{1.32}$$

$$v_\varphi = \frac{\hbar l}{m r_\perp}, \tag{1.33}$$

which is the velocity pattern typical for irrotational vortices, singular at $r_\perp = 0$. The circulation Γ is therefore zero for paths not including the vortex line. Instead, if the circulating path includes a region which is not connected, the circulation takes a fixed value independently of the contour. Integrating along a circle of radius $r_\perp$:

$$\Gamma = \oint_{\mathcal{C}} \vec{v} \cdot d\vec{r} = \int_0^{2\pi} r_\perp v_\varphi d\varphi = l \frac{2\pi\hbar}{m}. \tag{1.34}$$

Such a relation can be seen also in a more general fashion as the requirements of the single valueness of the wavefunction around the vortex: the integral $\delta S = \oint_{\mathcal{C}} \vec{\nabla} S \cdot d\vec{r}$ is the phase increment in a loop around the vortex, hence $\delta S = 2\pi l$, where l is an integer, for having a uniquely defined wavefunction at a given point. Recapitulating, the velocity field around the vortex is quantized, taking discrete values given by the integer multiples of the quantum of circulation h/m.

Analogies with magnetostatics

In the case of the homogeneous and stationary system, the continuity equation (1.14a) becomes simply $\vec{\nabla} \cdot \vec{v} = 0$. Then the equations for the superfluid velocity show a strict analogy with equations of magnetostatics:

$$\vec{\nabla} \cdot \vec{B} = 0 \;\Leftrightarrow\; \vec{\nabla} \cdot \vec{v} = 0 \tag{1.35}$$

$$\vec{\nabla} \times \vec{B} = \frac{j}{\epsilon_0 c^2} \delta^{(2)}(\vec{r}_\perp)\hat{z} \;\Leftrightarrow\; \vec{\nabla} \times \vec{v} = l \frac{\hbar}{m} \delta^{(2)}(\vec{r}_\perp)\hat{z}, \tag{1.36}$$

where $\delta^{(2)}(\vec{r}_\perp)$ is the 2D delta function in the radial plane; thus the velocity field of a vortex has the same structure of the magnetic field produced by a current through a wire. This analogy is often used to simulate vortex dynamics in the mesoscopic scale.

Other descriptions of superfluidity

The description of superfluidity based on the Gross-Pitaevskii equation has a microscopic approach, which catches the mechanisms of vortex dynamics and vortex-vortex interaction (reconnection); its use is especially suited to atomic condensates because of their diluteness, while, in the case of strongly interacting systems like helium, its results have only a qualitative relevance. The mean-field approach described here is valid at $T = 0$, or, in good approximation, at very low temperatures, Dalfovo et al. 1999. Generalizations to finite temperature have been proposed, as the Hartree-Fock-Bogoliubov theory,

the Zaremba-Nikuni-Griffin theory or the stochastic Gross-Pitaevskii Equation. For details about these theories I refer to N. P. Proukakis 2007. Exploiting the analogy pointed out by (1.36), vortex dynamics can be treated through the Schwarz approach (Schwarz 1988): neglecting the effects at the scale of ξ the vortex is approximated as an infinitesimally thick line which moves according to the self-induced velocity field calculated via the Biot-Savart law. This approach does not directly include the possibility of reconnection.

VORTEX ENERGY AND ITS ORIENTATION The energy of a vortex is dominated by the kinetic energy due to the superfluid flow $\vec{v} = \frac{\hbar}{m}\vec{\nabla}S$ around its core (Cohen-Tannoudji et al. 2011). An estimation of this energy can be given considering the vortex core as a straight line parallel to $\hat{z}$ across the condensate. The vortex position is identified by the vector $\vec{r}_0 = (x_0, y_0)$ in the plane xy. The kinetic energy associated to a vortex of topological charge l is:

$$E_V(l) \approx \int d^3r \, \frac{1}{2} m \, n(\vec{r}, z) \, v^2(l). \tag{1.37}$$

The dependence in the plane xy of the density in equation (1.37) is neglected because the diverging contribution of the velocity field in $\vec{r}_0$ dominates the smooth variation of the density, which can be approximated with its value at the vortex position $n(\vec{r}_0, z)$. The problem has cylindrical symmetry along $\hat{z}$, hence $d^3r = dz\, dr\, r d\varphi$. Considering a uniform varying phase pattern around the core, $S = \arctan \frac{x-x_0}{y-y_0} = \varphi$, the velocity term becomes $v^2 = \frac{\hbar^2 l^2}{m^2 r^2}$. Thus the integration on $d\varphi$ gives simply a 2π, while on dz it gives the column density along $\hat{z}$ at the core position $n^z_{2D}(x_0, y_0)$. The integral in dr can be calculated between the core radius ξ and the extension of the sample $R_\perp$ along the axis perpendicular to the vortex, and it gives a logarithmic correction of the energy value. Hence

$$E_V(l) \approx \frac{\pi \hbar^2 l^2}{m} \, n^z_{2D}(x_0, y_0) \ln \frac{R_\perp}{\xi}. \tag{1.38}$$

Noticing that the column density is proportional to length of the vortex line L we get the important relation:

$$E_V \propto L. \tag{1.39}$$

Vortex orientation and System geometry

Given the behaviour (1.39), vortices tend to be the shortest as possible to minimize the energy. Two cases are then possible:

- *oblate* or *pancake systems*, where the shortest axis is parallel to the symmetry axis of the sample;
- *prolate* or *cigar-shaped systems*, where the shortest axis is perpendicular to the symmetry axis.

The case of rotating systems is different because the presence of rotation of the entire trap introduces a preferential alignment axis, which is the axis of rotation, independently from the shape of the sample; a detailed description of rotating systems, which are not treated in the present work, is given by A. Fetter 2009.

2 PRODUCTION AND DETECTION OF VORTICES IN A BEC

CONTENTS

In this chapter I will introduce the main techniques that may be used for generating and probing vortices in a Bose-Einstein condensate. The role of the geometry and dimensionality of the sample will be pointed out. Finally I will describe the main characteristics of the system considered in this thesis, highlighting its novel elements with respect to the more traditional approaches described during the chapter.

2.1 GEOMETRY AND DIMENSIONALITY

An important role in the studies of vorticity in BECs is played by the geometry and the dimensionality of the sample. A strictly 1D system cannot sustain vortex solutions: the only defect supported in this system is the *soliton*, which represents a phase disontinuity in the order parameter (*phase kink*)[1]. In 2D systems a vortex can appear as a point-like singularity characterized by a 2π phase winding around it. If the system is infinite the absence of a long-range order, because of the algebraic decay of the coherence length, prevents the system from condensation. Such systems undergo to a transition between a normal and a superfluid phase without the appearence of Bose-Einstein condensation. The different phase transition is called Berezinskii-Kosterlitz-Thouless transition. On the other hand, if the 2D system is finite, the setting of a condensed phase is permitted because of the non neglibility of the coherence length given by the algebraic behaviour. In a 3D system the vortex has a filamentary structure: the singularity of the wavefunction happens along a line of vanishing density, around wich the phase winds up.

1 A compete review on solitons, vortices and related phenomena can be found in the book by Kevrekidis et al. 2007.

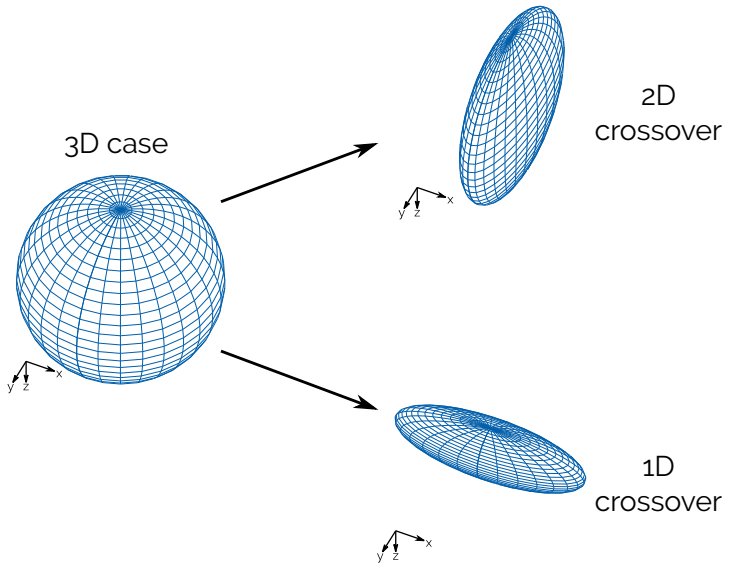

Figure 2.1: Sketch of the dimensional crossover from a spherical 3D system toward 2D and 1D geometries.

Dimensionality crossovers

Dealing with phase defects it is useful to define the dimensionality of a system through the relation between the sizes of the sample and the characteristic dimension of a defect in a BEC, *i.e.*, the healing length ξ. A dimension is actually frozen if the extension of the sample in that direction is less than the healing length. A system is fully 3D if all its sizes are much larger than the healing length. The intermediate cases, where the system is not too large with respect the defect size, can be considered as sorts of *dimensional crossovers*, which can show peculiar properties in the dynamical behaviour of the defects. Three main regimes can be recognized:

- *3D → 2D regime*: the trap frequencies have the hierarchy $\omega_x > \omega_y = \omega_z \equiv \omega_\perp$, and the sample has an *oblate* (*pancake*) shape;
- *3D → 1D regime*: the trap frequencies have the hierarchy $\omega_x < \omega_y = \omega_z \equiv \omega_\perp$, and the sample has a *prolate* (*cigar*) shape;
- *intermediate regime*: the frequencies are $\omega_x < \omega_y < \omega_z$.

A pictorial view of the first regimes is sketched in figure 2.1. As anticipated in the last section of the previous chapter, the shape of the sample has a strong influence on the orientation of the vortex lines: they are aligned along the axis of the system in the case of a pancake, while they are aligned radially in the cigar. The perfect cylindrical symmetry of a cigar-shaped system prevents vortices to have a preferred orientation. Hence a peculiarity of the cigar-shaped samples is to support the possibility of vortices crossing each other with arbitrary orientations, realizing a fully 3D vortex-vortex interaction. On the other hand in a pancake the vortex-vortex interaction manifests

as a 2D interaction between point-like particles, since all vortices are aligned. The intermediate case is characterized by an effective 2D vortex behaviour, because the alignement is favoured along the only direction of maximum confinement.

Effect of trap rotation

The case of a rotating system is also important, since many experiments deal with rotating traps to produce vortices. In the case of a trapping potential rotating with an angular velocity Ω around the x axis, the energy of the condensate in the rotating frame becomes:

$$E = E_0 - \Omega L_x, \tag{2.1}$$

where E_0 is the energy in the rest frame and L_x is the projection along x of the angular momentum carried by the condensate. If no vortices are present $L_x = 0$ and hence $E = E_0$. This happens when the rotation frequency of the trapping potential is below a critical value and hence the sample does not rotate, in accordance to the Landau criterion for the appearence of excitations in a superfluid. The presence of a vortex with topological charge l introduces an angular momentum $L_x = l\hbar$ and energy $E_V(l)$ in the system. The energy is therefore $E = E_0 + E_V(l) - \hbar l\Omega$. The creation of a vortex is favorable in the case of rotations with a frequency $\Omega > \Omega_C \approx \frac{E_V(l)}{l}$, in which condition the energy in the rotating frame is minimized. The minimization here occurs if vortices carry angular momentum along the rotation axis, hence a vortex state in a rotating system shows vorticity aligned along that axis, independently of the shape of the sample.

2.2 PRODUCTION OF VORTICES

Many techniques for the production of vortices have been developed since the first pioneering experiment by Matthews et al. 1999. We can characterize such techniques according to the number of vortices they are able to generate, and to the *deterministic* or *stochastic* nature of the method, *i.e.*, the possibility to generate in a reproducible manner a given vortex configuration.

Vortex number

Some techniques can be used to produce states with a single vortex, useful to probe the structure of a vortex and its dynamical behaviour from a "single-particle" point of view. Other techniques permit instead to probe the physics of few-vortex systems, hence studying the effects due to the simultaneous presence of two or three vortices, also with different signs. Finally systems with many vortices (up to hundreds) can be produced, where the mechanisms of the interactions can lead to the formation of an ordered phase, a *vortex lattice*, or of the chaotic phase called *turbulence*.

Deterministic and stochastic vortex production

The second main characteristic of a vortex-production method is its deterministic or stochastic nature. Such a characteristic strongly influences the way to probe the system. Indeed, if vorticity can be gener-

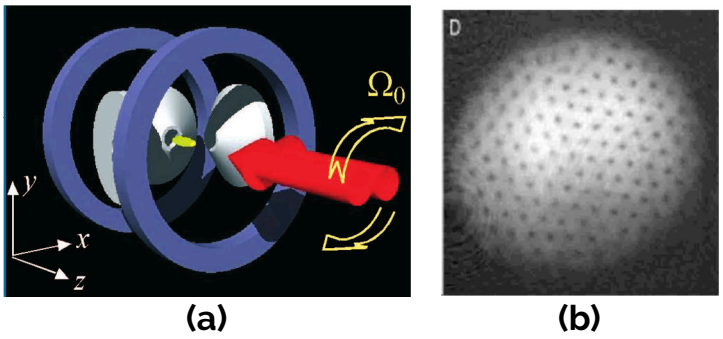

Figure 2.2: **(a)** Putting a condensate into rotation, from Chevy 2007. **(b)** Vortex lattice, from Abo-Shaeer et al. 2001.

ated obtaining always the same dynamical state within different experimental runs, its study can be carried on with a standard destructive imaging technique and repeating the experiment in the same conditions. For studying stochastically generated vortices, instead, real-time barely-destructive techniques have to be implemented, because each experimental run produces a different vortex state.

STIRRING AND ROTATION The most straightforward method for creating vortices in a BEC consists in putting the superfluid in rotation through mechanical stirring of the sample. This approach is implemented by introducing a transverse asymmetry in the confinement of an axisymmetric sample, and then varying in time such an anisotropy to set an effective rotation of the trapping potential. This method can be applied to oblate systems rotating around the tight-confinement axis or to prolate ones rotating around the axis of shallower confinement. The first realization of such a scheme was implemented by Madison et al. 2000, where a cigar-shaped condensate in a magnetic trap was perturbed by two far detuned optical beams copropagating along the axis of the sample and rotataing around it (see figure 2.2 **(a)**). The beams introduce a slight modification of the radial confinement in the plane defined by the beams. The rotational motion of such a distortion puts the superfluid in rotation during the evaporation. When a critical angular velocity is reached, the energy of the final superfluid can be minimized through the formation of vortices. Increasing the rotation frequency, more and more vortices are nucleated, permitting to create from one-vortex state, just above the critical rotation, to many-vortex states. Such a method is extensively used for generating vortex lattices (Abo-Shaeer et al. 2001; Haljan et al. 2001), represented in figure 2.2 **(b)**. In the experiment by Hodby, Hechenblaikner, et al. 2001, the rotating anisotropy was implemented modifying the bias field of an axially symmetric time-averaged optical potential trap. In this way the rotation is induced in a purely magnetic way without the need of optical beams.

A variation on the technique was implemented by Engels, Coddington, Haljan, Schweikhard, et al. 2003 for the observation of giant vortices. They impart angular momentum to a thermal sample via a sudden change of the ellipticity of a magnetic trap, remove then the radial anisotropy and evaporate the system to reach condensation. The final condensate keeps the rotation imparted to the thermal sample, thus vortices appear in it.

Another way to stir a condensate and favour the formation of vortices was implemented by Inouye et al. 2001, where vortices are generated by the passage of a tightly focused far-blue-detuned laser beam across the condensate. A refined implementation of such a stirring process was given by Neely et al. 2010, where they show the deterministic creation of a pair of vortex and antivortex. Such a technique was used to probe 2D turbulence in BECs by Kwon, Moon, et al. 2014, and to generate von Kármán vortex street in an oblate superfluid by Kwon, J. H. Kim, et al. 2016.

Vortices can be created also in annular condensates moving an optical barrier along the ring, as realized by Wright et al. 2013. The motion of the barrier along the ring can generate persistent quantized currents, depending on its angular frequency. When the angular frequency becomes large, the formation of vortices in the annulus is favoured, beside the setting of the persistent current.

PHASE IMPRINTING Another method for producing vortices in BECs consists in imprinting a phase pattern on the wavefunction. A phase can be imprinted on a sample in a magnetic trap varying slowly the bias magnetic field to rotate the local direction of the spins[2]. Atoms follow adiabatically the rotating magnetic field, acquiring a space-dependent quantum phase in the form of a Berry phase, due to the inhomogeneous trapping field experienced during the adiabatic rotation. The acquired phase leads to the formation of a single-vortex state, whose sign depends on the sign of the internal state m_F. This scheme was realized by Leanhardt et al. 2002. They also show the applicability of such a technique for producing vortices with multiple quanta of circulation.

Another scheme to imprint a wrapping phase in the BEC wavefunction was implemented by Andersen et al. 2006. This scheme uses a two-photon Raman process stimulated by two laser beams, where one of the two has a gaussian profile, while the other shows a Laguerre-Gauss profile. A Laguerre-Gauss beam carries angular momentum, which is transferred to the sample in the Raman process. With this technique single vortices with arbitrary winding number can be imprinted in a deterministic way.

2 A bias magnetic field is usually applied to suppress Majorana losses in the region of vanishing magnetic field (Ketterle, Durfee, et al. 1999).

Vortices can be created also through the decay of dark solitons. Dark solitons are unstable in systems with more than one dimension since they undergo snake instability and decay to vortex states. Vortices can then be created imprinting a dark soliton in a 3D system (Denschlag et al. 2000) and waiting for its decay (B. P. Anderson, Haljan, Regal, et al. 2001). A dark soliton can be imprinted by means of a sharp-edge far-detuned laser beam illuminating only a part of the condensate. The two parts acquire a differential phase, whose magnitude is related to the intensity and to the duration of the illumination of the condensate. If the imprinting is well controlled, the products of the decay show a reproducible dynamics, as shown in a fermionic superfluid by Ku, Ji, et al. 2014.

MERGING OF DIFFERENT CONDENSATES A phase defect can be created when merging different independent BECs, each with a well defined uniform phase. The condensation appears by means of a second order classical phase transition. The role of the order parameter is played by the BEC wavefunction, which is a complex scalar field. Thus, the crossing of the transition spontaneously break the $U(1)$ symmetry on the phase of the wavefunction. Independent samples pick up different random phases when they cross the BEC transition. By putting in contact such different systems, one creates a unique condensate with a patchworked phase. If two condensates are put together, a phase jump in the junction produces a dark soliton. When three or more condensates meet in a common point and their phases change with monotonic jumps from a condensate to the following when moving around that point, a vortex can appear. Such an approach was demonstrated by Scherer et al. 2007, producing three independent condensates in a triple-well trap and then removing the barriers between the samples.

A similar approach was also used by Schweikhard et al. 2007 to study the vortex proliferation in the Berezinskii-Kosterlitz-Thouless phase. In this case an initial condensate is loaded into a 2D optical lattice and tunneling between adjacent sites is then suppressed. In this way, thermally activated phase fluctuations between condensates in each well are enhanced. Switching off the optical lattice, all the condensates merge and the site-to-site phase fluctuations can lead to vortex production. Thermally activated vortices were studied also by Choi et al. 2013 in the crossover between the BKT phase and the BEC phase in a finite 2D system.

KIBBLE–ZUREK MECHANISM A mechanism similar to the merging of multiple BECs occurs in the Kibble-Zurek mechanism (Kibble 1976; Zurek 1985). It consists in the spontaneous formation of defects in the order parameter of a system when a classical or quantum phase transition is crossed in a finite quenching time τ_Q. The formation of

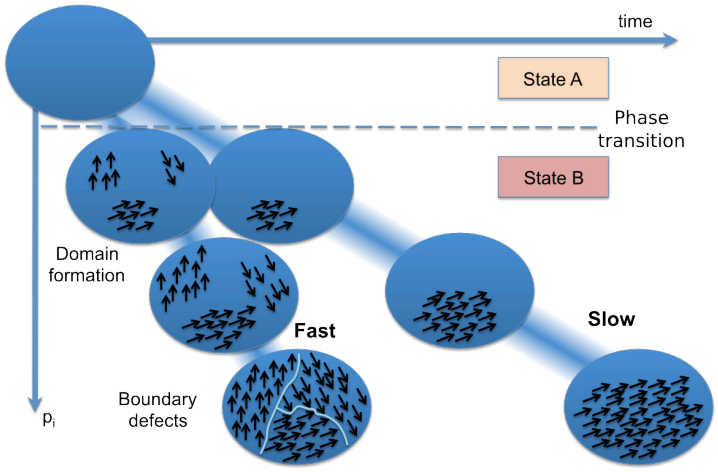

Figure 2.3: Schematic representation of the Kibble-Zurek effect.

defects is due to the independent nucleation of the ordered phase in regions that are causally disconnected, and hence each part of the system breaks the symmetry independently of the others. When the condensates grow, phase defects can appear between their boundaries and, for the same reason reported in the previous paragraph, vortices or solitons can be formed. The nature of the stable defects depends on the dimensionality of the system, and the number of defects created depends on the quench time across the transition through a power law:

$$N_{\text{def}} \propto \tau_Q^{-\alpha}, \tag{2.2}$$

where α depends on the system and defect dimensionality and on the critical exponents of the phase transition. A pictorial representation of the KZM is reported in figure 2.3. Such a mechanism was studied for the first time in BECs by Weiler et al. 2008. Then the KZ mechanism was used by Freilich et al. 2010 to study single vortex and vortex dipole precession through real-time imaging (more on this topic will be given in the following chapters). A refined characterization of the Kibble-Zurek mechanism in prolate BECs was given by our group (Lamporesi, Donadello, Serafini, Dalfovo, et al. 2013; Donadello, Serafini, Bienaimé, et al. 2016), while studies on homogeneous BECs were carried on by Navon et al. 2015 and in 2D systems by Corman et al. 2014; Chomaz et al. 2015.

2.3 VORTEX DETECTION

In this section I will briefly describe the techniques employed for probing vortices in a Bose-Einstein condensate. The special requirements needed to probe vortex states, both in the case of determinis-

tic and stochastic generation, will be considered. I will mention also other techniques beyond the direct imaging that can be used.

Imaging a BEC

A Bose-Einstein condensate is normally probed by shining some light on it and observing how the beam is transformed by the interaction with the sample (Ketterle, Durfee, et al. 1999). The most employed techniques for imaging Bose-Einstein condensates are:

- *absorption imaging*;
- *dispersive imaging*.

The index of refraction of a dilute gas of atoms is, for low light intensity[3]:

$$n_{\text{ref}}(x,y,z) = 1 + \frac{\sigma_0 n(x,y,z)\lambda}{4\pi}\left(\frac{i}{1+\frac{4\delta^2}{\Gamma^2}} - \frac{\frac{2\delta}{\Gamma}}{1+\frac{4\delta^2}{\Gamma^2}}\right), \tag{2.3}$$

where $n(x,y,z)$ is the density of the sample, λ is the probing light wavelength, δ is the detuning of the probe beam from the resonance, Γ is the atomic natural linewidth of the excited level and σ_0 is the on-resonance scattering cross section:

$$\sigma_0 = \frac{3\lambda^2}{2\pi}. \tag{2.4}$$

If the sample is illuminated with an optical field $\vec{E}_0$ propagating along y, the transmitted field is given by:

$$\vec{E}(x,z) = \vec{E}_0 \exp\left\{-\frac{2\pi i}{\lambda}\int dy(n_{\text{ref}}(x,y,z)-1)\right\} = t\vec{E}_0 e^{i\phi}. \tag{2.5}$$

Intensity and phase of the probe beam changes according to the following relations:

$$t = e^{-\mathscr{O}/2} \tag{2.6}$$

$$\phi = -\delta\frac{\mathscr{O}}{2}, \tag{2.7}$$

where the *optical density* $\mathscr{O}$ of the sample was introduced:

$$\mathscr{O}(y,z) = \frac{\sigma_0}{1+4\delta^2/\Gamma^2}\int n(x,y,z)dx. \tag{2.8}$$

Equation (2.6) defines the absorption properties of the sample, while equation (2.7) is related to the dispersive part of the interaction, giving the phase shift accumulated across the sample.

3 In particular $I \ll I_{\text{sat}}$, where I_{sat} is the saturation intesity, see appendix A.

ABSORPTION IMAGING Absorption imaging consists in observing the intensity transmitted through the sample in the focal plane of the imaging system with a square-law detector (for example a CCD or a CMOS). Such a detector is not sensitive to the phase of the field, but only to its intensity. The probe beam is set on resonance $\delta = 0$, thus the dispersive contribution is suppressed, while absorption is maximized. This technique consists in detecting the transmission coefficient t by measuring the intensity profile $I_0(y,z)$ of the unperturbed beam and the intensity profile $I(y,z)$ transmitted by the sample. The optical density is then calculated:

$$\mathcal{O}(y,z) = -\log t^2 = -\log \frac{I(y,z)}{I_0(y,z)}. \tag{2.9}$$

From the optical density profile (2.9), the extensions of the sample and the number of atoms in it can be inferred, depending on the fit model. The fit model is a gaussian profile for a thermal gas, a paraboloid for a condensate in a harmonic trap in the Thomas-Fermi regime (negligible thermal fraction) or a bimodal distribution for a BEC in the TF limit but with a non-negligible thermal fraction.

Absorption imaging is widely used for probing BECs because of its simplicity and richness of information. The main drawback of this technique is the necessity to probe samples with low optical density to be in the dilute regime. Absorption imaging cannot be used for probing in-situ samples, because of their very large optical densities and the sub-resolution size of defects. The absorption cross section, and hence the optical density, can be reduced by detuning the probe beam from resonance. However, such an approach introduces important non-linearities which make the imaging not reliable. Normally absorption imaging is performed on samples after a time of flight: the free expansion makes the density and hence the optical density, lower, permitting the implementation of on-resonance absorption imaging. Clearly such a technique is destructive because the absorption process exchanges a large amount of energy, heating the sample.

DISPERSIVE IMAGING This technique consists in enhancing the dispersive effect while making the detuning so large that the absorption process is suppressed. The information encoded in the phase shift of the probe beam can be converted in an intensity pattern, hence detectable by a CCD, introducing some spatial filters in the Fourier plane, in order to suppress the unscattered light (*Dark-ground imaging*) or to shift its phase with respect to the scattered light (*Phase-contrast imaging*).

Dispersive imaging is often used for imaging samples in-situ because optically thick samples are preferred with this technique. Furthermore, the strongly suppressed absorption gives the possibility to take multiple images of the same condensate.

2.3.1 Resolution and Destructivity

When a condensate is probed to investigate its defects, the resolution of the imaging system can be the main limiting factor. The typical in-situ dimension of a defect in a BEC is given by the healing length. Such a dimension can be sub-wavelength, making the implementation of an in-situ imaging impossible. In order to make the defects visible, a free expansion of the sample is needed, in order to lower its density, hence increasing the healing length (see equation (1.4)). The need of an expansion makes the dispersive imaging not ideal because of the reduction of the optical density, and hence of the signal-to-noise ratio. The absorption imaging is preferred for low-optical-density samples. In the case of deterministic creation of defects, the destructivity of absorption imaging does not represent the main limiting factor, because the dynamics of many defects with the same initial conditions can be studied in different experimental runs. In the case of stochastically-generated vortices a dynamical study requires more refined implementations.

Real-time minimally-destructive techniques

For observing the dynamical behaviour of non-deterministic defects, the imaging technique must permit the repetition of the measurement with the minimization of the effects of the probe beam on the sample. If the dimension of the vortex core is larger than the imaging resolution, a possible way to implement such an imaging is through in-situ dispersive imaging. However this condition is not fulfilled in all cases, especially when dealing with large samples with high densities, where generally the healing length is below the optical wavelength of the probe beam. To circumvent this issue a technique based on absorption imaging of only a part of the sample was suggested by Freilich et al. 2010. A fraction of atoms are transferred from the trapped BEC state to an auxiliary state, belonging to different hyperfine levels. The probe beam is resonant only with the atoms in the auxiliary state (*bright state*), while the trapped BEC is in a *dark state*. Atoms in the bright state can expand and, when the defects become large enough to be resolvable, a standard absorption imaging is performed only on this state. The effects on the trapped BEC are limited because the detuning of the probe beam reduces the absorption of photons, and is mainly due to the decrease of the atom number due to the partial transfer to the auxiliary state. An extensive treatement of partial-transfer absorption imaging is given by Ramanathan et al. 2012.

2.3.2 Probing Matter Waves

Beside the direct imaging of vortices that can be obtained through the aforementioned methods, other kinds of measurements can be implemented to study vorticity in a Bose-Einstein condensate. Since

Bose-Einstein condensation is a macroscopic quantum effect, samples can be probed by exploiting their wave properties.

Matter-wave interferometer

Exploiting the analogy of matter waves with optics, atomic interferometer can be implemented. Such interferometers give access to the phase of a BEC wavefunction, making it to interfere with another coherent matter-wave, which can be a different condensate or a part of the same condensate. Interference of macroscopically occupied matter waves was demonstrated by Andrews et al. 1997. The possibility to use interference for probing vortex states, which are characterized by a well defined phase pattern in the wavefunction, was suggested by Bolda et al. 1998 and realized by Chevy, Madison, Bretin, et al. 2001 and Inouye et al. 2001 with slightly different approaches. The presence of a vortex, with its non-uniform phase pattern in the wavefunction, leads to the observation of dislocations in the interference fringes, as shown in the top panel of figure 2.4. More details on the application of interferometry to characterize single vortices will be given in section 4.2.1, where I will describe also its implementation in our experiments.

The effect of interference between matter waves can be exploited to measure quench-induced supercurrents in annular condensates, as realized by Corman et al. 2014. The system consists of an annular condensate with another independent concentric disk-shaped condensate. The two condensates are released from the trap and the interference pattern can show concentric fringes or spiral patterns depending on the absence or presence of supercurrents in the annular BEC. The orientation of the spiral represents the direction of the superflow (see bottom panel of figure 2.4).

Matter-wave interferometry was used also by Hadzibabic et al. 2006 to study the BKT transition in a 2D bi-layer system, as reported in the left panel of figure 2.5. The interference fringes appearing from the superposition of the expanding atoms released from the two-layer trap are imaged through absorption imaging. From the contrast of the fringes the first-order correlation function can be measured. In the presence of vortices the phase pattern shows a sharp dislocation (see the right panel of figure 2.5).

Bragg spectroscopy

The presence of vortices can be inferred also through Bragg spectroscopy, as demonstrated by Muniz et al. 2006. The diffraction of the matter wave by an optical lattice occurs as a two-photon Raman process which is sensitive to the atomic velocity field because of the Doppler effect. The process involves atoms with the same projection of the velocity along the exchanged momentum. The diffraction pattern contains the information regarding the orientation of the coarse-grained velocity field, coded as a deformation in the shape of the diffraction peaks, as reported in the top panel of figure 2.6. Bragg spectroscopy can be used also for studying 2D quantum turbulence in BECs, as demonstrated by Seo et al. 2016. In this work Bragg spec-

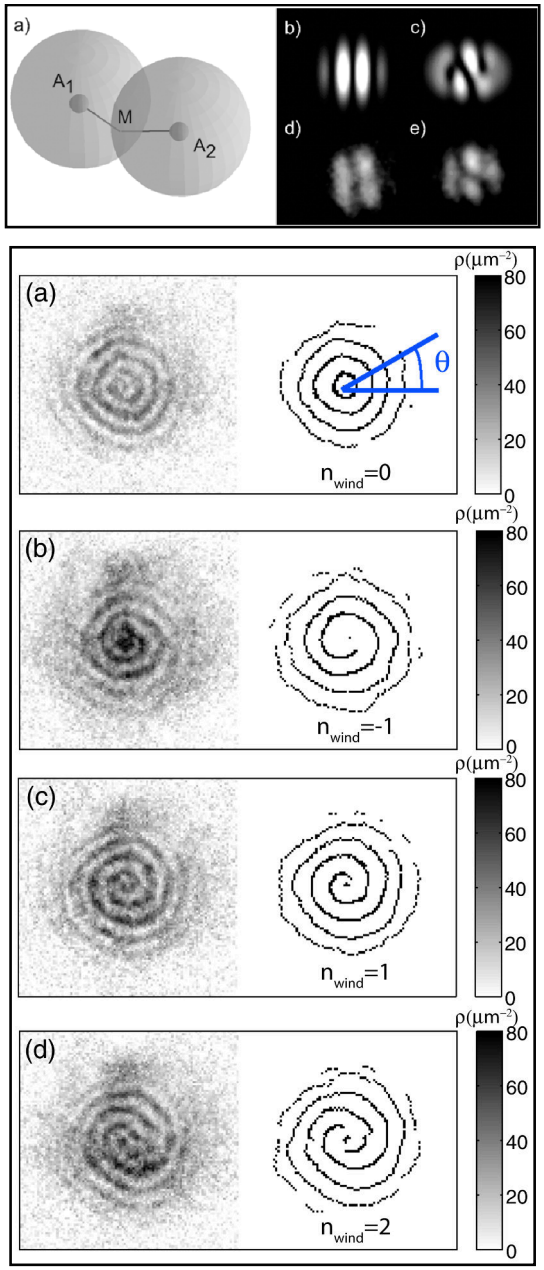

Figure 2.4: In the top panel the fringe patterns obtained through a matter-wave interferometer of a splitted condensate are shown in the absence **(b,d)** and presence **(c,e)** of a vortex, from Chevy 2007. In the bottom panel the supercurrent in an annular BEC is measured from the spiral interference pattern, from Corman et al. 2014.

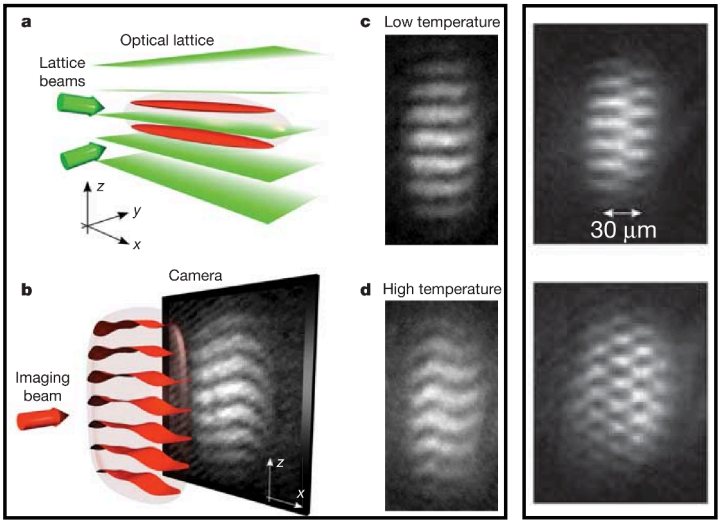

Figure 2.5: Left panel: sketch of the experiment by Hadzibabic et al. 2006. Right panel: signal of a single vortex (upper picture) and of multiple vortices (lower picture). Taken from Hadzibabic et al. 2006.

troscopy can spatially resolve the vortex structure, giving access to the local velocity field instead to a coarse-grained average of it, as reported in the bottom panel of figure 2.6.

The angular momentum carried by a condensate can be measured observing its collective oscillation modes. The presence of vortices modifies the frequencies of scissor and quadrupole modes of a Bose-Einstein condensate (Stringari 2001; Zambelli et al. 1998). The experimental verifications were given by Chevy, Madison, and Dalibard 2000; Hodby, Hopkins, et al. 2003.

2.4 OUR SYSTEM

The experiments and the numerical simulations presented in this thesis consider a non-rotating axially symmetric cigar-shaped condensate with vortex states created through the Kibble-Zurek mechanism. We therefore explore the vorticity in the 3D $\rightarrow$ 1D crossover, which is characterized by transverse vortices, also defined *solitonic vortices*. The first part of chapter 5 is devoted to the presentation and characterization of such defects, in terms of density and phase profiles, both in situ (section 5.1.1) and after expansion (section 5.1.2). The Kibble-Zurek mechanism is used to generate condensates with one or few vortices, to study the intrinsic dynamical behaviour of the vortex (section 5.2) and the effects of vortex-vortex interaction (chapter 6). The stochastic nature of the method imposes the necessity to implement a real-time minimally-destructive imaging. Our experimental samples are composed by a large number of atoms ($\sim 1 \times 10^7$ atoms), tightly confined in a magnetic trap. The healing length is $\sim 200\,\mathrm{nm}$,

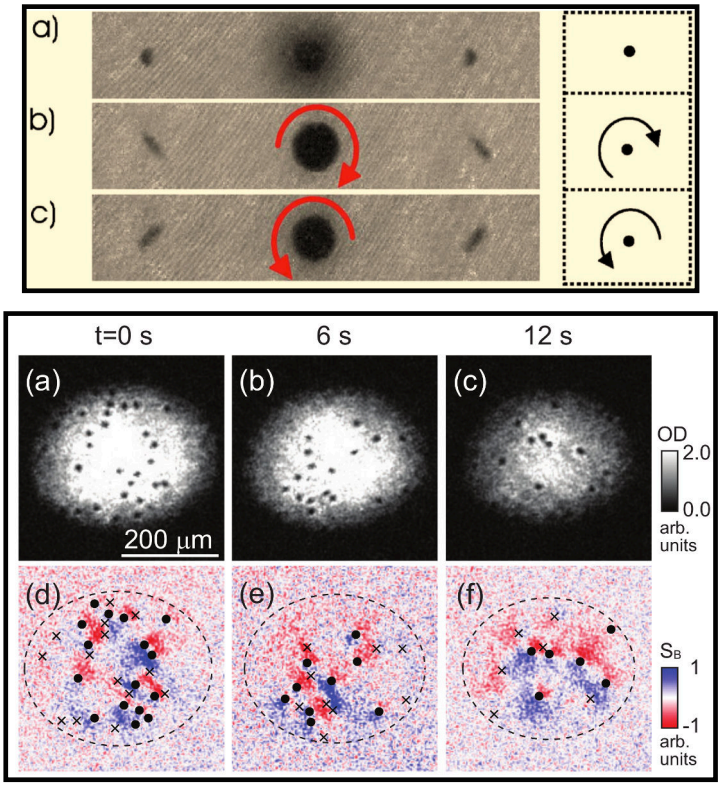

Figure 2.6: Top panel: Bragg diffraction of **(a)** a pure condensate, and of condensates with a vortex lattice with **(b)** a clockwise and **(c)** counter-clockwise vorticity, from Muniz et al. 2006. Bottom panel: **(a-c)** images of turbulent 2D BECs at different hold times with the corresponding Bragg signal **(d-f)**, the sign of the vortices is coded in the asymmetry of the Bragg signal around the vortex depletion, from Seo et al. 2016.

making the implementation of in-situ imaging impossible. In chapter 4 two implementations of partial-transfer absorption imaging techniques are described: a first one was used for the investigations on the single-vortex dynamics, the second one was developed for a better characterization of vortex-vortex interactions, and it presents an innovative way to perform the atom transfer to the auxiliary state. Such a novelty permits to characterize the radial orientation of a vortex line without imaging along the axial direction. The Kibble-Zurek mechanism permits to generate different initial conditions for each experimental run. This is very useful for exploring the mechanisms behind vortex-vortex interaction from a dynamical point of view, *i.e.*, exploring the role of the relative velocity and the relative orientation of the colliding vortices in the vortex-vortex interaction. No adjustements of the experimental setup are needed to explore different sets of initial conditions.

The dynamical approach to study vortex collisions is still an unexplored field, both from the experimental and numerical point of view. The richness of our system lies in the cigar-shaped geometry which permits collisions between vortices with arbitrary orientations. The stochastic generation of vortices can be exploited to explore easily a large range of initial conditions without any adjustement. Finally, the implementation of a novel innovative imaging technique gives a complete information on the vortex dynamics.

Part II

EXPERIMENTAL SETUP AND TECHNIQUES

The second part of this thesis is devoted to the description of the experimental apparatus of the Ultracold Gases Laboratory of the University of Trento and INO-CNR BEC Center. I will describe also the procedure and the techniques implemented for the experiments on the study of vorticity in elongated Bose-Einstein condensates, paying particular attention on the novel real-time minimally-destructive imaging technique we developed.

3 EXPERIMENTAL SETUP

CONTENTS

The present chapter is devoted to the description of the experimental apparatus of the Ultracold Gases Laboratory of University of Trento and INO-CNR BEC Center. I will not enter in details about the laser cooling techniques, for which I refer to Cohen-Tannoudji et al. 2011 and bibliography therein.

SODIUM The atomic species used in our experiment is sodium (Na). The use of sodium in the field of Bose-Einstein condensation dates back to its first realizations in 1995 (K. B. Davis et al. 1995). Useful data concerning sodium properties are reported in the appendix A, to which I will refer for all the specific quantities and for the energy level diagrams. Sodium is characterized by an favorable combination of elastic scattering cross-section and three-body reconnection rate, making the evaporation process toward quantum degeneracy very effective. For this reason sodium is particularly suitable for producing very large BEC (Stam et al. 2007). Large condensates are a fundamental ingredient for exploring the real-time dynamics of stochastically generated vortices.

An experimental setup for studies on Bose-Einstein Condensates and, more generally, on ultracold gases is composed of these main parts:

- a *laser system*, necessary for laser cooling, imaging and internal state manipulation;
- a *vacuum system*, composed of the atomic source and the science chamber;
- an *atom trapping system* for keeping the sample confined during the experiment. It can be optical, magnetic or hybrid;
- an *electronic control system*, which controls in real-time all the actions occurring during an experimental run.

In the present section these blocks are described in details. The trapping system used for the investigations reported in this thesis is a purely magnetic one.

3.1 LASERS SYSTEM

The laser source is placed on a dedicated table separated from the main table hosting the vacuum apparatus. Laser light is distributed to the experiment on the main table through single-mode polarization maintaining optical fibers (SCHÄFTER & KIRCHHOFF PMC-630-4.5-NA011-3-APC-900-P). The separation of the laser source and the vacuum system permits the complete suppression of the resonant light near the science chamber, interrupting the fibers injection with mechanical shutters. All tables are delivered by TMC and are equipped with air-compressed suspended benches in order to decouple them from the floor.

Cooling and imaging light

Laser cooling of alkali atoms is achieved using an optical radiation tuned near a closed transition. In the case of sodium, given its nuclear spin $I = \frac{3}{2}$, the fine-structure ground state splits in two levels with total angular momenta $F = 1$ and $F = 2$. The most convenient closed transition is $3^2S_{1/2} : F = 2 \leftrightarrow 3^2P_{3/2} : F' = 3$, this is our *cooling transition*. There is a non negligible probability that atoms end up in the hyperfine state $F = 1$. This occurs because off-resonant excitation of $F' = 2$. Another beam tuned on the transition $F = 1 \leftrightarrow F' = 2$, that will be called *repumping transition*, is also needed to avoid accumulation of atoms in the dark ground state during the cooling stage. The sketch of the optical system is reported in figure 3.1.

Optical potentials

Far-detuned laser beams are useful to implement *optical potentials*, which can be used to trap atoms or to modify their dynamics. Such capabilities are due to the conservative dipole force exerted by non-resonant light on atoms; in particular the force can be attractive, if red-detuned, or repulsive, if blue-detuned with respect to an internal transition. Conservativity of the force is due to the very low scattering cross-section, which hence reduces heating mechanisms in the sample. Optical potentials depend on the geometry of the light beams and on their intensities.

LASER SOURCES The wavelength that we are interested in is not directly accessible with laser diode technology, but its use is strongly recommended compared to the use of dye lasers. In order to obtain the 589 nm radiation with solid-state technology we start from a master laser emitting at the double wavelength 1178 nm, made recently accessible with the quantum dots technology (Nevsky et al. 2008), and we double it using a non-linear crystal placed in a resonant optical cavity.

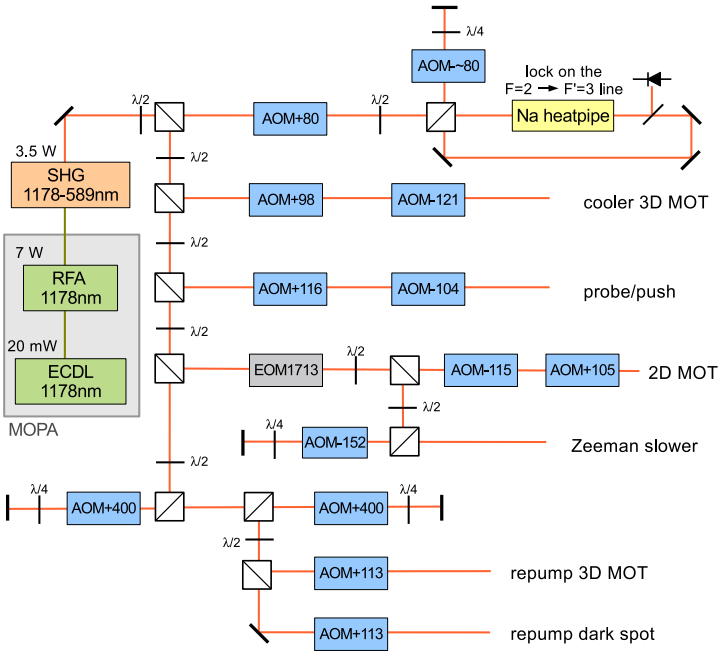

Figure 3.1: Simplified schematic of the optical system: the focusing and collimating lenses are not reported.

Doubling cavity

Before entering in the frequency-doubling cavity (by LEOS-SHG) the infrared beam coming from the master laser is amplified through a Raman fiber amplifier (MPB-RFA-YFL-P-8000-1178-SF); details on the Raman amplification can be found in Agrawal 2002. The input power of the amplifier is about 10 mW while its output power can be set up to 8 W.

After the frequency doubling we have available up to 4.5 W at 589 nm with a spectral width about 20 times smaller than the natural linewidth of the cooling transition ($\Gamma = 2\pi \cdot 9.79\,\mathrm{MHz}$).

The laser frequency is stabilized via a FM saturated absorption spectroscopy on the transition $3^2S_{1/2} : F = 2 \leftrightarrow 3^2P_{3/2} : F' = 3$ performed on a sodium vapour cell.

Optical potential source

The laser source for the generation of light to be used for optical potentials is a commercial INNOLIGHT/COHERENT MEPHISTO MOPA operating at 1064 nm, with a continuous power up to 42 W. A free-space doubling crystal (PPSLT) is also present on the main optical path to obtain, in addition to IR light, visible light at 532 nm. In this way both attractive and repulsive potentials can be generated. The beams are injected into polarization-maintaining fibers suitable for high-power operation; the fibers are NKT PHOTONICS LMA-PM-10.

3.2 VACUUM SYSTEM

The vacuum system is divided into two parts:

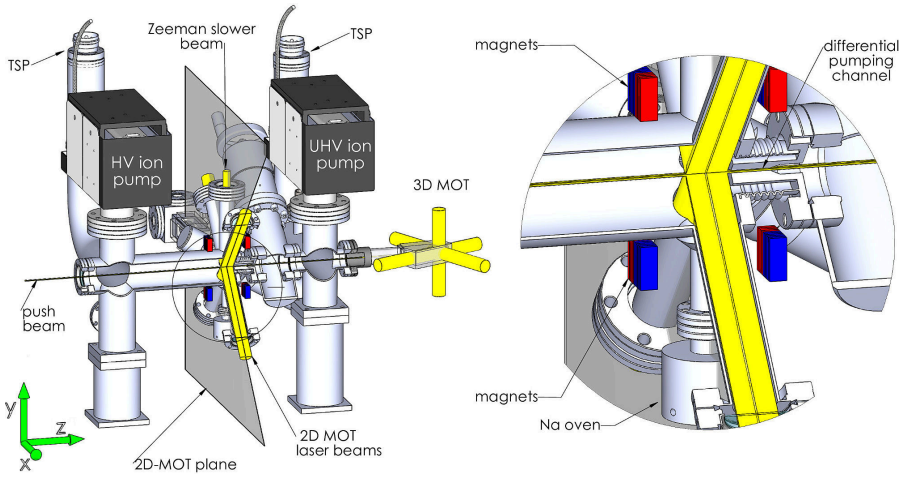

Figure 3.2: View of the whole vacuum system. The yellow thick beams represent the MOTs beams while the thin one is the pushing beam; they indicate the main optical accesses of the system. A particular of the 2D-MOT region and the differential pumping channel is zoomed at the right.

- an Ultra High Vacuum (UHV) region, hosting the science chamber, where the pressure is below 1×10^{-10} mbar;
- a High Vacuum (HV) region, where the pressure is of the order of 10^{-10}-10^{-9} mbar during the operation of the Na atomic source.

The vacuum system is depicted in figure 3.2 (rendering). The pumping system is composed of an ion pump in the Sodium MOT region and one in the UHV region, both pumps are Varian Starcell 55 l s^{-1}. There are also two Varian Titanium Sublimation Pumps (TSP), one in the HV region, the other in UHV region. The HV and UHV regions are separated from a Differential Pumping stage (DP) permitting a maximum pressure ratio between the two regions of two orders of magnitude. There is the possibility to isolate the UHV from the HV region via an all metal valve. In order to allow baking and to insure low outgassing properties, low magnetic permeability and minimization of eddy currents during the transients of magnetic manipulation, the metallic parts of the system are built with AISI 316 stainless steel. The science chamber has to fulfil more stringent requirements: in the science chamber atoms are magnetically trapped and manipulated with high precision thus, throughout the experimental sequence, the magnetic fields need to be controlled with high accuracy in the center of the science cell. For this reason the material for the science chamber has to be non magnetic and highly resistive in order to suppress eddy currents. In addition to these, good optical access has to be ensured. The science chamber is the part in which the quality of vacuum is most important: material constituting it should have little hydrogen outgassing. Quartz cells annealed with molecular bonding fulfil all these requirements and for this reason our science chamber is made employing this technology (figure 3.3).

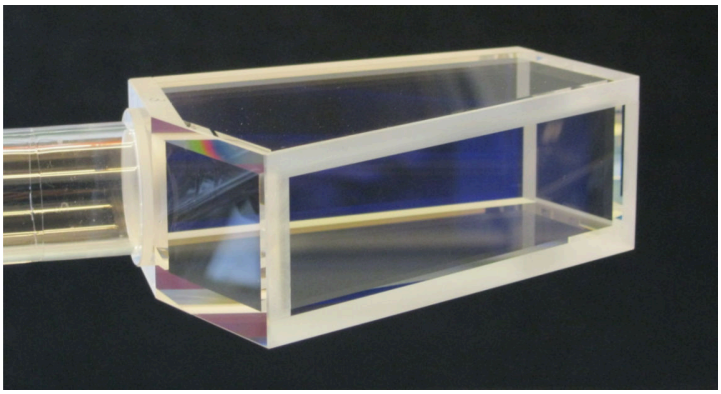

Figure 3.3: Photograph of the quartz cell constituting the science chamber.

HV REGION The HV region is the one at the left part of the differential pumping channel in figure 3.2.

Na 2D-MOT

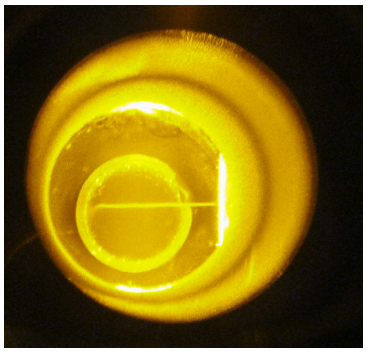

Figure 3.4: Fluorescence of atoms captured in the 2D-MOT.

On the main tube the 2D-MOT for sodium is hosted. The sodium atomic source is described in details in Lamporesi, Donadello, Serafini, and Ferrari 2013. Atoms coming from an effusive oven are first collected into a 2D-MOT (figure 3.4) and then sent to the science chamber through the DP channel by a push beam alligned along the axis of the MOT. In this manner the science chamber is not exposed to the direct flux of hot atoms coming from the oven, giving a better immunity against hot collisions in the cell. The loading of the final 3D-MOT in the UHV region can be modulated switching the 2D-MOT and the push beams. The principal characteristics of this source are:

- its compactness;
- high atom flux: higher than 1×10^9 atoms s^{-1} trapped in the final 3D-MOT hosted in the science chamber.

UHV REGION The UHV region is made of a stainless steel chamber that hosts the pumps and is connected with the differential pumping stage, and in the glass cell in which atoms are trapped. The glass cell, depicted in figure 3.3, is connected to the pumping stage with a CF40 flange through a glass to metal seal. The cell is designed to ensure a good optical access for imaging beams and for atomic manipulating beams. Its shape is a polyhedron with mostly 5 mm thick flat surfaces (except one 4 mm thick) and outer dimensions of about 35 mm $\times$ 80 mm $\times$ 60 mm. The four largest surfaces are exter-

nally coated with a broadband anti-reflecting film, giving a reflectivity $R \sim 0.5\,\%$ over the spectral range $530 \div 1100$nm. The particular design of the cell is necessary in order to avoid the overlap between the 3D-MOT laser beams and the axis of the flange connecting to the pumping unit and the atomic source (see figure 3.2). The cell was delivered by *Hellma Analytics* certified for vacuum leakage $< 3.2 \times 10^{-10}\,\mathrm{mbar\,l\,s^{-1}}$.

3.3 MAGNETIC TRAP

The principle of operation of a magnetic trap exploits the Zeeman structure of the atomic levels to modulate their energy through magnetic fields. In this way, depending on their internal state, the behaviour of atoms is controlled, permitting to trap, to eject or not to perturb them. This kind of modulation is done through an inhomogeneous magnetic field $\vec{B}(\vec{r})$, that interacts with an atom through the following potential:

$$U_{|F,m_F\rangle}(\vec{r}) = -\vec{\mu}_{\mathrm{at}} \cdot \vec{B}(\vec{r}) = \mu_B g_F m_F \left|\vec{B}(\vec{r})\right|, \tag{3.1}$$

where the vector of modulus $|\vec{\mu}_{\mathrm{at}}| = \mu_B |g_F m_F|$ is the magnetic moment of the atom expressed in units of the Bohr magneton μ_B and dependentent on the internal state $|F, m_F\rangle$ through the gyromagnetic factor g_F and the magnetic quantum number m_F. The potential (3.1) depends on the sign of the product $m_F g_F$, in particular:

- if $m_F g_F < 0$ atoms are attracted by the potential toward the regions where the modulus of the magnetic field is higher (*high field seeking* states);
- if $m_F g_F > 0$ atoms are attracted by the potential toward the regions where the modulus of the magnetic field is lower (*low field seeking* states).

Because of the Wing's theorem (see Meystre 2001 for a complete demonstration), which states that in a region without any charge and current a quasi-static solution of Maxwell equations can have only local minima but not local maxima, only low field seeking states can be magnetically trapped. In the case of sodium, see the tables of characteristic numbers in appendix A, the magnetically trappable states are $|1,-1\rangle$, $|2,1\rangle$ and $|2,2\rangle$, while $|1,1\rangle$, $|2,-1\rangle$ and $|2,-2\rangle$ are anti-trapped.

Ioffe-Pritchard trap

The Ioffe-Pritchard trap (Gott et al. 1962; Pritchard 1983) is based on a static magnetic field with cylindrical symmetry with a non-zero field minimum to prevent Majorana losses (see Majorana 1932; Ketterle, Durfee, et al. 1999). Along one axis the field is quadratic with a

bias term: $B_x = B_0 + B''x^2/2$. In order to satisfy the Maxwell's equations for a static field ($\vec{\nabla}\cdot\vec{B} = 0$ and $\vec{\nabla}\times\vec{B} = 0$) the magnetic field in the harmonic approximation has to be:

$$\vec{B}(\rho,\phi,x) = B_0\begin{bmatrix}0\\0\\1\end{bmatrix} + B'\rho\begin{bmatrix}\cos 2\phi\\-\sin 2\phi\\0\end{bmatrix} + \frac{B''}{2}\begin{bmatrix}-x\rho\\0\\x^2-\frac{\rho^2}{2}\end{bmatrix}. \tag{3.2}$$

The confining potential

The confining potential depends only on the modulus of the magnetic field:

$$|\vec{B}| = \Bigg[B_0^2 + B_0B''x^2 + \rho^2\left(B'^2 - \frac{B_0B''}{2} - B'B''x\cos 2\phi\right) + \frac{B''^2}{16}\rho^4 + \frac{B''^2}{4}x^4\Bigg]^{1/2}. \tag{3.3}$$

Substituting equation (3.3) into (3.1), the potential energy can be derived. This potential energy defines a trapping potential for low-field-seeking states, which in the low temperature regime, *i.e.*, $\mu_{at}B_0 > k_BT$, can be approximated by

$$U_{|F,m_F\rangle}(\vec{r}) \approx \mu_{at}B_0 + \frac{1}{2}\mu_{at}B''x^2 + \frac{1}{2}\left(\frac{B'^2}{B_0} - \frac{B''}{2}\right)\rho^2 = \tag{3.4}$$

$$\mu_{at}B_0 + \frac{1}{2}m\omega_\perp^2\left(y^2+z^2\right) + \frac{1}{2}m\omega_x^2x^2, \tag{3.5}$$

where the axial and radial trap frequencies $\omega_x = \sqrt{(\mu_{at}/m)B''}$ and $\omega_\perp = \sqrt{(\mu_{at}/m)(\frac{B'^2}{B_0} - \frac{B''}{2})}$ are introduced. Such frequencies characterize the strength of the confinement due to the magnetic potential in the radial direction ($\omega_\perp$) and in the axial direction (ω_x).

In the case of a high temperature regime, the sample experiences a linear confinement along the radial direction. This fact will be useful for the forced evaporation, as will be explained later in section 4.1.1.

The value set by $\mu_{at}B_0$ is the minimum Zeeman splitting, occurring at the bottom of the trapping potential. Its value is called *trap bottom*, often expressed in frequency units ($\nu_0 = \mu_{at}B_0/h$). The value of the trap bottom can be tuned to modify the radial confinement and hence the aspect ratio $\omega_\perp/\omega_x$.

Geometry

In our setup the trapping field is generated by the combination of several coils, as represented in figure 3.5. A pair of large coils in anti-Helmholtz configuration (cyan coils in figure 3.5) are used to generate a 3D spherical quadrupole field. This field is used also for the magneto-optical trapping stage. For producing the Ioffe-Pritchard field (equation (3.2)) a *pinch coil* (green in figure 3.5) is used. This coil cancels out the component of the gradient of the quadrupole field

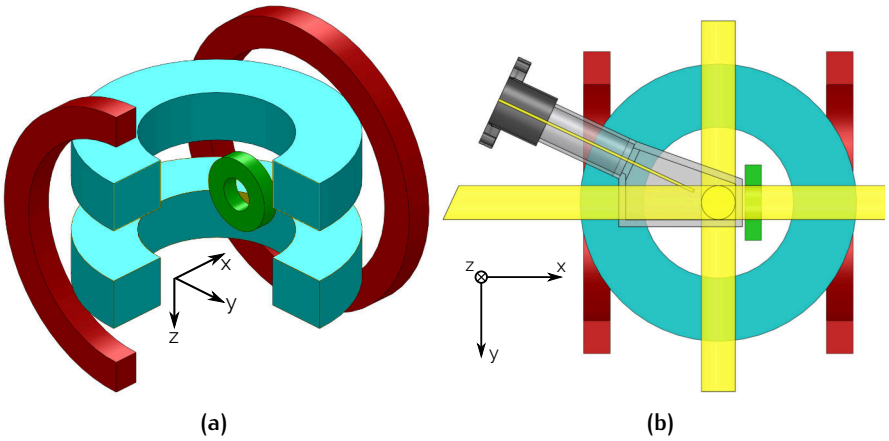

Figure 3.5: **(a)** Axonometry of the coil system for the generation of magnetic fields. **(b)** top view of the coil system with the glass chamber and optical beams.

along its axis x, introducing a shallow quadratic confinement. The axis of the pinch coil is the symmetry axis of our cigar-shaped BEC: I will refer to $\hat{x}$ as the *axial horizontal direction*, to $\hat{y}$ as the *radial horizontal direction* and to $\hat{z}$ as the *radial vertical direction*, hence gravity acts along $\hat{z}$. The pair of red coils in figure 3.5, called compensation coils, are needed to tune the bias field B_0 along the pinch axis, permitting to reduce it and hence to tighten the radial confinement. The coils are driven by a pair of high power supplies (Delta Elektronica SM30-200), which can be remotely controlled. Coils are water cooled through high pressure water flowing in the hollow core of the copper wire. The current is the same for all the coils, while the configuration of the active coils can be programmed acting on IGBT switches (Semikron SKM400GAL12E4) and relays (Kilovac EV200). IGBTs are used for fast switching operations and can be used with care for linear operation applying an analog voltage to their bases. The setting time for maximum magnetic field is $\sim$ 10 ms, while the switch-off time for the magnetic field normally used for BEC trapping is $\sim$ 150 µs. Relays can be used anytime the switching time is not critical, because of the long response time ($\sim$ 10 ms switching time versus a $\sim$ 1 µs for an IGBT). Configuring the coil system to allow current circulation through only one of the quadrupole coils permits to generate a levitating field, which is a crucial requirement to implement imaging after a long time of flight (section 4.2).

Shim and fine-tuning coils

Some additional smaller coils are added to cancel out the environmental magnetic field at the center of the trap. These are three independent pairs of coils in Helmholtz configuration, called *shim coils*. These coils have their axis oriented along the three orthogonal directions. The values of the currents circulating through shim coils are tuned to have an isotropic expansion phase during the optical mo-

Table 3.1: Design trap parameter.

	B_0 [G]	B' [G cm^{-1}]	B'' [G cm^{-2}]
I_{ht}	4	200	120
I_t	2	100	60
I_s	1	50	30

Table 3.2: Measured trap frequencies for the two BEC regimes and relative gravitational sags.

	$\frac{\omega_x}{2\pi}$ [Hz]	$\frac{\omega_\perp}{2\pi}$ [Hz]	$\frac{g}{\omega_\perp^2}$ [µm]
I_t	13(1)	131(1)	15
I_s	9.2(1)	92(1)	30

lasses stage (section 4.1.1.1). For each of the horizontal orthogonal directions a further pair of Helmholtz coils is added, called *fine-tuning coils*. The aim of the fine-tuning coils is to regulate finely the bias field B_0 along x, for compensating daily for the eventual fluctuations or for changing the aspect ratio of the trap. The fine-tuning coils along the y axis are used instead for fixing a quantization axis aligned to the imaging direction during time of flight, as discussed in 4.2.

Trap regimes

The magnetic trap is normally operated within three regimes, differing in the current flowing through the coils. The use of such regimes depends on the experimental need. The three regimes are:

- *high-temperature regime* I_{ht}: the trap is loaded in this configuration and it is used only for the first stage of evaporation (see 4.1.1.2), the sample is in the thermal regime;
- *tight confinement* I_t: final regime with a tight-confined BEC;
- *shallow confinement* I_s: final regime with a shallow-confined BEC.

The design parameters of the magnetic field in the three regimes are reported in table 3.1.

Trap frequencies

The sodium atomic magnetic moment for the ground state is $\mu_{\text{at}} = |m_F| \cdot 700\,\text{kHz}\,\text{G}^{-1}$, dependent on the internal state. The condensate is produced in the state $|1, -1\rangle$, in which losses due to dipolar relaxation are suppressed. The experimentally determined trapping frequencies in the condensation state are reported in table 3.2 for the two regimes I_t and I_s.

MAGNETIC TRAPPING IN A GRAVITATIONAL FIELD Experiments are usually performed on the Earth surface, hence the total potential en-

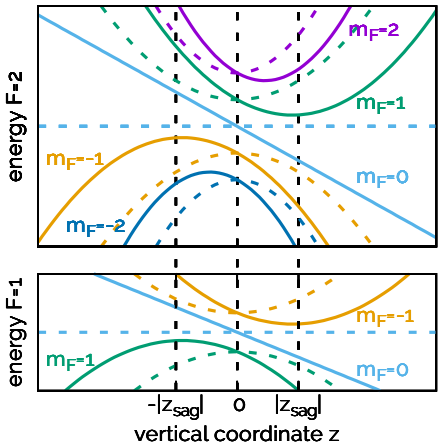

Figure 3.6: Magnetic potentials of the Zeeman states of the two hyperfine groundstates with (continuous line) and without (dashed line) the effect of gravity. The sag for states with $|m_F| = 1$ is reported (z_{sag}), states with $|m_F| = 2$ experience half of this sag.

ergy of the sample must also include the contribution of the gravitational potential, yielding a total potential energy of

$$U_{|F,m_F\rangle}(\vec{r}) \approx \mu_{\text{at}} B_0 + \frac{1}{2} m\omega_\perp^2 \left(y^2 + z^2\right) + \frac{1}{2} m\omega_x^2 x^2 + mgz. \tag{3.6}$$

The effect of gravity on a trapped state is to introduce a displacement in the minimum of the potential, shifting it from the position of the minimum of the magnetic field. This shift, commonly known as *gravitational sag*, is given by

$$z_{\text{sag}} = -\frac{g}{\omega_z^2} = -\frac{g}{\omega_\perp^2}. \tag{3.7}$$

The value of the gravitational sag in our setup is reported in table 3.2. In the case of an anti-trapped state the effect of gravity simply gives an exchanged sign, *i.e*, the maximum of the potential energy is upshifted with respect to the maximum of the matter-field interaction energy. The effect of gravity on the magnetic potential for the different Zeeman states in the $F = 1$ and $F = 2$ ground states is sketched in figure 3.6.

Resonance conditions between Zeeman states

The resonance condition between two internal states ($|F, m_F\rangle$ and $|F + \Delta F, m_F + \Delta m_F\rangle$) clearly depends on the spatial coordinates:

$$h\nu_{\Delta F}^{\Delta m_F}(\vec{r}) = \left| U_{|F+\Delta F, m_F+\Delta m_F\rangle}(\vec{r}) - U_{|F,m_F\rangle}(\vec{r}) \right|. \tag{3.8}$$

Equation (3.8) describes a 3D surface which remains centered on the minimum of the magnetic field independently of the action of gravity, because it acts on all the internal states in the same way and its contribution cancels out from the resonance condition (3.8). Atoms which cross the resonance surface (3.8) can undergo a spin-flip transition, thus changing their internal state. The effectiveness of the state-

changing process depends on the coupling strength between the two levels, *i.e.*, on the Rabi frequency:

$$\hbar\Omega = \mu_B g_J \langle F', m'_F | \vec{J} | F, m_F \rangle \cdot \vec{B}. \tag{3.9}$$

The Rabi frequency expressed in (3.9) depends on the intensity and polarization of the magnetic field because transitions between sublevels of the hyperfine ground state are magnetic dipole ones, being the electronic orbital quantum number constant while only the nuclear and electronic spins change. Selection rules for magnetic dipole transitions are $\Delta m_F = 0, \pm 1$. The polarization of the field influences the coupling strength, favouring the $\Delta m_F = 0$ transition in the case of linear polarization ($\hat{\pi}$) or the $\Delta m_F = \pm 1$ in the case of circular polarization ($\hat{\sigma}_+$ or $\hat{\sigma}_-$).

Outcoupling

By setting a suitable radiofrequency (RF) or microwave (μw) field it is possible to exploit the state-changing resonance to implement a forced evaporation in the magnetic trap (see below in 4.1.1), or to implement the so called *outcoupling* of the sample. Outcoupling means the partial coherent transfer of a part of a sample in another state, which then evolves independently of the original. Outcoupled atoms can then be manipulated and/or imaged without affecting the atoms remained in the trap. The outcoupling technique for implementing real-time imaging of vortices is the central topic of my thesis.

3.4 ELECTRONICS AND CONTROL SYSTEMS

The experimental procedure for creating, manipulating and probing a Bose-Einstein condensate requires a high degree of control over many variables, with a required time precision at the level of 1 µs. The large part of our instrumentation is controlled through a custom digital control system based on *Field-Programmable Gate Arrays* (FPGAs), developed by Marco Prevedelli. FPGA is a technology which permits the implementation of highly customizable digital procedures with the possibility to have a full control over the timing, making it particularly suitable to systems needing a very precise time control. The core of the system is a XILINX SPARTAN 3 (XC3S250E) FPGA based developement board clocked at 10 MHz. The core receives a temporal sequence of instructions via USB from a remote PC, which have to be executed when the communication stops. Each instruction is repeated by the FPGA on a parallel custom bus, composed of 7 address channels and 16 data channel plus a strobe line. The time resolution of the instruction writing is 100 ns, with a maximum instruction rate of 2.5 MHz. Different slave boards are connected to the common bus, they read uniquely the instructions concerning their univocal address. Slave boards can be of three different kinds:

- *digital boards*: each board outputs 16 independent TTL channels. They are used for controlling switches, for triggering data acquisition and for controlling the motion of moving mirrors and shutters;
- *analog boards*: each board mounts a pair of 16 bit digital-to-analog converter (DAC), used for analog programming of power supplies, for controlling IGBTs in the linear regime and for tuning the intensity of RF/μw fields through mixers;
- *RF boards*: a RF board is equipped with a DDS chip (Analog Devices AD9958), which outputs RF signals through two independent channels in the range between 200 kHz and 140 MHz, with an amplitude up to 13 dBm. The DDS is programmed through a microcontroller PIC18F2550, which interpretes the instruction from the bus and reads the parameters for the programming from a look-up table (LUT). RF boards are used to generate the signals for controlling acusto-optic-modulators and RF-forced evaporation.

Because of their large number, slave boards are connected on different buses driven by two separated identical FPGAs, which are placed in different locations in the laboratory to permit easier access to them. This avoids a long data bus, reducing the cross-talk between its lines and hence improving the overall reliability. The two FPGAs are synchronized by an external microcontroller (Arduino duemilanove) only when the USB programming of both is finished, to avoid any jitter in the execution of the actions.

The binary instructions for the FPGAs are generated starting from a human-readable list of actions. The list of actions can be edited through a specifically designed Python software (`https://github.com/simondona/exp-control-bec-tn`), which also produces the binary executable for the FPGAs and programs them.

3.5 IMAGING SYSTEM

The imaging system uses different two-lens telescopes with different magnifications along the horizontal and axial directions. Five CCD cameras are used for imaging the sample. When imaging is performed after long time of flight low-magnification ($M = -1.3$) setups are used, while in the case of short expansion, as in the case of the real-time imaging described in the next chapter, imaging with a magnification $M = -2$ is implemented. For obtaining a high frame rate in the real-time imaging two cameras, sharing the same telescope, are used along the horizontal radial direction. The high resolution and magnification imaging for real-time applications uses as objective lens an achromatic doublet with focal length $f = 75\,\text{mm}$, placed

one focal length from the atoms. The diffraction limit of such a system is $\sim 2\,\mu m$, while the depth of focus is $\sim 50\,\mu m$.

The cameras used for imaging are STINGRAY F-201B with CCD technology, connected to PC via FIREWIRE 1394-B protocol. The CCD sensor is $1624\,px \times 1234\,px$, with a pixel size of $4.4\,\mu m$. In order to implement imaging with a high frame rate, the timing of the CCD reading and transmission to the PC have to be matched. Acquisition and transmission of the data depend on the size in pixels of the *area of interest*, *ie.*, the region of the CCD with the useful signal, which can be selected via software. The maximum frame rate achievable in the reading of the employed CCD depends on the number of vertical lines A_h in the area of interest:

$$fps_{CCD}^{max} = \frac{1}{344.9\,\mu s + A_h \cdot 54.81\,\mu s + (1238 - A_h) \cdot 7.14\,\mu s}. \quad (3.10)$$

Transmission in B-mode of the FIREWIRE has to be enabled, permitting a full-duplex communication up to $800\,Mbit\,s^{-1}$. The limit imposed on the frame rate by the communication bandwidth is

$$fps_{com}^{max} = \frac{p}{A_h \cdot A_w \cdot BD \cdot 125\,\mu s}, \quad (3.11)$$

it depends on both the sizes (A_h and A_w) of the area of interest, on the packet size p in bit ($p = 8192\,bit$ for a full-duplex B-FIREWIRE) and on the depth of a single pixel BD, which is of $16\,bit$ for our cameras. The maximum performance on the communication side can be reached in case of more than one camera connected on the same PC only using the PCI EXPRESS and/or PCI $64\,bit$ slots. The acquisition can occur only if

$$fps_{CCD} < fps_{com}. \quad (3.12)$$

Acquisition is actually done through a LABVIEW software, which calculates the optical density of the sample starting from the raw images from the camera. Optical density is saved in binary mode in a file which is then elaborated through a Python software written by Gregor Thalhammer. This software performs 2D fits of various types and takes care of saving the fit parameters and the optical density matrix in a specific directory tree. The matrix is saved in a customized binary format that we call `*.sis`. A Python implementation for reading and writing such files can be found at `https://github.com/SimoneSerafini/readsis`. This library actually includes a more articulated header in view of future revisions and improvements of the entire acquisition process.

4 EXPERIMENTAL TECHNIQUES

CONTENTS

In this chapter I will describe the experimental production of Bose-Einstein condensates with the apparatus described in chapter 3. I will describe the experimental techniques used in our experiments, describing in detail the imaging techniques used for probing vortices.

4.1 THE BEC PRODUCTION

Our experimental sequence to achieve Bose-Einstein condensation is composed of a pre-cooling stage followed by a magnetic trapping stage with evaporative cooling. In the pre-cooling stage a magneto-optical trap with dark-spot technique (DS-MOT) and an optical molasses phase are implemented. The pre-cooling stage is described in section 4.1.1. The crossing of the BEC phase-transition needs a closer insight, being crucial for the vortex production in our experiments. Details on this stage are reported in section 4.1.2. In the last section 4.1.3 the evolution of the sample and any manipulation after the BEC transition are described.

4.1.1 From Hot to Cold Atoms

BEC is normally obtained in conservative traps like magnetic or far-detuned optical dipole traps. This is because the photon re-absorption limits the minimum temperature achievable through magneto-optical traps, which uses near-resonant light. Conservative traps are normally shallow, requiring a pre-cooling stage exploiting in this case the advantages of laser cooling.

4.1.1.1 *Pre-cooling Stage*

A pre-cooling stage is necessary for loading our magnetic trap, whose depth is of the order of 4 mK. Moreover the sample from the pre-cooling stage should have a good geometrical matching with the equilibrium distribution of a sample at the same temperature confined in the magnetic trap. This requirement, commonly known as mode-matching, is sometimes difficult to obtain and the loading into the magnetic trap heats up the sample. Thus the temperature of the sample has to be well below the magnetic trap depth.

DS-MOT We implement a magneto-optical trap with the repumper light provided independently from the cooling light and screened out from the center of the sample in order to reduce the effect of re-absorption, obtaining higher values of densities than traditional magneto-optical traps (Ketterle, K. Davis, et al. 1993). Our DS-MOT consists of six independent cooling laser beams with large diameter (2.5 cm), counterpropagating in pairs along the three orthogonal directions. All beams are circularly polarized with the appropriate helicities for magneto-optical trapping. In the intersection region of the cooling beams a 3D-magnetic-quadrupole field with vertical axis, along which the gradient is $\sim 12\,\mathrm{G\,cm^{-1}}$, is present. This field is generated by the two quadrupole coils described in section 3.3, used also for magnetic trapping. The repumper light is carried by an independent beam, which passes through a glass plate with an optically dense circle in the central region. The shadow of this circle is imaged at the the center of the trap. In this way the outer region efficiently captures and cools down atoms coming from the atomic source, while in the inner region the colder atoms are accumulated in the dark state.

The DS-MOT loading procedure lasts between 8 s and 12 s; we can use this duration as a free parameter for tuning the number of atoms in the final BEC. Atoms are loaded from the atomic source by switching on a pushing beam aligned to the 2D-MOT in the HV region and passing through the differential pumping channel (section 3.2): the beam blows atoms from the 2D-MOT into the science chamber, where they are finally captured by the DS-MOT. At the end of this stage the sample has a phase-space density of the order of 1×10^{-6}.

OPTICAL MOLASSES An all-optical cooling stage without trapping effects is subsequently performed. The optical molasses phase lasts 5 ms, during which the intensity and the detuning of cooling and repumping light are tuned to enhance sub-Doppler cooling mechanisms. During this phase the magnetic field is switched off. The residual environmental magnetic fields are cancelled out through the three orthogonal pairs of shim coils, which operate not only during optical molasses but during the entire procedure. This stage results in an improvement of one order of magnitude in the phase-space density.

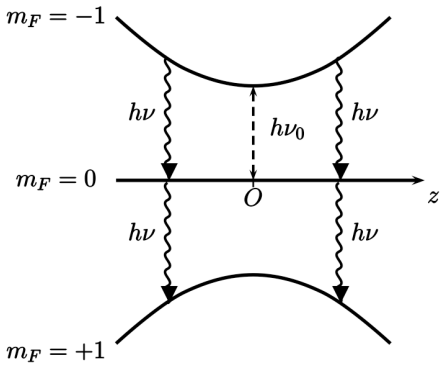

Figure 4.1: Sketch of RF-forced evaporation im a magnetic trap, from Cohen-Tannoudji et al. 2011.

Gray molasses

We implemented also a gray molasses cooling scheme for the first time on sodium atoms (Colzi et al. 2016) in order to end up the pre-cooling stage with higher phase-space densities and to achieve at the end of the entire procedure a larger condensate. The gray molasses technique allows to reach a phase-space density of 1×10^{-4}. Nevertheless the direct loading of samples cooled with gray molasses to a Ioffe-Pritchard magnetic trap revealed to be unfeasible, because of the non-ideal mode-matching which cancels out completely the improvements achieved via gray molasses. Moreover the loading is strongly demanding for the hardware, requiring to operate IGBTs in the linear mode at very high current, making the system prone to failures.

4.1.1.2 *Magnetic-trapping Stage*

After the pre-cooling stage atoms are loaded into the magnetic trap. The magnetic field in the Ioffe-Pritchard configuration is switched on abruptly with the maximum strength (I_{ht} regime). The sample is heated due to the non-phase-matched transition[1], but the high stability of the trap permits long evaporations with a high efficiency, making a smooth loading not so necessary. The hot sample experiences a potential which is not harmonic but feels a linear radial confinement (high temperature limit of equation (3.3)). The linear shape of the confinement enhances the elastic collisional rate, favouring in this way the efficiency of the evaporation.

RF-FORCED EVAPORATION The magnetic trap is conservative, thus a cooling mechanism has to be added to reach quantum degeneracy. The most effective cooling mechanism in magnetic traps is the *radio-frequency-forced evaporation*. RF-forced evaporation consists in contin-

1 Phase-matching requires, in our setup, complications as the loading with a high bias field to make the potential less anisotropic makes the trap frequncies very shallow, enhancing the gravitational sag. MOT is not affected by the sag and a smooth loading requires the displacement of the trap center to match the MOT center.

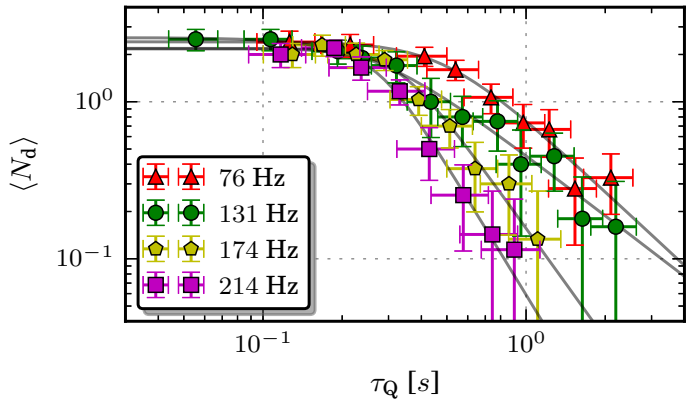

Figure 4.2: Kibble-Zurek scaling, from Donadello, Serafini, Bienaimé, et al. 2016.

uously removing atoms from the high energy tail of the thermal distribution. The process can be visualized as an iterated removal of hot atoms followed by a re-thermalization at a lower temperature. The evaporation mechanism is implemented exploiting the inhomogeneous Zeeman splitting of the atomic levels in the magnetic trap: only high-energy atoms can climb the confining potential (equation (3.5)) up to a threshold energy fixed by a spin-flip transition between the trapped and untrapped state (figure 4.1). Highly energetic atoms are then expelled from the trap because of the change in their magnetic moments. The evaporation mechanism can be forced ramping down the frequency toward the bottom value $h\nu_0$.

Trap decompression

During the evaporation the trap is decompressed, smoothly changing the current through the coils to go from the regime I_{ht} to I_t. The decompression makes the confinement shallower reducing the density of the sample. This stage is necessary to reduce losses due to three-body inelastic collisions, which are the main source of losses at high density (Ketterle, Durfee, et al. 1999). Evaporation continues during decompression and after it.

4.1.2 Crossing the Transition and Generating Vortices

The part of the evaporation in which the BEC threshold is crossed is particularly important because the speed in which the BEC transition is crossed influences the number of defect generated through the Kibble-Zurek mechanism. The characterization of KZM in our system was investigated by Donadello, Serafini, Bienaimé, et al. 2016, varying also the trap aspect ratio. The rate of change in the radiofrequency clearly produces a temperature quench of the system. The cooling rate in our setup is $4.5\,\mathrm{nK\,kHz^{-1}}$, while the critical temperature depends only slightly on the slope of the frequency ramp, at least when the cooling rate is not too fast. The quench time is then

Table 4.1: Typical numbers of the studied BEC: μ is the chemical potential, $\mathscr{R}_{x,\perp}$ are the Thomas-Fermi radii, ξ is the healing length and Na/a_{ho} is the Thomas-Fermi parameter.

Regime	N	μ		$\mathscr{R}_x$	$\mathscr{R}_\perp$	ξ	Na/a_{ho}
		$[\hbar\omega_\perp]$	[kHz]	[µm]	[µm]	[nm]	[AD]
I_t	10×10^6	27	3.6	140	14	240	10 250
I_t	20×10^6	36	4.7	150	15	200	20 500
I_s	20×10^6	34	3.1	180	18	260	17 100

determined by the relation $\tau_{\mathrm{Q}} = -T_c \left(\frac{\partial T}{\partial \nu}\frac{\partial \nu}{\partial t}\right)^{-1}$. The dependence of the number of defects as a function of the quench time defines the KZ scaling, and is measured in our experiments after a waiting time of 250 ms to permit the relaxation of the system hence permitting the counting of defects (all the experiments reported in this thesis deal with a waiting time after the transition, see section 4.1.3). The rate of the evaporation represents the tuning knob for regulating the number of vortices in the BEC under study. The scaling reported in figure 4.2 is an indicative starting point that can be fine-tuned during the experiment to take into account fluctuations in the initial conditions, like in the atom number. The number of defects generated through KZM in fact depends also on the atom number (Lamporesi, Donadello, Serafini, and Ferrari 2013).

4.1.3 Manipulations of the Condensate

After the temperature quench our sample is highly turbulent, as pointed out by numerical simulations done by N. Proukakis 2016. Performing imaging near to the transition does not give useful information because of the difficulties in the interpretation of the signal and the recognition of the defects. A waiting time after the quench across the transition is needed to let the system relax toward a stationary state. After this evolution time, lasting hundreds of milliseconds, the sample can be imaged.

The characteristic quantities for the typical condensates studied in our experiments are reported in table 4.1. The chemical potential is expressed in terms of the energy quanta of the transverse confinement and in frequency units. The axial and Thomas-Fermi radii are reported together with the healing length.

RF SHIELDING In order to increase the lifetime of the sample, reducing the loss rate due to inelastic collisions with hot atoms, a technique called *radiofrequency shielding* is implemented during the time elapsing from the end of the evaporation ramp and the subsequent manip-

ulations or probing. The technique is applied if not interfering with the experiment. A radiofrequency field with a fixed frequency value is kept on during the evolution time. Such a frequency value is chosen to set a resonance surface spatially far away from the condensate, in order to avoid any further evaporation. In this way, high energy atoms, which can cross that surface, are pumped to the non-trapped states, depleting the hot atoms from the region where the condensate lies. Typical values used in our experiments are 100 kHz ÷ 300 kHz above the trap bottom.

TRAP BOTTOM To implement the outcoupling techiques described below (section 4.2), a precise determination and control of the trap bottom is required. A simple but not very accurate procedure for controlling the trap bottom consists in evaporating the system to the level for which the Zeeman splitting between the trapped and untrapped levels at the center of the trap is at the desired value, and then regulating the current through the compensation coils until atoms disappear. In this way the effective bias field B_0 is finely tuned to produce the desired splitting. This procedure is done daily to compensate for possible fluctuations of the environmental magnetic fields. The accuracy of this procedure is however poor, because the RF field used for the evaporation couples the levels on an energy range given by the Rabi frequency, which is in our case $\sim$ 20 kHz.

A more precise characterization of the trap bottom can be implemented exploiting a fixed-time atom-laser outcoupling at very low intensity, to reduce the coupling Rabi frequency. Such a technique is strictly related to the novel real-time imaging technique developed in our group and described in section 4.2.3. The effect of gravity modifies the resonance condition as described in section 3.3, thus radiating the condensate with a single frequency field the atomic spin-flip occurs on a surface which dissects almost horizontally the sample, and by changing the frequency the height of the section changes. More details about this will be given in section 4.2.3.1, introducing the novel imaging technique. After a fixed outcoupling time the residual atom number is measured using standard absorption imaging after time of flight. The procedure is the following: a sample is prepared, at the end of the evaporation ramp a single frequency field at very low intensity is switched on and kept for 50 ms, after

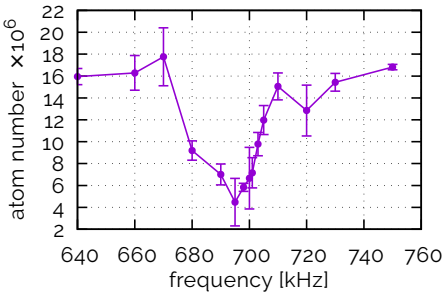

Figure 4.3: The atom number remaining in the condensate as a function of the weak RF outcoupling for the determination of the trap bottom in the I_s configuration.

Table 4.2: Trap bottom value.

	ν_0 [MHz]	B_0 [G]
I_t	1.187	1.70
I_s	0.692	0.98

which the trap is switched off and the residual atom number is measured. The procedure is repeated many times, varying the low-power-field frequency, obtaining the graph reported in figure 4.3.

The trap bottoms measured for the two field configurations are reported in table 4.2. The width of the dip in figure 4.3 is given by the vertical extension of the condensate in terms of the resonance with the outcoupling transition: such width is larger than the chemical potential because of the quadratic behaviour of the magnetic field.

SECOND DECOMPRESSION When implementing the novel imaging technique described in section 4.2.3.1, where imaging is performed on samples far from the trap center in the presence of the trapping field, the need to reduce the magnitude of the magnetic field experienced in the imaging region arises. In this case the sample undergoes to a second decompression of the trap after the end of the evaporation, passing from the I_t strength to the I_s one. This decompression halves in this way the radial gradient of the magnetic field. The modification of the trapping potential in the presence of a very cold sample requires the contemporary modification of the trap bottom. The modification of the trap strength indeed modifies the Zeeman splitting of the atomic levels and hence the value of the trap bottom. In some cases the fine control of the trap bottom is crucial, hence an adiabatic tuning of the trap bottom between the values reported in table 4.2 has to be performed during the trap decompression[2].

4.2 PROBING AND IMAGING TECHNIQUES

In all the experiments described in the present thesis the characterization of the samples is carried on through resonant absorption imaging. In the present section I will report the details of the different implementations used for this work. Such implementations are:

- standard destructive absorption imaging applied along the three orthogonal directions, used for the characterization of the expansion properties of vortices (section 5.1.2), and applied also

2 In the case of decompression at high temperature, as done during the forced evaporation, such care is not justified because the energy variation of the trap bottom is negligible with respect to the thermal energy of the sample.

for the detection of the output of an atomic Bragg interferometer. A long time of flight is needed for samples with a large atom number to reduce the optical density to suitable values and to make clearly visible the defects in the condensate;

- *real-time minimally destructive* implementations of absorption imaging, implemented to access the dynamics of stochastically generated vortices. In particular two techniques were applied:
  - *μ-Wave Pulsed Minimally Destructive* (μw-PMD), mainly used for the characterization of the dynamics of single vortices in our elongated BEC (section 5.2.1);
  - *Radiofrequency Sweep Minimally Destructive* (rf-SMD), novel technique developed for the study of vortex-vortex interaction processes (chapter 6).

Their applications will be described in the following chapters.

ABSORPTION IMAGING All the experiments described in this work are based on the *absorption imaging* technique. As introduced in section 2.3, the absorption of resonant light by a dilute sample can be described through a generalized Lambert-Beer law:

$$I(x,z) = I_0(x,z)e^{-\mathcal{O}}. \tag{4.1}$$

The optical density of a sample is experimentally determined measuring the intensities of the light transmitted through the sample and of the reference beam:

$$\mathcal{O}(y,z) = -\log \frac{I(y,z)}{I_0(y,z)}. \tag{4.2}$$

The contribution of the intrinsic electronic noise of the sensor can be reduced by subtracting the signal from the CCD taken in dark condition from the intensity profiles in equation (4.2).

Magnetic levitation

When the optical density of the sample is too high a faithful determination of the total number of atoms in the sample is not possible, because for an optically thick cloud the generalized Lambert-Beer's law ceases to be valid. Above a value of 2 the measurement of the optical density of the sample is not accurate. To ensure reliability, then, the sample has to expand freely for a sufficient long time in order to reduce its spatial density. In the case of large condensates, like in the experiments described here, the required expansion time can be quite long. Long times of flight have a drawback: the sample, or part of it, might end up outside the imaging region because of the effect of gravity. A solution could be to set the imaging region below the trapping region, but making the system hard to tune for different values of time of flight or for in-situ imaging. Another way to reach very long time of flight, but keeping a high flexibility, is to implement a magnetic levitation. As described in the section devoted to the description

of the magnetic trap (section 3.3), a single coil with vertical axis can be used to generate a magnetic field gradient that compensates for the gravity in the position of the trapped sample. In this way the sample can freely expand remaining centered in the imaging region, independently of the chosen time of flight. The added magnetic field introduces a negligible horizontal confinement. This residual confinement was estimated looking at the anisotropy of a BEC in the yz plane after a given expansion. By comparing the expansion in the levitating field to what is expected integrating the expansion equations proposed by Castin et al. 1996, we estimate a residual curvature in the horizontal xy plane to produce a residual harmonic confinement of 1 Hz, to be compared to the typical expansion time of 180 ms.

Imaging efficiency

Absorption imaging requires atoms to cycle on a closed transition while excited by the probe beam. This condition depends on the coupling between the hyperfine levels connected by the probe light and on their magnetic sublevels, populated according to the polarization of the probing beam. Normally the imaging is performed polarizing the sample with a magnetic field along the imaging axis through a pair of fine-tuning coils (see 3.3), and using circularly polarized light in order to accumulate atoms in the stretched levels, avoiding optical pumping into dark states. Imaging in-situ samples or outcoupled samples in the presence of the magnetic trapping field imposes a not ideal configuration for transverse imaging because the bias field of the magnetic trap points along the axis of the sample. Optical pumping is thus unavoidable and reduces the absorption cross-section (equation (2.4)) to about $\sim 85\%$ of the maximum value. This ratio was determined by comparing the absorption in the presence of the optimal biasing first and then with the axial bias field of the magnetic trap. The ratio between the atom number from the fits gives the attenuation due to depumped imaging in our setup. This effect also masks the true atom number, underestimating it, when imaging is performed at the same time along the three orthogonal directions, because of the presence of probing light with arbitrary polarization is in this case unavoidable.

Digital filtering

Often raw images show interference fringes that strongly reduce the SNR, especially when imaging is performed along the axis x of the trap, where the optical density is about $1/4$ of the radial one because of the oblate shape of the sample after the time of flight. Visibility of defects can thus be strongly reduced. To overcome this limitation we apply a digital filtering procedure to the raw images, which can be combined and tuned for each particular necessity. The used filtering procedures are:

- *fringe removal through FFT filtering;*
- *contrast tuning through gaussian filtering.*

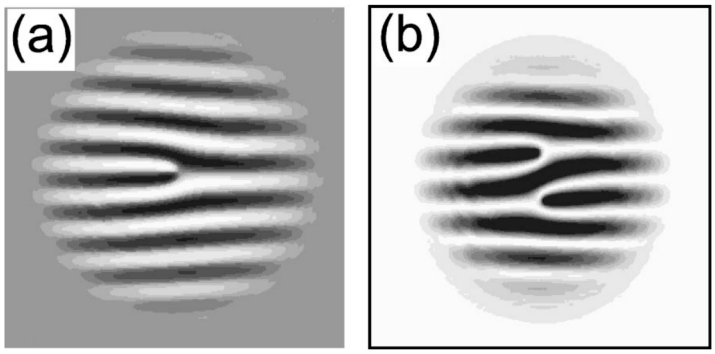

Figure 4.4: Dislocations in the fringe pattern due to the same vortex probed through heterodyne **(a)** and homodyne **(b)** technique. From Dobrek et al. 1999.

4.2.1 Bragg Interferometry

In order to access the phase profile of a condensate the analogy between matter waves and optical waves can be exploited: BEC is a system with a well-defined macroscopic wavefunction, hence when two condensates overlap the interference of the two wavefunctions produces a fringe pattern, like two classical coherent optical waves. Let us consider two point-like sources of a matter wave located in the two points A and B, separated by a distance d. If the generated matter waves $\Psi_{A,B}$ are let to expand for a time t_{ToF}, the overlapping region of the two waves will show an interference fringe pattern in the density, given by $|\Psi_A(t_{\mathrm{ToT}}) + \Psi_B(t_{\mathrm{ToT}})|^2$. The fringe spacing λ_{ph} depends on the time of flight and on the initial relative distance d:

$$\lambda_{\mathrm{ph}} = \frac{h t_{\mathrm{ToF}}}{m d}. \tag{4.3}$$

The first experimental demonstration of the interference pattern coming from the overlap of two condensates was given by Andrews et al. 1997.

A matter-wave interferometer can thus be implemented making the sample interfere with a reference condensate to measure the relative phase through the fringe pattern appearing in the density. The reference condensate can be an independent one (*heterodyne detection*) or a copy of the sample condensate (*homodyne detection*). The presence of a vortex in the sample condensate causes in the case of heterodyne detection a fringe dislocation in the interference pattern in correspondence of the vortex core, as reported in figure 4.4 **(a)**. The dislocation is due to the phase winding around the vortex core. If the reference condensate is a copy of the sample BEC the fringe pattern shows a double dislocation with opposite orientation, because the two interfering condensates have the same helicity but opposite velocity, figure 4.4 **(b)**. The interferometric technique for probing vortices in BEC was proposed theoretically by Bolda et al. 1998, and experimen-

tally demonstrated by Inouye et al. 2001 in the heterodyne case and by Chevy, Madison, Bretin, et al. 2001 in the homodyne case.

We implemented a homodyne type interferometer to probe vorticity, requiring thus to produce a copy of the sample BEC and then to let the two matter waves to overlap.

Bragg beam splitter

In our interferometer the reference copy is produced by means of a *Bragg diffraction* of the condensate by an optical grating, following the scheme implemented by Kozuma et al. 1999. The use of Bragg diffraction of a matter wave from an optical lattice as a very effective beam splitter was proposed by Dobrek et al. 1999. An optical lattice is created in the crossing region of a pair of light beams (see figure 4.5 **(a)**), with a relative angle θ. The two beams have a different k vector and a relative detuning δ. The conservation of momentum and energy in the interaction between the matter wave (BEC) and the optical lattice gives:

$$|\vec{q}| = 2n\hbar k \sin\theta \tag{4.4}$$

$$\Delta E_{BEC} = \beta E_{\text{rec}}, \tag{4.5}$$

where n is the order of the process, meaning $2n$ photons are involved in the transition, $\vec{q}$ is the exchanged momentum and ΔE_{BEC} is the energy acquired by the BEC in the process, which can be expressed in units of the recoil energy as β. Hence a condensate with an initial momentum $\vec{p}_i$ ends up with a momentum $\vec{p}_f = \vec{p}_i + \vec{q}$, being $\vec{q} = \hbar\left(\vec{k}_2 - \vec{k}_1\right)$, as depicted in figure 4.5 **(a)**, if the exchanged energy is sufficient. If the condensate is intially at rest, $\vec{p}_i = \vec{0}$, energy conservation can be written as

$$\Delta E_{BEC} = \beta E_{\text{rec}} = n^2\delta. \tag{4.6}$$

The process can be interpreted as a $2n$-photon Raman transition, as depicted in figure 4.5 **(b)** for the case $n = 1$. An overall detuning Δ ensures that light is off-resonant with respect to the excited states, leading to a negligible resonant scatterning. The two-photon exchange gives to the BEC in the state $|g, \vec{p}_i = \vec{0}\rangle$ sufficient energy to access the state $|g, \vec{p}_f = \vec{q}\rangle$, if conservation laws (4.5) and (4.6) are satisfied. The BEC remains in the same internal state $|g\rangle$, it acquires the kinetic energy $q^2/2m$, and it recoils in the direction of the exchanged momentum.

The momentum transfer affects a fraction of the population of the BEC, depending on the two-photon Rabi frequency Ω_2 and on the duration τ and shape of the light pulse illuminating the condensate. The two-photon Rabi frequency is given by the relation:

$$\Omega_2 = \frac{I|\langle d\rangle|^2}{2c\epsilon_0\hbar^2\Delta}, \tag{4.7}$$

where $|\langle d\rangle| = 2.988 \times 10^{-29}\,\text{C m}$ is the dipole moment of the optical transition for sodium, from which the light is detuned by Δ, I is the

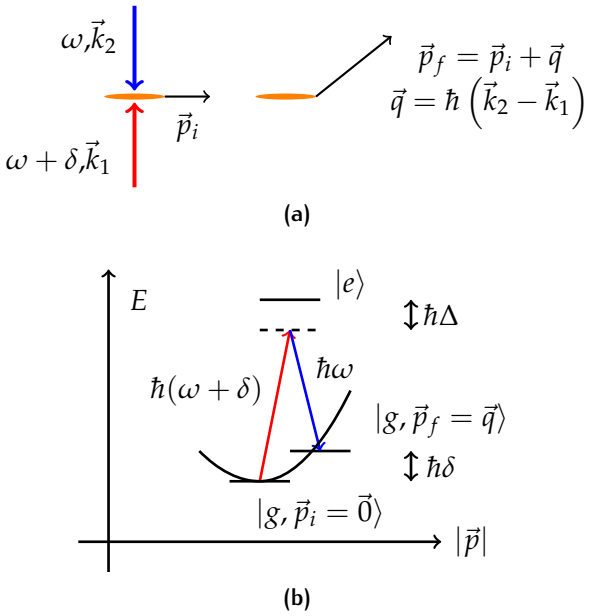

Figure 4.5: (a) Schematic representation of the matter wave Bragg scattering, the condensate is in orange, while in red and blue are the two laser beams. **(b)** Representation of the Bragg scattering as a Raman process.

intensity of each optical beam, c is the light speed and ϵ_0 is the vacuum permittivity. In the case of a rectangular pulse, the phase factor $\Omega_2\tau$ gives the efficiency of the transfer: for $\Omega_2\tau = \frac{\pi}{2}$ we get a 50% of transfer, ending with a wavefunction which is an equal superposition of the initial state $|g,\vec{p}_i\rangle$ and of the state $|g,\vec{p}_f = \vec{p}_i + \vec{q}\rangle$.

Complete interferometer

We implement an open-type $\frac{\pi}{2} - \frac{\pi}{2}$ interferometer. A first Bragg pulse, at t_1 after the release of the atoms from the trap, coherently splits the initial wavefunction in two, one is stationary as the original condensate, the other is travelling along the direction of the exchanged momentum. After a given time t_2, a second Bragg pulse is applied. In this way, after the second pulse, two pairs of copies are present: one pair is stationary while the second is travelling. The second pulse is needed to make the copies with the same velocity to overlap after a time of flight t_3, while copies with different velocities become well spatially separated. A schematic representation of the whole process is reported in figure 4.6. The time span between the two pulses defines the relative distance d between the interfering copies, which, in combination with the time of flight t_3, gives the fringe spacing according to equation (4.3). At the end, the two output ports of the interferometer show the interference pattern revealing the relative phase of the two overlapping pairs of condensates.

Experimental implementation

We implemented the Bragg matter-wave beam splitter using two light beams off-resonant with respect to the $D2$ line by $\Delta/2\pi = -1.771\,\text{GHz}$. The two beams lie in the xz plane and have a relative

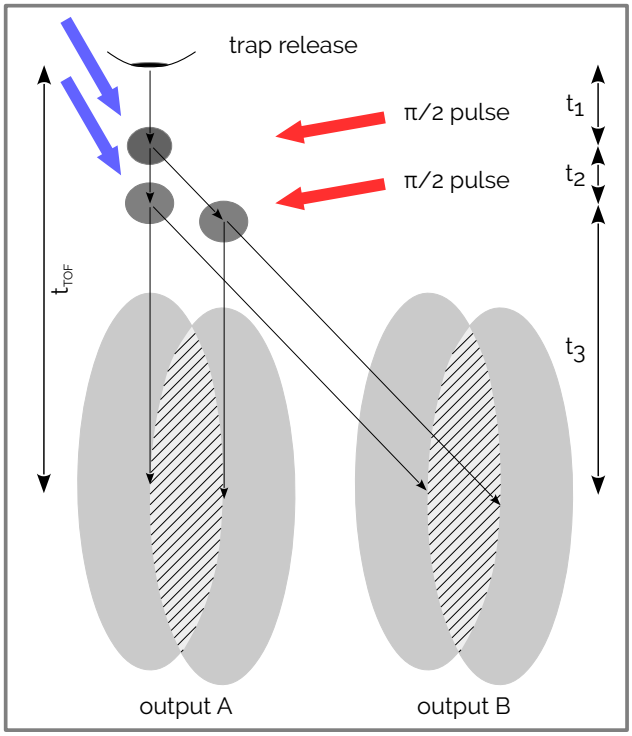

Figure 4.6: Scheme of the two-pulse Bragg interferometer.

angle $\theta \approx 110°$. The geometry of the beams gives an acquired velocity for the first-order process of

$$v_B = 2v_{\text{rec}} \sin\theta \approx 4.8\,\text{cm}\,\text{s}^{-1}, \tag{4.8}$$

where $v_{\text{rec}} = 2.9\,\text{cm}\,\text{s}^{-1}$ is the recoil velocity for the optical photon $v_{\text{rec}} = \hbar k/m = h/(m\lambda)$, where $\lambda = 589\,\text{nm}$ is the $D2$ transition wavelength. The energy exchanged is $\beta = (2\sin\theta)^2$, expressed in units of the recoil energy $E_{\text{rec}}/h = 25\,\text{kHz}$. The relative detuning between the two beams is then expected to be $\sim 67\,\text{kHz}$ in our geometry. The beam intensity is $12\,\text{mW}\,\text{cm}^{-2}$ each, leading to a two-photon Rabi frequency $\Omega_2/2\pi \sim 25\,\text{kHz}$. A $\frac{\pi}{2}$ pulse then has to be $\sim 8\,\mu\text{s}$ long.

The first Bragg pulse is applied at time $t_1 = 20\,\text{ms}$ after the release of the magnetic trap. This waiting time is necessary to reduce the density, hence avoiding strong interactions between the two created copies. The separation times $t_2 = 1.5\,\text{ms}$ defines the distance between the interfering copies $d = v_B t_2 \approx 72\,\mu\text{m}$. The time of flight $t_3 = 98.5\,\text{ms}$ is chosen to have a total expansion time of $120\,\text{ms}$ from the trap release, which is sufficient to lower the optical density to values compatible to absorption imaging. The expected fringe spacing is $\lambda_{ph} \approx 25\,\mu\text{m}$, sufficiently larger than the imaging resolution ($\sim 5\,\mu\text{m}$).

The experimental results of the application of such a technique will be discussed in chapter 5, where the technique is used to explore the properties of the solitonic vortex after expansion (section 5.1.2).

4.2.2 μ-Wave Pulsed Minimally Destructive Imaging

This method is based on ideas discussed in Freilich et al. 2010; Ramanathan et al. 2012, where a partial transfer of atoms is applied from the trapped state to an auxiliary state that has a cycling transition for the imaging procedure, while atoms remaining in the trap are essentially unperturbed by the imaging light since it is out of resonance. In this way a repeatable minimally destructive imaging can be implemented directly in-situ (Ramanathan et al. 2012) or after a time of flight (Freilich et al. 2010). The starting state is the magnetically trapped state $|1,-1\rangle$, which is dark with respect to the cycling transition $F = 2 \leftrightarrow F' = 3$. A microwave field can be used to couple energy states between the two different hyperfine ground-states $F = 1$ and $F = 2$. The microwave radiation induces then Rabi oscillations between the coupled states. Since the selection rules for the magnetic dipole transition[3] require $\Delta m_F = 0, \pm 1$, the auxiliary states accessible from the trapped BEC state are $|2,-2\rangle$, $|2,-1\rangle$ and $|2,0\rangle$. Transitions with $\Delta m_F = \pm 1$ can be triggered through circularly polarized fields, while for $\Delta m_F = 0$ a linear polarization is needed, making evident the necessity of having different antennas for the two purposes. The internal state dynamics is well described in terms of Rabi oscillations with a Rabi frequency

$$\hbar\Omega = \mu_B g_J \langle F', m'_F | \vec{J} | F, m_F \rangle \cdot \vec{B}. \tag{4.9}$$

The probability for an atom to be measured in the upper hyperfine state oscillates in time as

$$P = \frac{\Omega^2}{\Omega^2 + \Delta^2} \sin^2\left(\frac{t}{2}\sqrt{\Omega^2 + \Delta^2}\right), \tag{4.10}$$

Pulse width

where Δ is the detuning from the resonance.

Extraction can be approximated as uniform if the intensity of the pulse is sufficiently high ($\Omega \gg \Delta$) and if the pulse duration is sufficiently short ($\Omega\tau \ll 1$). Indeed a short enough pulse has a spectral width wide enough to cover the resonance frequency dispersion due to the finite size of the condensate in the magnetic trap. The relation between pulse duration τ and the spectral width $\Delta\omega$ (FWHM) is

$$\tau\Delta\omega = 2\pi K, \tag{4.11}$$

Transition frequencies

where K depends on the envelope in time of the pulse: for a rectangular one $K \approx 0.443$.

The resonance frequencies can be determined knowing the zero-field hyperfine splitting of the ground state ν_{hf} and the splitting ν_0 between Zeeman sublevels due to the bias magnetic field of the trap.

3 Only electronic and nuclear spin are involved in microwave transitions between hyperfine levels, being the electron orbital quantum number constant.

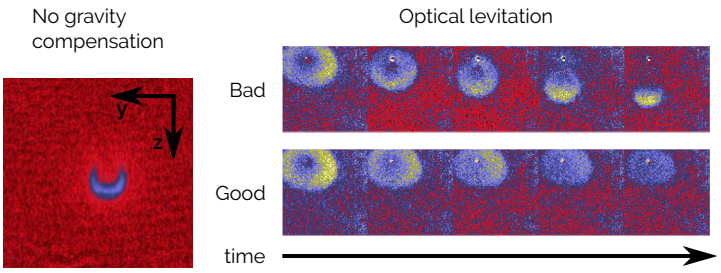

Figure 4.7: On the left the axial view of the outcoupled sample after 5 ms of expansion without any compensation is shown. On the right the same view is depicted in a sequence of 3.5 ms expansions every 100 ms, when a bad (top) and good (bottom) optical gravity compensation is implemented.

The resonance condition between states $|1, m_1\rangle$ and $|2, m_2\rangle$ can be written as

$$\nu_{\mu w}^{m_1 \to m_2} = \nu_{\mathrm{hf}} - m_1 \nu_0 + m_2 \nu_0, \tag{4.12}$$

where the different signs are determined by the opposite Landé g_F factors for the states $|1, m_1\rangle$ and $|2, m_2\rangle$. Relation (4.12) is valid only near the trap center, where the magnetic field is low and hence the Zeeman shift is in the linear regime.

State selection: transfer efficiency and losses

The three possible auxiliary states differ for the efficiency of the transfer and for the stability against inelastic collisions. The most effective is the doubly polarized state $|2, -2\rangle$ because of two reasons:

- the transition $|1, -1\rangle \to |2, -2\rangle$ has the largest Clebsch-Gordan coefficient, hence a stronger coupling at equal intensity;
- suppression of the dipolar relaxation losses.

4.2.2.1 *Experimental implementation*

I will now describe the details of the implementation of the μw-PMD technique in our system, reporting the difficulties faced and the devised solutions.

CONTROLLING THE EXPANSION The main difference between our implementation and the one by Freilich et al. 2010 is that the imaging direction does not coincide with the direction along which vortices are aligned. Such a difference raises some notable issues in our implementation, such as anisotropic expansion of extracted atoms in the plane orthogonal to the imaging direction because of the distortion induced by mean-field interaction with the trapped sample and gravity. An example of the anisotropic expansion, when imaged along the trap axis, is reported in figure 4.7. Indeed during the first instants of the expansion the outcoupled part and the trapped condensate interact through the mean field term, creating a depletion in the extracted cloud. Such a depletion takes the shape of a half-moon when

the imaging is performed along the axis of the BEC, as reported in figure 4.7, because of the fall in the gravity field. This effect is deleterious for observing vortices also along the radial imaging. In order to solve this issue two points have to be considered:

- compensation for the effect of gravity to make the distortion isotropic;
- reduction of the effect of mean-field interaction to limit the distortion.

Optical levitation

To avoid the anisotropic distortion of figure 4.7 which makes impossible to perform reliable fits to the optical density, we can compensate for the gravity fall during the first instants of the expansion in order to have an isotropic expansion around the trapped BEC. Moreover gravity can introduce top-bottom asymmetry in the extraction because of the gravitational sag of the magnetically trapped sample with respect to the resonant region. To center the BEC in the outcoupling resonant region, the trapping potential must be engineered through the use of optical potentials. We used a far blue-detuned light beam to realize a repulsive potential for the atoms. A gaussian beam of 532 nm light is used, its profile and power P determine the gaussian shape and the strength of an optical potential $OP(P,h)$, where h is the transverse coordinate of the beam. In the position of the flex, *i.e.*, at half of the waist w_0, the potential has null curvature, thus equating its gradient to the gravitational potential, *i.e.*,

$$\frac{\partial OP(P,h)}{\partial h}\Big|_{h=\frac{w_0}{2}} = -mg, \tag{4.13}$$

and aligning the beam to have its flex point on the atoms will compensate locally for the effect of gravity, making the expansion isotropic. The effect of the optical compensation of gravity is shown in the right part of figure 4.7, in the case of well-aligned and not well-aligned beam.

Accelerated expansion

To reduce the effect of the mean field, expansion has to occur in a fast way so that the overlap between the outcoupled and trapped distributions is minimised in time. In light of this observation the outcoupled state $|2,-2\rangle$ has a further advantage in addition to the ones mentioned above: this state, being a high-field-seeking one, is antitrapped by the magnetic field gradient of the trap. This means that expansion is accelerated with respect to the case of the non-magnetic state $|2,0\rangle$, and accelerated more than the state $|2,-1\rangle$ because of its double magnetic moment.

SNR preservation: atom RF recapture

The use of the auxiliary state $|2,-2\rangle$ has then many advantages. Nevertheless, its fast expansion properties introduces a limit in the detection of the outcoupled sample: density vanishes so fast that the signal-to-noise ratio of the detected optical density can become remarkably low during the time-of-flight expansion needed to make

vortices large enough to be resolved. To avoid this problem expansion of the outcoupled atoms must be slowed down after the first fast expansion for overcoming mean-field interaction. A suitable way to implement that is the use of RF shielding (see section 4.1.3). Imposing a constant radiofrequency field the atomic levels become *dressed states* (Zobay et al. 2001). They are modified as depicted in figure 4.8. The choice of the value for the RF shield must avoid interference with the trapped sample, thus its value has to fix a resonant surface sufficiently far from the trapped BEC, also in order to make possible anharmonicities to vanish in the center of the trap. The dressing of the atomic states makes the potential to change its nature from antitrapping to trapping when the value r_{inv} is passed. After a first fast expansion stage, the outcoupled part passes the resonance surface with the RF shield and it experiences a confining potential, which refocuses atoms toward the center. Such a scheme will be identified as *RF recapture*. The recapture slows down the expansion and, refocusing the sample, it makes the SNR to increase again. Such a technique permits thus to perform a sufficiently long expansion to improve the detection of defects. The action of the recapture field happens mainly along the radial directions. Because of the weakness of the axial confinement the expansion along this direction is rather slow, in particular within the experimental expansion time atoms never reach the resonance surface along this axis. Hence the vortex axial dynamics is completely unaffected by the recapture field, and what is imaged along the horizontal radial direction is a faithful copy of condensate where the position of the vortex is coded in a reliable way.

PULSE-INDUCED COLLECTIVE OSCILLATIONS The outcoupling of a fraction of atoms induces in the remaining condensate an abrupt change in the density and hence in the chemical potential. The in-trap distribution rearranges to an equilibrium configuration but oscillatory modes are also activated. The most effective is the axial breathing mode, which occurs with a frequency of $\omega_{\mathrm{bAx}} = \sqrt{\frac{5}{2}}\omega_x$. This behaviour can strongly affect the accuracy in the vortex position tracking and in the calculation of its period, as will be evident in section 5.2.1.1. The extraction protocol has to be carefully designed in order to minimise the excitation of collective modes. We chose a proper timing sequence, in which the extraction-pulse sequence is phase-locked to the residual axial breathing oscillation. The extraction then is reduced to the smallest amount of atoms, compatibly with the requirement on the SNR on the imaging, in order to reduce the amplitude of the residual many-body excitations. The equilibrium size of the condensate is the Thomas-Fermi radius, which is proportional to the square root of the chemical potential $\mu \propto N^{2/5}$. The extraction of ΔN atoms from the condensate makes the chemical potential, and

hence the TF radius, to change. The fluctuation of the TF radius is then related to the amount of the extraction as:

$$\frac{\Delta\mathscr{R}}{\mathscr{R}_0} \propto \frac{1}{5}\frac{\Delta N}{N_0}. \tag{4.14}$$

Sampling locking to the breathing mode

The time at which the extraction is performed can be tuned to minimize the oscillation amplitude. Each extraction introduces a jump in the equilibrium Thomas-Fermi radius and triggers an oscillation whose amplitude is $\Delta\mathscr{R}_x/2$, where $\Delta\mathscr{R}_x$ is the difference between the initial and final equilibrium TF radii. If the extraction timing is chosen to be equally spaced and occurring always in phase with the axial breathing mode, like in figure 4.9a, the oscillation is damped after the second extraction, but it is reactivated in the following cycle. Such a timing is therefore not effective to reduce the amplitude of the overall oscillation, and also the TF radius in the instant of the extraction changes in different steps, depending on the parity of the number of extractions performed. In order to remove such a "bistability" in the decrease of the Thomas-Fermi radius the second extraction has to be done when the oscillation induced by the first pulse reaches the half of the amplitude during the expansion phase before passing to the equilibrium value, as schematically represented in figure 4.9b. The following pulses then can be taken every half (or three halves) of the oscillation period. In such a way the TF radius scales univocally and the breathing oscillations are still present, but minimized in amplitude. Given the experimentally measured period $T_{\mathrm{bAx}} = 56(2)\,\mathrm{ms}$, two different time sequences can then be implemented:

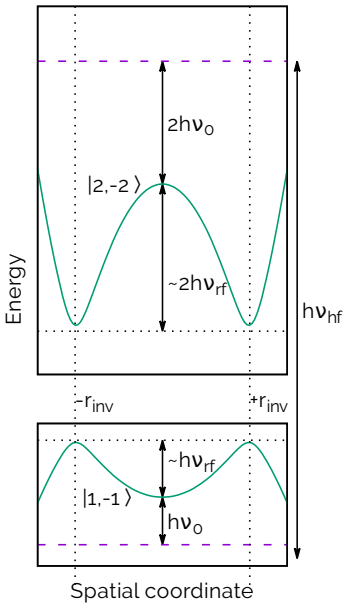

Figure 4.8: Effects of RF dressing on the trapped and anti-trapped states.

- *dense sampling*: second extraction after $\frac{7}{12}T_{\mathrm{bAx}} = 33\,\mathrm{ms}$, followed by subsequent pulses every $\frac{1}{2}T_{\mathrm{bAx}} = 28\,\mathrm{ms}$;
- *long sampling*: second extraction after $\frac{19}{12}T_{\mathrm{bAx}} = 89\,\mathrm{ms}$, followed by subsequent pulses every $\frac{3}{2}T_{\mathrm{bAx}} = 84\,\mathrm{ms}$.

The two time sequences were used for studying, respectively, systems with many vortices, focusing on their interaction, and the dynamics of single vortices on a time scale comparable to the vortex orbiting period.

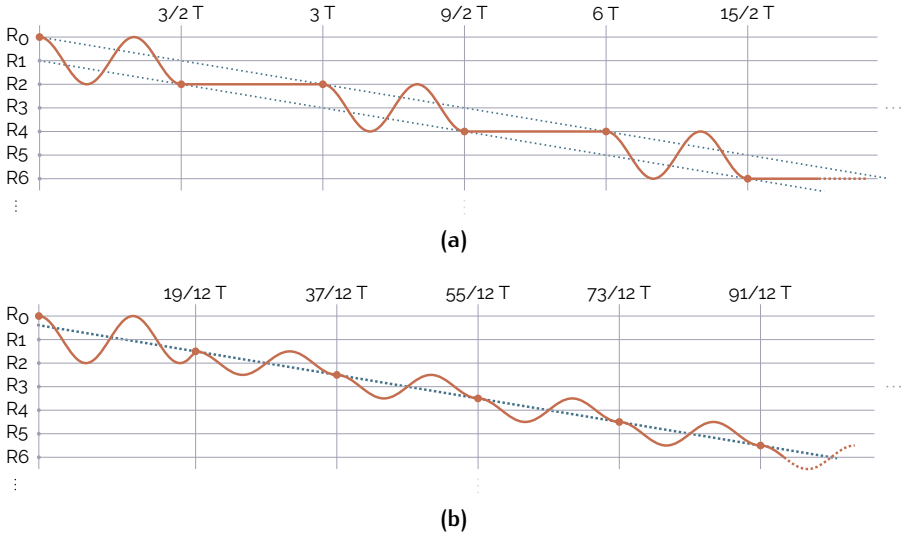

Figure 4.9: Schematic representation of the pulse-induced oscillation in the case **(a)** of equally spaced extraction, and **(b)** optimized extraction timing sequence.

EXPERIMENTAL TIME SEQUENCE The experiments are performed in the tight regime I_t. The optical potential is switched on just after the loading of the magnetic trap and the evaporation ramp is tuned optimizing condensation in the trap compensated for the gravity. At the end of the evaporation ramp the radiofrequency shield is turned on 100 kHz above the trap bottom. This field implements also the recapture of the outcoupled part. The condensates, initially, have on average 1×10^7 atoms. Always the same fraction of the initial number of atoms is extracted, $\Delta N/N_0 \approx 4\%$. The maximum number of extraction is then $N_0/\Delta N \simeq 25$, thus we perform a total of 20 extractions, avoiding the complete depletion of the condensate and keeping a residual population of $N_{20} = N_0 - 20\Delta N \approx 2 \times 10^6$ atoms. The last pulse extracts about 20% of the actual atom number. The total time span is then $\sim$ 560 ms for the dense sampling and $\sim$ 1700 ms for the long sampling sequence. In order to keep constant the number of extracted atoms the duration of the μw pulse has to be increased. The first pulse lasts 3 µs, given the Rabi frequency of $\sim$ 10 kHz. For small pulse duration the Rabi oscillation can be approximated as quadratic with respect to the pulse duration, hence the two conditions

$$(\tau_0\Omega)^2 \simeq 0.04 \tag{4.15}$$

$$(\tau_{20}\Omega)^2 \simeq 0.2 \tag{4.16}$$

lead to a relation between the first and last pulse of $\tau_{20} \simeq \sqrt{5}\tau_0 \simeq 6.7\,\mu s$. The duration of the pulses is then fine-tuned experimentally up to a value of 7 µs. The spectral broadening of the rectangular pulse is between 150 kHz and 60 kHz, lowering with the increasing of the pulse duration, covering in all cases the whole condensate, whose

chemical potential also gets reduced in time because of the extractions. Experiments were done to look at the dynamics of a single vortex and to possible interaction mechanisms between more vortices. In the first case the long sampling protocol was used, with a KZ ramp of $525\,\mathrm{kHz\,s^{-1}}$. In the other case, the dense sampling protocol was implemented to observe in average more defects through a faster KZ ramp ($700\,\mathrm{kHz\,s^{-1}}$). The total expansion time of the outcoupled part is 13 ms.

A few examples of the images obtained via the μw-PMD technique after the digital processing are reported in figure 4.10, in its right part the same experimental images are shown after squeezing the images along the transverse axis of the condensate for enhancing the vortex visibility.

LIMITS OF THE STROBOSCOPIC TECHNIQUE While this technique is well suited for studying the dynamics of a single vortex, it has some limitations that can make difficult the investigations when considering systems with many vortices. In particular:

- the strong interaction between outcoupled atoms and the mean field of the remaining BEC requires accelerated expansion in the anti-trapped state and gravity compensation through optical levitation to guarantee isotropic expansion;
- the excitation of breathing modes can become critical thus a careful design of the experiment timing is required to reduce it, ultimately limiting the acquisition rate;
- very fast expansion in the anti-trapped state must be reduced in the last part of the expansion through a recapture RF field, in order to preserve a sufficiently high signal-to-noise ratio;
- information about the dynamics in the radial plane, which is central in the studying of vortex-vortex interactions, is completely lost.

4.2.3 Radiofrequency Sweep Minimally Destructive Imaging

In the present section I will describe the developement of a new experimental technique, designed to implement a time-dense minimally-destructive real-time imaging to study dynamics of vortices when approaching, overcoming limitations of the μw-PMD technique. In the first part I will describe the principles of operation of this technique, then I will point out one of its features: the mapping of the axial orientation of vortex lines onto the radially-integrated column density. I will report some numerical simulations supporting this feature. I will refer to this novel technique as *Radiofrequency Sweep Minimally Destructive* (rf-SMD) imaging technique.

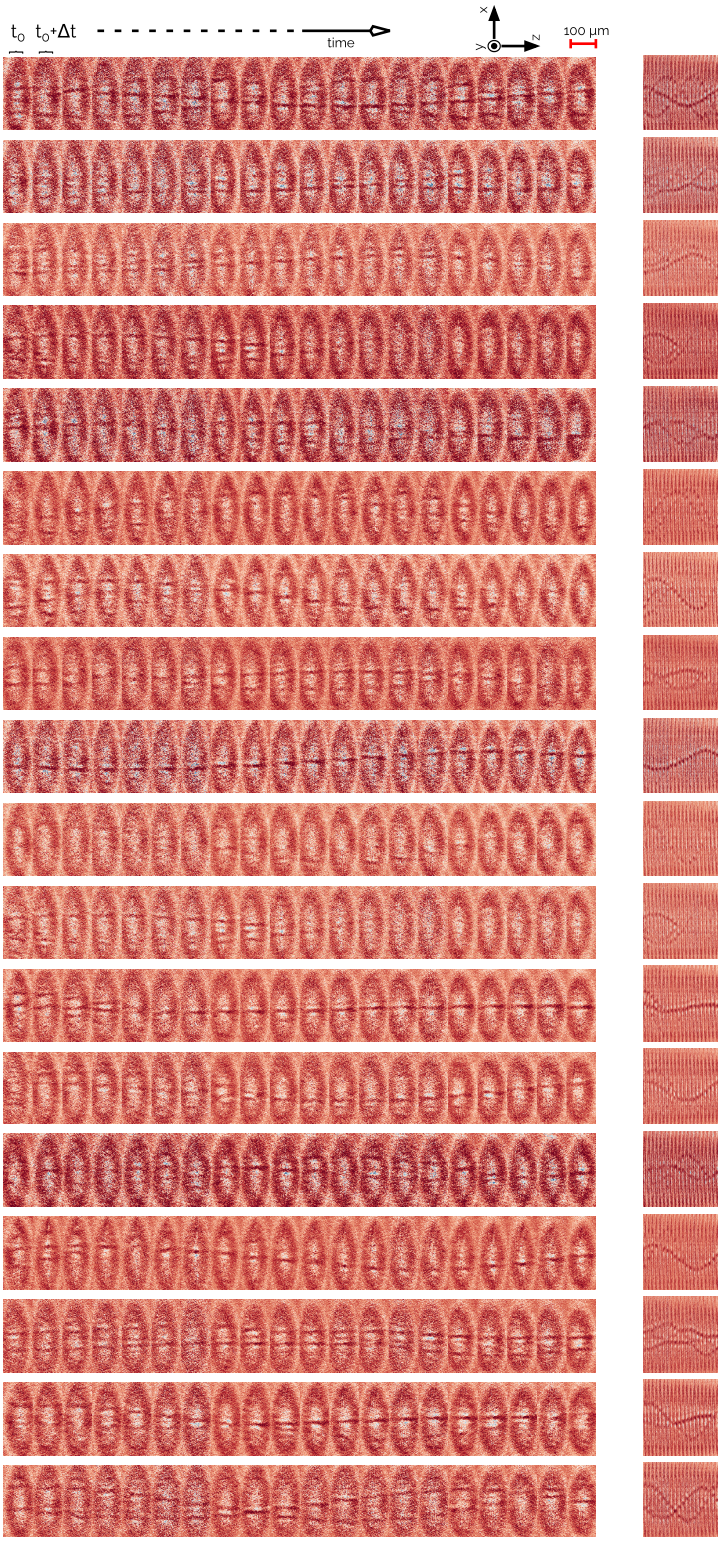

Figure 4.10: Examples of acquisitions through μw-PMD technique.

The Atom Laser

To overcome the aforementioned limitations of μw-PMD imaging technique, an atom-laser-like outcoupling is implemented (Bloch et al. 1999). Outcoupling is performed between states in the same hyperfine manifold, using an electromagnetic field in the RF band. Such a technique clearly needs a repumping of the extracted atoms in a bright state to access information; details on that will be given in the following sections. The process of outcoupling can be implemented more efficiently than the previous case, reducing the excitation of collective modes to a negligible level. No constraints on the pulse timing sequence are present, permitting a very high frame rate (infinite in the case of continuous outcoupling).

Resonances between the magnetic internal states, whose degeneration is removed by the trapping potential, are strongly affected by the presence of gravity, as discussed in section 3.3. This fact permits to implement a local coupling between the internal states. For the sake of convenience in this work I will refer to *outcoupling* for transitions remaining in the same F-manifold ($\Delta F = 0$), while I will call *repumping* transitions when the F-manifold changes ($\Delta F = +1$). This nomenclature is chosen because in the present technique the outcoupling from the BEC exploits the spin-flip transition $|1,-1\rangle \rightarrow |1,0\rangle$, while the transition $|1,0\rangle \rightarrow |2,0\rangle$ brings the atoms into a bright state with respect to the optical transition $F = 2 \rightarrow F' = 3$, as required for imaging.

Outcoupling

I will first consider the case of outcoupling: $\Delta F = 0$ and $\Delta m_F = +1$. For convenience I will use the notation $h\nu_{\Delta F=0}^{\Delta m_F=+1} \equiv h\nu_{\mathrm{rf}}$. Neglecting the effect of gravity the TF distribution of the sample would be centered in the minimum of the magnetic field, $\vec{r} = \{0,0,0\}$, and the resonance condition in that point would be simply determined by the bias magnetic field:

$$\begin{aligned} h\nu_{\mathrm{rf}}(\vec{0}) &= \left| U_{|1,0\rangle}(\vec{0}) - U_{|1,-1\rangle}(\vec{0}) \right| \\ &= |0 - \mu_{\mathrm{at}} B_0| \\ &= \mu_{\mathrm{at}} B_0, \end{aligned} \tag{4.17}$$

being $|\vec{\mu}_{\mathrm{at}}| = 0$ for the state $|1,0\rangle$. A frequency larger than the one given by equation (4.17) identifies a resonance surface that is an ellipsoid centered in the origin. If the blue detuning from condition (4.17) is less than the chemical potential of the sample, outcoupling occurs from an elliptic shell concentric with the BEC, whose distance from the center depends on the detuning and its thickness depends on the spectral purity of the RF pulse.

When gravity is taken into account, instead, the TF profile of the BEC is off-centered with respect to the magnetic field, being the minimum of the potential energy located at $\vec{r}_{\mathrm{min}} = \{0,0,z_{\mathrm{sag}}\}$ (see section 3.3). The sample, then, experiences a Zeeman shift that is not symmetric around its own center because it is positioned below the

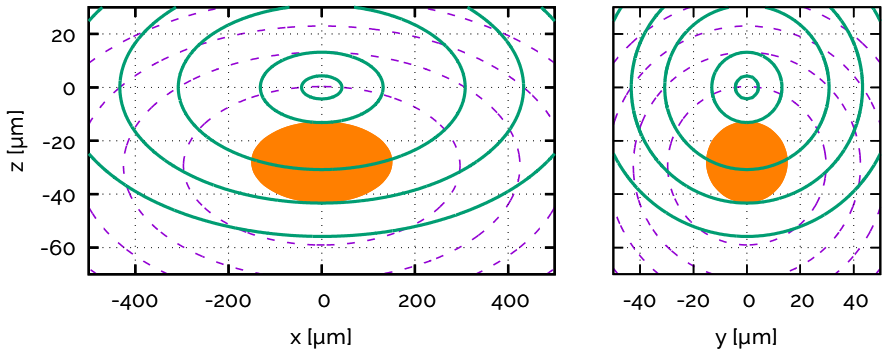

Figure 4.11: Contour plot of the magnetic field and position of the sample. The resonance shell and its intersection with the sample is shown.

center of the magnetic field. The resonance surface is defined by the Zeeman shift, thus it clearly remains centered with the magnetic field. Now the intersection between the sample and the resonance surface occurs only in a partial region of the BEC. Figure 4.11 reports the position of the condensate (orange ellipse), the equipotential lines of the trapping potential (purple dotted lines) and the resonance surfaces for different values of the RF field (green continuous lines), the radial and axial views are depicted.

Repumping

Repumping to $F = 2$ manifold is required to image the extracted slices of atoms. Imaging resonant with $F = 2 \rightarrow F' = 3$ transition, since it is largely out of resonance with $F = 1$ manifold, is not destructive for the BEC. The transition now addressed is the $|1,0\rangle \rightarrow |2,0\rangle$: $h\nu_{\Delta F=+1}^{\Delta m_F=0} \equiv h\nu_{\mu w}$. Such a transition has to be driven in a region far away from the condensate in trap, in order to avoid a direct μw outcoupling. The presence of the trapping magnetic field is crucial and exploited in a similar way than for the RF outcoupling: when atoms in the $m_F = 0$ state fall in the gravity field they experience a strongly increasing magnetic field, being the vertical aligned to the strong confinement (large gradient) axis of the trap. States to be connected are non magnetic to first order ($m_F = 0$), but in presence of a strong field they experience a second order Zeeman shift. This shift increases the spacing between the two levels by an amount given by

$$\Delta\nu_{\text{clk}} = \frac{(g_J - g_I)^2 \mu_B^2}{2h\Delta E_{\text{hfs}}} B^2. \tag{4.18}$$

By setting up a μ-wave field with an appropriate blue detuning from the zero-field hyperfine splitting a resonant surface centered with the magnetic field is settled. Such a surface intersects the falling atoms coming from outcoupling at a distance fixed by the detuning. If the detuning is chosen sufficiently large, the resonant surface does not intersect the BEC. Figure 4.12 reports a schematic view of the whole process.

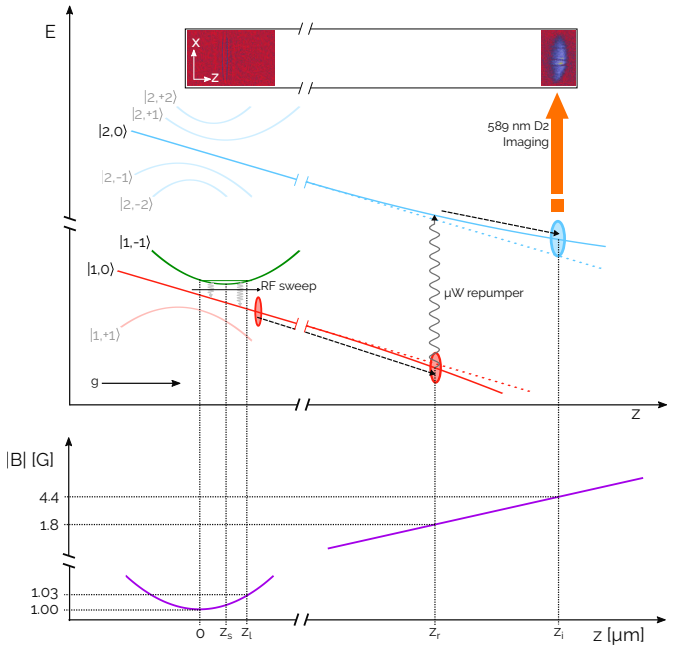

Figure 4.12: Schematic picture of the rf-SMD technique. In the upper part energy levels are reported as a function of the vertical coordinate, while in the lower part the modulus of the trapping field is reported. z_s is the gravitational sag, $z_l = z_s + \mathscr{R}_\perp$ corresponds to the lowest boundary of the condensate, z_r is the position of the repumping surface and z_i is the imaging position.

4.2.3.1 *Frequency-sweep Outcoupling*

I will now discuss different ways in which outcoupling can be implemented. What we are doing here can be considered a *continuous* or a *pulsed* atom laser. I will then focus on a particular kind of pulsed outcoupling, that is the point of major novelty in our technique: the *frequency-sweep outcoupling*. I will describe its peculiarities, reporting also some supporting numerical simulations.

Continuous vs Pulsed Outcoupling

In analogy to optical lasers also atom lasers can be divided in continuous and pulsed lasers. A continuous atom laser can be generated radiating the sample with a continuous single RF field. The sample acts as a coherent source of particles. If the resonance condition between the trapped state and the untrapped one is met somewhere in this particles reservoir, a coherent atomic beam is expelled from it, propagating along the vertical direction under the effect of gravity. In the top figure 4.13 an example of continuous extraction is reported. A depleted stripe crossing the atomic beam along its propagation direction is visible in the filtered zoom of figure 4.13, this is related to the presence of a vortex in the probed BEC. The main drawback of the continuous outcoupling is its not so small destructivity: to have a good signal-to-noise ratio a rather large extraction is needed, depleting totally the condensate in about 100 ms. Such effect drastically reduces the time interval during which the vortex dynamics can be

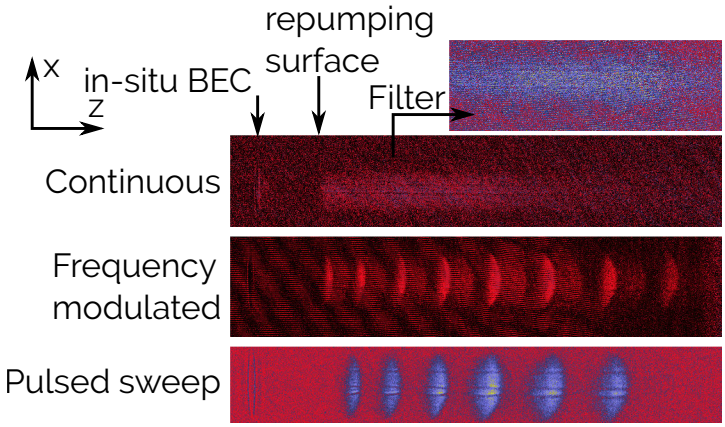

Figure 4.13: Example of continuous (top) atom laser, frequency modulated outcoupling (middle) and frequency-sweep outcoupling (bottom).

followed. The signal-to-noise ratio is limited also because the atomic beam crosses a region where the magnetic field is strongly changing. Thus a spatial modulation of the absorption cross-section of the transition used for imaging occurs. Such a modulation does not permit to image the entire beam with the same efficiency along its entire path.

A way to increase the signal-to-noise ratio is to discretize the outcoupled beam, accumulating the signal in time-separated bunches. This can be obtained as in Bloch et al. 2000, where extraction is performed from two spatially separated surfaces. The coherence of the two sources makes the two beams interfere, like in the Young's double slit experiment. Whenever the interference is constructive the signal is increased while the noise remains the same, improving in this way the visibility of the vortex signal. To achieve that we applied a frequency modulation ν_m to the carrier ν_C which outcouples from the center of the condensate. The frequency deviation $\Delta\nu$ of the modulation fixes the number of discrete spectral components of the signal, hence the number of coherent sources from the condensate is $\Delta\nu/\nu_m$. An example of experimental realization of such a scheme is reported in figure 4.13, where 5 point-like sources were activated. The improvement in the SNR with respect to the continuous outcoupling is evident. Different choices of the modulation parameters lead to different periods in the interference pattern. A long observable time interval is not achievable, even with this kind of outcoupling because the extraction is still continuous even if information comes from bunches with larger SNR.

To minimize the impact of the imaging on the remaining sample, we decided to realize a pulsed laser outcoupling. A simple way to implement such an outcoupling consists in using RF pulses, whose time separation defines the time resolution of the imaging, while their duration defines their spectral broadening. The latter must be larger than the width of the condensate, *i.e.*, its chemical potential expressed in frequency units. In this way a good SNR can be achieved while

completely avoiding extraction when not needed, increasing in this way the time span that can be probed.

We choose another way to implement pulsed outcoupling: instead of single pulses we apply a linearly chirped RF signal starting just below the minimum resonance and ending just above the extension of the sample, this frequency sweep lasts a few ms and it is repeated many times, each corresponding to an extraction. The RF signal is kept at a very low intensity to reduce the Rabi frequency and hence keeping instantaneously small the range of the coupling between the levels, in this way the resonance condition is met on a slice of vanishing thickness of the condensate. The advantages of this approach will be evident below.

The experimental optical density 2D profiles of the outcoupled samples, obtained through absorption imaging, are digitally filtered and then integrated along the vertical direction. The obtained 1D profiles are then fitted with a fourth-order polynomial and residuals are calculated[4]. Such a procedure is performed on each extraction to reconstruct the full temporal sequence for a given condensate. A pictorial sketch of the entire procedure is reported in figure 4.14. The presence of an asymmetry in the residuals turned out to be a major strength of the rf-SMD imaging technique, as described in the following paragraphs.

Self-interfering Velocity Field

The sweep of the outcoupling field from a lower to a higher frequency causes the release of atoms from the top of the condensate first and then from lower slices. Such a procedure produces a bunch of outcoupled atoms with a high optical density and hence a good SNR. The superposition of the coherent slices of atoms leads to an interference of different parts of the outcoupled wavefunction. The presence of a vortex modifies the local velocity field, and the phases of the extracted parts are not equal. The superposition of parts with different phases due to the presence of a velocity field gives rise to interferences in the density profile of the outcoupled cloud. The shape of the interference pattern is related to the direction of the velocity field with respect to the extraction front:

- *vortex velocity field copropagating to the extraction front velocity*: constructive interference leading to a higher density (panel t_1 of figure 4.14);
- *vortex velocity field counterpropagating to the extraction front velocity*: destructive interference leading to a low density (panel t_3 of figure 4.14);
- *vortex velocity field perpendicular to the extraction front velocity*: unaffected density profile (panel t_2 of figure 4.14).

4 The outcoupled atoms are not well described by a TF profile, thus a generic polynomial model was preferred.

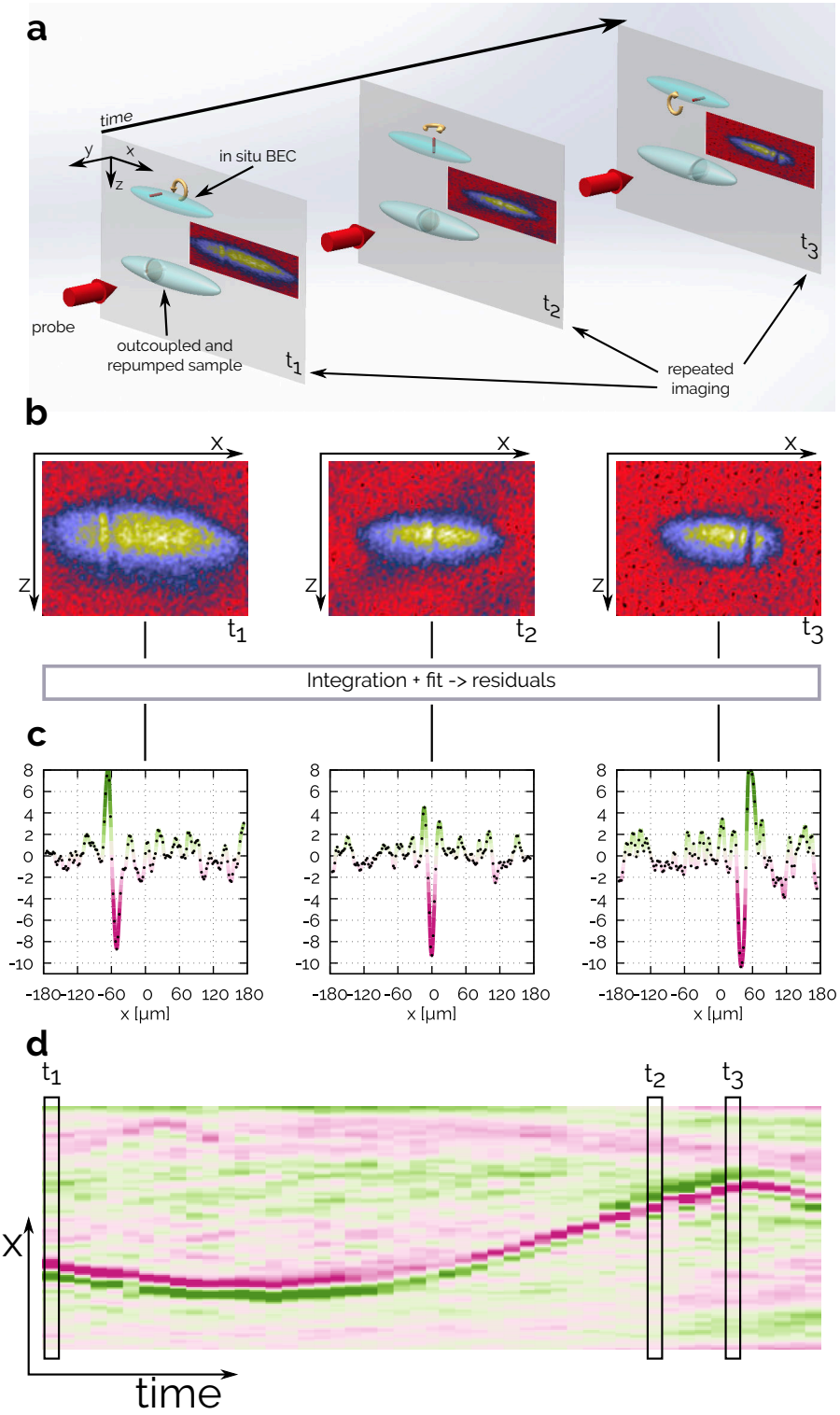

Figure 4.14: **(a)** The imaging of the outcoupled atoms is repeated in time. **(b)** The obtained optical density profiles are then digitally filtered and processed, obtaining for each extraction, after integration of the fit residuals, a 1D axial profile. **(c)** Each profile encodes information about the position and orientation of the vortex. **(d)** All the 1D profiles are put together in chronological order to highlight the dynamics of the vortex and the changing in the interference pattern encoding the vortex orientation.

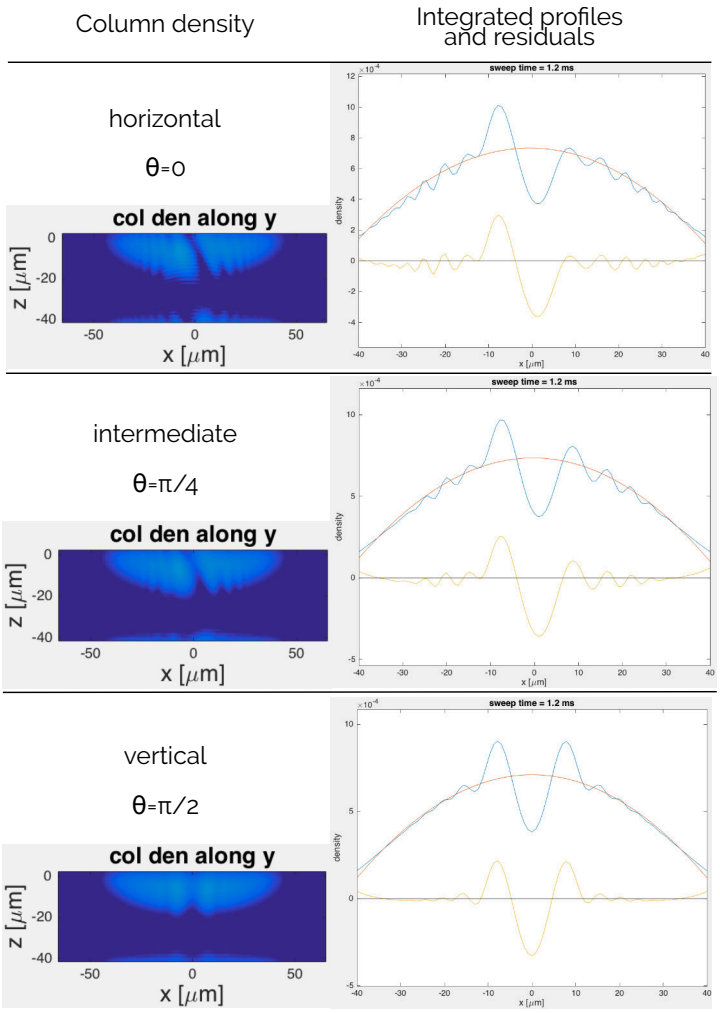

Figure 4.15: Simulations of the frequency-sweep outcoupling in cases of different vortex orientations. The column density along the imaging direction y is plotted on the left, while in the right part the vertically integrated optical density is reported.

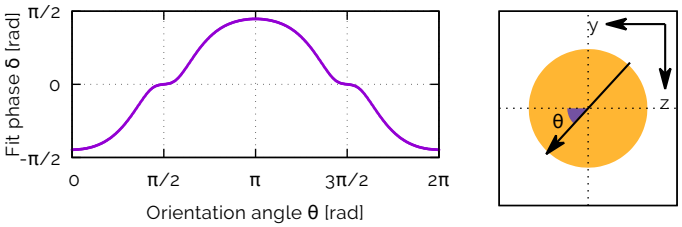

Figure 4.16: The function $\delta(\theta)$, as numerically determined. In the right part the orientation angle is defined.

Numerical simulations

These behaviours are confirmed by the numerical simulation of the outcoupling and expansion. The condensate is simulated through a real-time Gross-Pitaevskii equation. Since the oucoupling lasts only a few ms, the vortex dynamics in the trap is frozen during the simulation. The expansion of the falling cloud enhances the x-direction asymmetry of the density profile in the presence of a vortex due to the inhomogeneous velocity field around it. This behaviour is a characteristic of transverse vortices in cigar-shaped Bose-Einstein condensates, as will be widely discussed in the next chapters of the thesis. Numerical simulations confirmed the self-interference effect, as reported in figure 4.15 for different orientations of the vortex in the yz axial plane.

Mapping the Axial Orientation

The results of the simulations allow us to extract information about the radial orientation of a vortex from a radially integrated sample. As for the experimental images, the numerical data were fitted with a fourth-order polynomial and residuals were calculated. The residual can be fitted with a phenomenological relation valid in the case of solitons:

$$f_{\text{fit}} = -A\frac{\cos\left[q(x-x_0)+\delta\right]}{\cosh^2\left[\frac{x-x_0}{\Xi}\right]}. \tag{4.19}$$

The fit parameter δ in equation (4.19) describes the symmetry of the function f_{fit}, thus it is related to the angle θ of the vortex line in the plane yz. The relation $\delta(\theta)$ can be numerically calculated and is reported in figure 4.16. In the same figure the orientation angle of a vortex is defined. Details on the experimental determination of such a relation and its comparison with the theoretical one are postponed to section 5.2.2.1.

EXPERIMENTAL TIME SEQUENCE The BEC transition is crossed in the tight trap regime I_t, but after the end of the evaporation ramp the trap is adiabatically decompressed to the I_s regime, together to the adiabatic tuning of the trap bottom (see 4.1.3). At the end of the decompression a large condensate (2×10^7 atoms) is present. The thermal fraction is negligible ($T < 150\,\text{nK}$, $T_c \simeq 500\,\text{nK}$). Such a decompression is necessary to reduce the magnetic field experienced by the outcoupled atoms during the fall. In fact imaging can become criti-

cal in our case, given that the polarization of the probe beam cannot be optimally set. Outcoupling starts about 250 ms after the transition. The choice of the outcoupling ramping rate was done maximizing the visibility of the defect in the outcoupling and the optimal value was found to be 10 kHz ms^{-1}. The range of the frequency ramp is chosen to cover the entire condensate, *i.e.*, the whole dip of figure 4.3. The chosen span is $\sim$ 40 kHz. Referring to figure 4.12 the gravitational sag is $z_s \approx 28\,\mu$m, while the lower edge of the condensate is at $z_l = z_s + \mathscr{R}_\perp \approx 45\,\mu$m. The microwave repumping surface is set at the position $z_r \approx 280\,\mu$m, corresponding to a detuning $\Delta\nu_{clk} \approx 15$ kHz, equation (4.18). The total time of flight is 13 ms, after which the absorption profile of the oucoupled cloud is taken, $\approx 800\,\mu$m below the condensate. The local strength of the magnetic field is reported in the lower part of figure 4.12. The whole sequence is repeated every 12 ms. In order to achieve such a high frame rate two interlaced cameras (see 4.2) have to be used interlaced.

Part III

EXPERIMENTAL RESULTS

In the third part of this thesis I will present the results of the experiments about the structure, the dynamics and the interactions of vortices in an elongated Bose-Einstein condensate.

5 SINGLE VORTEX STATIC AND DYNAMIC PROPERTIES

CONTENTS

In the current chapter I will introduce the concept of *solitonic vortex*, which is the lowest excited state of a cigar-shaped condensate, making it the natural way in which vorticity appears in such a system. In the first part I will describe the peculiarities of the solitonic vortex in terms of the phase pattern of the wavefunction and its effects on the density profile, both in-situ and after a time of flight. The expansion properties are the subject of experiments described here.

In the second part of the chapter I will characterize experimentally the motion of the solitonic vortex, in the two opposite cases:

- a vortex with a fixed orientation but precessing around the center on an elliptic orbit;
- a vortex at the center of the BEC but whose axis rotates around the axial direction (*spinning vortex*).

The characterization of the precession was done through the μw-PMD technique described in section 4.2.2 of the previous chapter. The investigations of the spinning vortex instead was made possible thanks to the novel rf-SMD technique, introduced in section 4.2.3.

A BIT OF HISTORY The first results of the characterization of the Kibble-Zurek mechanism in our system was done in Lamporesi, Donadello, Serafini, Dalfovo, et al. 2013 from which figure 5.1 is extracted. The defects created in the temperature quench across the BEC transition were thought to be gray solitons, because of the prediction by Zurek 2009 for an elongated system. This assumption was also supported by the fact that the defects show essentially a planar structure after the time of flight, when imaging is performed along two orthogonal radial directions. The bent structure sometimes occurring, as in figure 5.1 **(g)**, was interpreted as a sign of the snake instability characterizing the decay of solitons in systems with more than one dimension. The most puzzling point in the interpetation of such defects

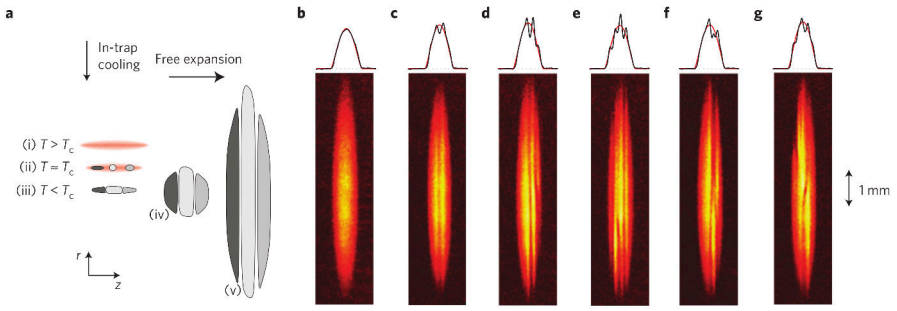

Figure 5.1: KZM generated defects after expansion, from Lamporesi, Donadello, Serafini, Dalfovo, et al. 2013.

as solitons was their long lifetime, of the order of a second, while the expected time scale for the snake instability would be much shorter ($\sim$ 10 ms for our trap), being the decay rate of a soliton of the order of the transverse trapping frequency $\tau^{-1} = \omega_\perp$. A similar effect was observed also in a cigar-shaped Fermi gas after phase-imprinting of a soliton (Yefsah et al. 2013). Further investigations on the nature of these defects became thus necessary.

The solitonic vortex

A cigar-shaped sample sits in a sort of cross-over between 1D and 3D systems, thus, in order to have a better understanding of the observations, a major point that must be addressed regards the nature of the excitations supported by such systems. This argument was theoretically treated in the works by Brand et al. 2002; Komineas et al. 2003; N. Parker 2004. They show the presence of a vortex state, called *solitonic vortex*, which is the first excited state of an elongated system. The vortex core in the case of solitonic vortex is orthogonal to the trap axis, then the vortex experiences a potential which is non-axisymmetric with respect to its own axis. Such a defect transforms smoothly into a soliton for a very strong radial confinement (*i.e.*, toward the 1D regime) and, in the opposite limit, into a "traditional" vortex in a 3D spherical system. The name solitonic vortex is due to the fact that the defect is a topological state with quantized circulation, as a vortex, but characterized also by a concentration of the superfluid flow in the radial plane containing the vortex core. Its peculiarities are related to the non-axisymmetric confinement experienced by the vortex in elongated systems. Thus our research focused on the characterization of the density and phase properties of the defects observed in Lamporesi, Donadello, Serafini, Dalfovo, et al. 2013, revealing that they actually are vortices in a weakly non-axisymmetric regime, whose solitonic-vortex properties can be highlighted through our experimental techniques (Donadello, Serafini, Tylutki, et al. 2014). The dynamical properties of these defects were then characterized in Serafini et al. 2015, opening the way for further intriguing studies in the field of vortex-vortex interactions. The cigar-shaped system shows in fact big advantages for studying such kind of effects, as will be extensively described in chapter 6.

Table 5.1: Conversions between dimensional parameters used in different wors. In Brand et al. 2002 the boundaries are hard walls where L_t is the transverse dimension, conversion is done through the approxiamtion $L_t \approx 2\mathscr{R}_\perp$. In Komineas et al. 2003 systems that are not axially confined are considered, they report a generalization of their results to finite axial confinement in the appendix of their work.

Reference	used parameter	conversion to γ
N. Parker 2004	$\gamma_{\text{Parker}} = \frac{\mathscr{R}_x}{\mathscr{R}_\perp}$ with $\mathscr{R}_x = 20\xi$	$\gamma = \frac{10}{\gamma_{\text{Parker}}}$
Brand et al. 2002	L_t/ξ	$\gamma = \frac{L_t/\xi}{4}$
Komineas et al. 2003	$\gamma_{1D} = n_{1D}a$	$\gamma = \gamma_{1D}$
Muñoz Mateo et al. 2014	$\gamma = \frac{\mu}{\hbar\omega_\perp}$	$\gamma = \gamma$

5.1 DEFECTS IN ELONGATED SYSTEMS

An elongated system is obtained when the confinement frequencies obey the hierarchy $\omega_y = \omega_z \equiv \omega_\perp \gg \omega_x$; the ratio $AR = \frac{\omega_\perp}{\omega_x}$ is known as *aspect ratio* and characterizes how much is the difference in the confinements and hence in the sample sizes, being $\omega_\perp/\omega_x = \mathscr{R}_x/\mathscr{R}_\perp$. However, the relevant dimensionless parameter for characterizing the behaviour of defects supported by an elongated system is the ratio between the chemical potential μ and the transverse confinement $\hbar\omega_\perp$ (Carr et al. 2007):

$$\gamma = \frac{\mu}{\hbar\omega_\perp} = \frac{\mathscr{R}_\perp}{2\xi}. \tag{5.1}$$

In equation (5.1) γ was rewritten in terms of the ratio between the transverse size and the healing length. The parameter γ is then a signature of how much the radial confinement is effective on the vortex structure, whose relevant length scale is the healing length ξ. γ plays thus the role of a *dimensionality parameter* which maps the crossover between 1D and 3D systems. For comparison with other relevant works about this dimensional crossover I report in table 5.1 the conversions between the factor used in those works and the γ factor defined by equation (5.1).

Elongated systems as waveguides

A cylindrical system can be seen as an electromagnetic non-linear waveguide, where the condensate plays the role of the medium, while solitary waves can propagate across it along the symmetry axis (Carr et al. 2007). When $\gamma \ll 1$ the system is 1D, being the size of the channel of the order of the extension of the wave (healing length), leading to a single-mode waveguide where the unique admitted solitary wave is the dark or gray soliton. When γ increases, the condensate enters the Thomas-Fermi regime. The waveguide is no longer single-mode and a family of solitary waves appear. They resemble the vibrational mode of a membrane fixed on a circular contour, the *Chladni modes*, where the nodes of the vibration mode are nodes of the BEC

wavefunction, *i.e.*, vortical lines. A numerical characterization of such modes can be found in Muñoz Mateo et al. 2014. Among the solitary waves one may find the soliton, which has no topological charge, the vortex ring and the solitonic vortex. This last kind of excitation is a non-axisymmetric excitation which is the lowest energy excitation in elongated samples outside the 1D regime. Numerical calculations of the excitation energies of solitary waves in cylindrical systems show a series of bifurcation points occurring at different γ going from the 1D regime, where the soliton is the unique possible excitation, to a full 3D system, where more and more modes are accessible. The lowest energy excitation outside the 1D regime ($\gamma \gtrsim 1.5$) is always identified with the solitonic vortex. This structure smoothly connects to the vortex solution of pancake-shaped systems (i.e. toward the 2D regime) or 3D spherical systems. It is easy to recognize that in a cigar-shaped system the transverse vortex minimizes the energy, as introduced in sections 1.2.2.2 and 2.1. The transverse dimensions in an elongated system are the shortest, then vortices tend to align along such directions to minimize their energy.

Solitonic vortices and KZM

What is observed in Lamporesi, Donadello, Serafini, Dalfovo, et al. 2013 are then solitonic vortices, whose formation can be ascribed to the decay from Kibble-Zurek generated solitons through a cascade of Chladni solitons, as observed in Ku, Mukherjee, et al. 2016, or can be directly generated via the Kibble-Zurek mechanism. Our system is difficult to access in the first instants after the BEC transition, hence a clear experimental picture of what happens just after the setting of the condensed phase is not yet achievable. A refined study of the scaling of the number of defects was done in Donadello, Serafini, Bienaimé, et al. 2016, and numerical simulations were performed by N. Proukakis 2016.

5.1.1 In-situ Properties of the Solitonic Vortex

As anticipated the solitonic vortex in elongated BECs and the usual vortex in pancake systems are, in fact, the manifestation of the same phenomenon in different systems, having both the same topology; for this reason I will use in the following the terms vortex, transverse vortex and solitonic vortex for referring to the same defect, *i.e.*, the lowest-energy defect in a non-axisymmetric landscape. What gives its peculiarities to the transverse vortex, is how the superfluid flow arranges around the vortex core because of the asymmetric effect of boundaries. In the following I will describe such peculiarities, starting from the phase profile of the transverse vortex and then explaining the effects of such a profile on the density around the vortex. Some features will be pointed out through experimental analysis of the defect.

The phase pattern

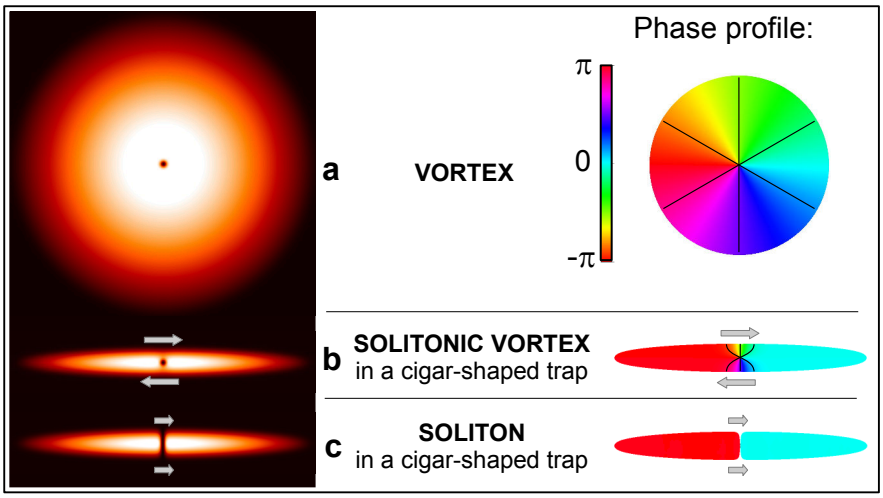

Figure 5.2: Phase and density pattern of a vortex in a pancake and in a cigar. The solitonic vortex peculiarities appear in elongated systems. For comparison the pattern of a soliton in a cigar is shown. From Donadello, Serafini, Tylutki, et al. 2014.

A vortex aligned along the symmetry axis of a cylindrical trap has a phase S that increases linearly from 0 to 2π along a circular path concentric with the vortex core. In the case of a transverse vortex instead the phase gradient is not uniform around the core because the boundary conditions impose the equi-phase surfaces to be orthogonal to the boundaries of the condensate[1]. In this way equi-phase surfaces bend and squeeze in a region close to the radial plane that contains the vortex line. In figure 5.2 the two behaviours are schematized together with the representation of a dark soliton.

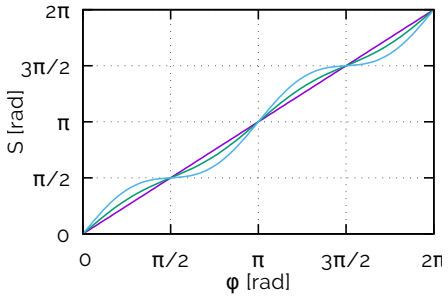

Figure 5.3: Phase winding around a bare vortex (purple) and a solitonic vortex along $r_\perp = 0.5\mathscr{R}_\perp$ (green) and along $r_\perp = 0.75\mathscr{R}_\perp$ (cyan), calculated from (5.2) with the experimental parameters.

The way in which the phase S changes around a vortex core in a non-axisymmetric landscape was derived by A. L. Fetter and A. A. Svidzinsky 2001. The phase S along a circular path at distance $r_\perp$ from the core is a function of the azimuthal angle φ, choosing the axis z of the cylindrical frame of reference aligned to the straight vortex core. Such a function is

$$S = \varphi - \frac{1}{4}\left(\frac{1}{\mathscr{R}_x^2} - \frac{1}{\mathscr{R}_\perp^2}\right) r_\perp^2 \log\left(\frac{r_\perp}{\tilde{\mathscr{R}}}\right) \sin(2\varphi), \tag{5.2}$$

1 The component of superfluid velocity orthogonal to the boundary must vanish on the border.

where $\tilde{\mathscr{R}}^2 = 2\mathscr{R}_x\mathscr{R}_\perp/(\mathscr{R}_x^2 + \mathscr{R}_\perp^2)$. When the asymmetry vanishes, $\mathscr{R}_x/\mathscr{R}_\perp \to 1$, the profile tends to the isotropic case $S = \varphi$. The vortex in this sense becomes a "dressed vortex", as pointed out by Anglin 2002, where the velocity field of the bare vortex is modified by the action of the boundaries. In figure 5.3 the phase winding around the vortex core is plotted for the axisymmetric (purple line) and for the non-axisymmetric case (green and cyan lines). In these last cases, the curves are calculated for our sample along the circle $r_\perp = 0.5\mathscr{R}_\perp$ and $r_\perp = 0.75\mathscr{R}_\perp$ respectively. The corrections to the vortex energy (equation (1.37)) when considering a phase winding like the one expressed by equation (5.2) does not modify the picture given at the end of chapter 1, in which the main contribution to the vortex energy is directly proportional to the length of the vortex core. Thus the argument of the minimization of the energy in a cigar-shaped trap through the transverse alignement of the vortex is still valid.

Some numerical simulations were done to characterize the properties of a vortex in the dimensional cross-over (Tylutki et al. 2015). The phase pattern of a vortex, whose core is aligned to a radial direction and passes through the center of the trap, is imprinted onto the ground state solution of the GPE. The system is let to converge to a stationary vortex state through imaginary time evolution of the time dependent Gross-Pitaevskii equation; in this way the solitonic-vortex solution is obtained. The fact that the traditional axisymmetric vortex and the non-axisymmetric companion share the same topology, implies that the phase and density profile of the solitonic vortex can be obtained simply by a continuous evolution in the imaginary time of the imprinting of the phase of a traditional vortex. Typical phase and density profiles are depicted in figure 5.2. The simulations were performed for different values of the chemical potential and of the dimensional parameter γ.

The density profile

The in-situ density is determined, after the convergence to the stationary state, in the two different points: $A \equiv (x = \mathscr{R}_x/2, y = 0)$ and $B \equiv (0, \mathscr{R}_\perp/2)$. The different patterns of the phase between the axisymmetric system and the cigar-shaped system generate different velocity fields in the two cases: while in the pancake the velocity field is uniform around the core, and hence the atomic density, in the case of solitonic vortex the velocity field is maximal in the radial plane where the vortex lies. Thus, in order to minimize the energy, such a higher velocity region is depleted. The ratio of the two densities n_B/n_A is reported in figure 5.4. In the left graph of figure 5.4 the density ratio is plotted as a function of the trap aspect ratio for different values of the chemical potential. For the case of spherical traps ($\omega_x/\omega_\perp = 1$) the solitonic vortex becomes a standard vortex, *i.e.*, the density depletion is present only in the core and, for symmetry, $n_A = n_B$. For elongated BECs ($\omega_x/\omega_\perp < 1$) the density ratio

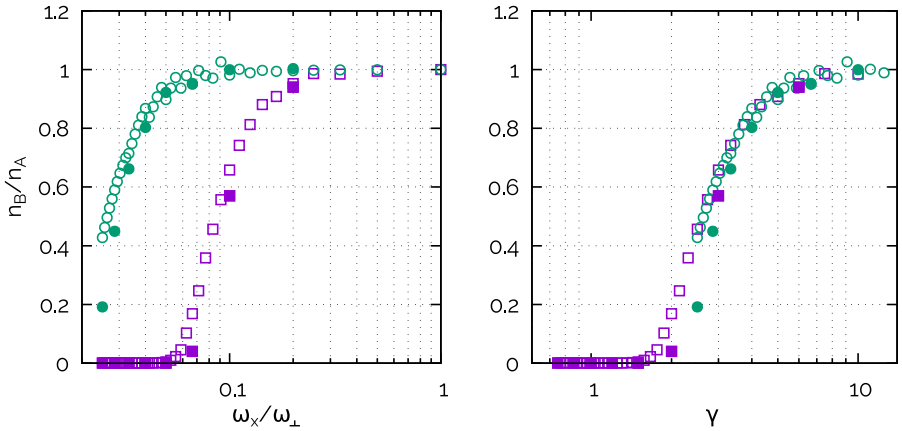

Figure 5.4: Ratio between the density in the solitonic plane of the transverse vortex and in the bulk BEC for $\mu = 30\hbar\omega_x$ (green circles) and for $\mu = 100\hbar\omega_x$ (purple squares). Void symbols report the results of 2D simulations, while filled ones are the results of 3D simulations.

spans in the range $0 < n_b/n_A < 1$. For $\omega_x/\omega_\perp \to 0$, *i.e.*, in the 1D regime, the density n_B vanishes and the defect is a dark soliton. The same data, plotted as a function of γ, are reported in the right plot of figure 5.4. In this case all the curves collapse onto a universal curve, confirming the dependence of the phenomenon on the dimensional parameter.

Three regimes

The curves of figure 5.4 permit to identify three regimes:

- *1D regime*: where the system supports soliton solutions;
- *bulk regime*: when the trap is symmetric and the lowest energy excitation is the traditional vortex;
- *crossover regime*: where the vortex assumes the peculiarities of the solitonic vortex. This regime can be in turn divided in two:
  - *strongly non-axisymmetric* ($1.5 \lesssim \gamma \lesssim 10$): the in-situ density profile is strongly modified by the tight radial confinement;
  - *weakly non-axisymmetric* ($\gamma \gtrsim 10$): the in-situ densty profile is very similar to the bulk regime and the anisotropy induced by the confinement becomes detectable only after a time of flight, as will be discussed in the next section.

In N. Parker 2004 the solitonic vortex[2] regime is identified with the 1D regime introduced above, while all the cross-over regimes are identified as weakly non-axisymmetric. Such a partitioning was suggested by the fact that excitations in the case of $\gamma \gtrsim 1.5$ (or aspect ratio 5.5 in the language of N. Parker 2004) show the dynamical behaviour predicted for vortices in non-axisymmetric traps, while for stronger radial confinement excitations cannot have stable vortical nature and

2 called also *svortex* in that work.

undergoes a soliton-like motion with an oscillation in the phase profile between a soliton kink and a vortex pattern. The crossover regime can therefore be extended below $\gamma \simeq 1.5$ and the solitonic vortex can be considered a cross-over state between soliton and vortex, which shows a more solitonic-like behaviour for $\gamma \lesssim 1.5$, and more and more a vortex-like behaviour for increasing γ.

5.1.2 Expansion Properties of the Solitonic Vortex

The structure of the solitonic vortex can be experimentally observed in our system only after a free expansion, in order to reduce the optical density of the sample to a level compatible with the absorption imaging. Thus a numerical simulation of the expansion of the in-situ wavefunction that hosts the solitonic vortex is a useful tool for the comparison with the experiment. Starting from the wavefunction obtained through the previously described imprinting, a 3D free expansion was simulated for $\gamma = 10$, rescaling the wavefunction in the transverse direction according to the Thomas-Fermi scaling law given by Castin et al. 1996; Massignan et al. 2003. The decrease of the density during the expansion makes the mean-field interaction to vanish, and hence the healing length increase. The size of the density depletion of the defect becomes then larger. A soliton expands keeping its overall density structure, *i.e.*, it widens, as the healing length increases, but maintaining its in-situ shape. In the case of solitonic vortex instead two peculiarities appear:

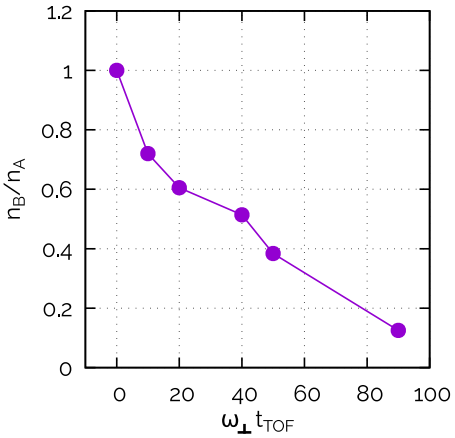

Figure 5.5: Evolution of the contrast of the solitonic plane as a function of the expansion time.

- a deepening of the density depletion of the solitonic plane;
- a twisting of this depletion plane around the vortex core.

Such peculiarities derive from the asymmetric flow around the vortex core. The result of the simulation is reported in figure 5.6 **(c)**, together with the results of the experiment described below (figure 5.6 **(a)** and **(b)**). The superposition of the velocity field of a transverse vortex with the velocity due to the free expansion leads to the formation of the characteristic bended planar structure appearing along the direction of the vortex core. The effect of the twisting of the density depletion around the hollow core of the vortex lasts as long as the mean-field interaction is not negligible. On the other hand, when

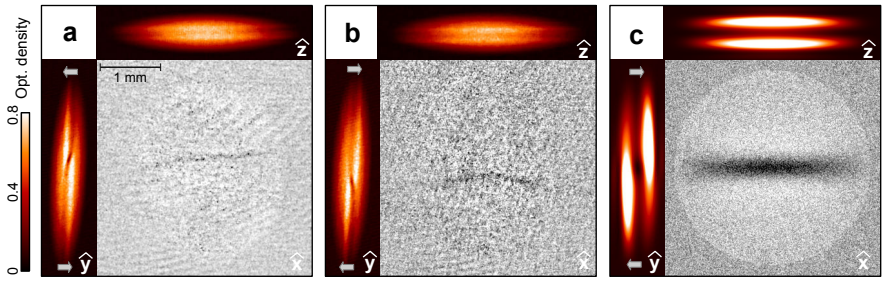

Figure 5.6: Experimental images through tri-axial absorption imaging after time of flight of a vortex **(a)** and an antivortex **(b)**. The panel **(c)** reports the numerical simulation of the expansion of a BEC with a solitonic vortex. From Donadello, Serafini, Tylutki, et al. 2014.

mean-field does not play any role the expansion becomes ballistic and the twisting stops. Long times of flight permit to highlight the effect of the anisotropy in the velocity field even in the weakly non-axisymmetric regime, as represented in figure 5.5, where the ratio n_B/n_A is plotted as a function of the expansion time rescaled to the radial trapping frequency. This effect will be also pointed out in the experiment described below.

EXPERIMENTS We experimentally reveal the behaviour pointed out by the numerical simulations by looking at BECs released from the trap after a long time of flight through the tri-axial absorption imaging described in section 4.2. Two representative cases are reported in figures 5.6 **(a-b)**, where the remarkable structure of the depleted plane twisted around the hollow vortex core is evident along y, while along z the depletion is straight.

Experimental protocol

The experiment is carried on in the tight regime I_t of the magnetic trap, for which the trap frequencies are $\omega_x/2\pi = 13\,\mathrm{Hz}$ and $\omega_\perp/2\pi = 131\,\mathrm{Hz}$ (section 3.3). BECs containing 1×10^7 atoms are produced with a negligible thermal component ($T < 200\,\mathrm{nK}$). The chemical potential is $\mu = 27\,\hbar\omega_\perp$. Vortices are created through a sufficiently fast temperature quench across the BEC transition, triggering the KZM. The temperature quench ($\sim 320\,\mathrm{kHz\,s^{-1}}$) is chosen to provide the formation of one vortex on average just at the end of the evaporation ramp, when the trap is released. Probing is performed through standard absorption imaging along the three orthogonal directions at the same time, exploiting magnetic levitation for reaching long time of flight (section 4.2).

The value of the dimensional parameter in the experiments is $\gamma = 27$. The system is therefore in the weakly non-axisymmetric 3D regime. This means that the in-situ effects due to the solitonic part of the solitonic vortex are weak. Nevertheless the possibility, and the need, to perform a very long time of flight through magnetic levitation permits us to visualize the effects of the anisotropic flow.

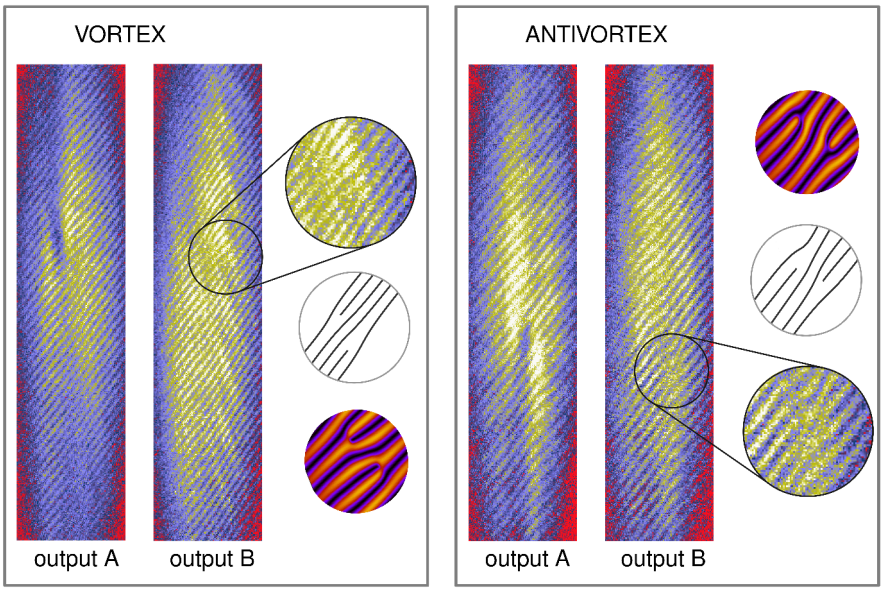

Figure 5.7: The output ports of the Bragg interferometer in the case of a vortex (left) and antivortex (right). The zooms of the regions where the double dislocations appear are reported with a guide for the eye and the results of a 2D numerical simulation of the interferometric technique. From Donadello, Serafini, Tylutki, et al. 2014.

The experimental and theoretical density profiles reported in figure 5.6 demonstrate their qualitative agreement. The main difference is the size of the defect, due to the reduced chemical potential in the simulated case that leads to a larger healing length. This smaller value of the chemical potential is dictated by the feasibility constraints on the computation of the 3D Gross-Pitaevskii equation.

SIGN OF CIRCULATION To demonstrate the presence of circulation around the hollow core of figure 5.6 **(a)** and **(b)**, and linking the sign of the circulation and the shape of the planar depletion after the expansion, a homodyne Bragg interferometry, described in detail in 4.2.1, was implemented. The experiment was performed in the same conditions as described before. The results are reported in figure 5.7. The output port A of the interferometer maintains a clear visibility of the shape of the planar depletion due to the expansion, while in the port B the signature of the circulation is highlighted through the expected double dislocations due to the homodyne detection method, in correspondence of the hollow core in the port A. A 2D numerical simulation of the Bragg interferometer was done for comparison with the experiments. Results in figure 5.7 confirm the link between the sign of the circulation and the asymmetry of the expansion, which is then clearly related to the asymmetric superfluid flow, depicted in figure 5.2.

5.2 VORTEX DYNAMICS

In the present section I will describe the dynamical properties of a transverse vortex in an elongated system. In the first part I will describe the origin and the experimental characterization of the precessional motion of a vortex in a harmonically trapped Bose-Einstein condensate. In the second part I will describe the rotational dynamics around the trap axis, which can be ascribed to a tilting of the plane where the vortex lies with respect to the radial plane.

5.2.1 Precession

A precession of the vortex line along equipotential orbits is expected in the case of harmonically trapped systems, both when the vortex experiences an axisymmetric potential and a non-axisymmetric one. I will give a generic picture of this motion explaining the physical arguments behind it. Then I will focus on the case of a vortex in a cigar-shaped system, that experiences a non-axisymmetric potential because of its transverse orientation. I will report the experimental characterization of the precessional motion of the transverse vortex.

As introduced in section 1.2.2.2, we have that the superfluid velocity field in the proximity of a vortex in $\vec{r}_0$ aligned along z far away from boundaries is given by the relation:

$$\vec{v} = \frac{\hbar l}{mr}\hat{\varphi} = \frac{\vec{k} \times (\vec{r} - \vec{r}_0)}{|\vec{r} - \vec{r}_0|^2}, \tag{5.3}$$

where the *spin vector* was introduced:

$$\vec{k} = \frac{\hbar l}{m}\,\hat{z}. \tag{5.4}$$

The velocity field of equation (5.3) is characteristic of a "bare" vortex, as it well describes the velocity field for $r \ll d$, with d the distance between the vortex and the closest boundary[3]. In the following paragraphs I will consider the vortex as a time-independent rigid cylindrical structure aligned along the z axis, not considering the possibility of bending.

Vortex hydrodynamics

The hydrodynamic formulation of the Gross-Pitaevskii equation (see 1.1.2) permits to interprete the superfluid flow as an irrotational compressible fluid, which is also isentropic because there is no heat transfer through it. A vortex moving in such a fluid can experience:

- a *buoyancy force*, due to the presence of density gradients;
- a *Magnus force*, experienced by a rotating object when moving in a fluid:

$$\vec{f}_{\mathrm{Mag}} = mn\,\vec{k} \times \left(\dot{\vec{r}}_0 - \vec{v}_{\mathrm{s}}\right), \tag{5.5}$$

3 In the present section the influence of other vortices on the dynamics of a vortex is completely neglected.

where $\vec{r}_0$ is the position of the vortex and $\dot{\vec{r}}_0$ its velocity and $\vec{v}_s$ is the velocity of the background superfluid flow.

The buoyancy force makes the vortex to tend toward regions with lower density. The Magnus force acts transversally to the direction of the vortex motion, deflecting it. For example in a homogeneous system the vortex moves with respect to the superfluid along a circular path, forced by the Magnus force acting as a centripetal force.

The role of boundaries

The presence of boundaries modifies the velocity pattern around a vortex: the vortex is not described by the "bare" field, equation (5.3), but it becomes a "dressed" vortex. In the case of a finite homogeneous systems the corrections due to the boundaries can be reproduced by exploiting the formal analogy with the electrostatic problem of determining the electric field due to a charge in presence of conductors. The motion of a vortex near the boundary is therefore equivalent to the motion of a vortex-antivortex pair in an infinite system, Mason et al. 2006. In the case of inhomogeneous systems instead the role of the vortex image is not straightforward, and the applicability of such a method is not universal in the study of the vortex dynamics in trapped systems, as discussed by Anglin 2002. The dressing of the vortex can be determined through an Euler-Lagrange equation for the phase as a correction to the bare-vortex velocity, in which the inhomogeneity enters through the Thomas-Fermi density profile; a detailed description can be found in Sheehy et al. 2004.

The vortex is expected to follow a trajectory along the equipotential lines of the trapping potential, as can be shown for example equating the Magnus force acting on the vortex and the force due to the trap inhomogeneity, which enters in the energy of the vortex:

$$mn\,\vec{k}\times\dot{\vec{r}}_0-\vec{\nabla}E_V(\vec{r}_0)=0, \tag{5.6}$$

where the vortex energy can be calculated through the approxiamtion of equation (1.37). In the calculation of the energy the contribution of the dressing correction to the superfluid flow can be neglected with respect to the diverging contribution of the velocity of the bare vortex, as pointed out by Sheehy et al. 2004. Such a divergence is regularized fixing the minimum distance from the vortex core from which the integral is calculated, usually such distance is the dimension of the vortex core, *i.e.*, the healing length ξ. Using the expression (1.37) for the vortex energy in equation (5.6) and solving with respect to the translational velocity of the vortex core $\dot{\vec{r}}_0$, one obtains:

$$\dot{\vec{r}}_0\simeq-\vec{k}\times\vec{\nabla}\mu(\vec{r}_0)\log\frac{\mathscr{R}_\perp}{\xi}. \tag{5.7}$$

In the case of a symmetric trap the solution of equation (5.7) is a circular orbit around the center of the trap with a precession frequency which depends on the gradient of the chemical potential at a distance

from the center equal to the radius of the orbit. The precession angular frequency points in the same direction of the spin vector $\vec{k}$ of the vortex. In the case of an elliptical trap the equipotential lines of the chemical potential are elliptic. Hence the vortex motion in such systems occurs along elliptic orbits. Also in this case the precession frequency points as the spin vector.

Inhomogeneity

Generally the motion of the vortex is derived via a variational Lagrangian approach which includes the inhomogeneity through the trapping potential. The additional inclusion of a vortex image gives only a small correction in the logarithmic factor (A. Fetter 2009). The vanishing of the normal component of the superfluid velocity on the boundary[4] is automatically taken into account in the vanishing density in the TF regime. Analytic results via the Lagrangian approach were obtained for axisymmetric (A. Svidzinsky et al. 2000) and non-axisymmetric (A. L. Fetter and J.-k. Kim 2001) systems. Compatible results can be derived through hydrodynamic approaches based on the Magnus force (Jackson et al. 1999) and on the Hamiltonian approach proposed by L.P. Pitaevskii 2013 for vortex rings in cigar-shaped Bose or Fermi gases and then generalized for the case of a solitonic vortex in a Fermi gas by Ku, Ji, et al. 2014.

For small γ there is no analytic results, the motion is expected to tend to the soliton one. In 1D such a motion is characterized by an oscillation with angular pulsation $\omega_x/\sqrt{2}$. Such a behaviour is pointed out numerically by N. Parker 2004.

Non-straight vortex

The dynamics of a bent vortex is not straightforward. The bending mechanism in the case of rotating condensates has been discussed by A. Svidzinsky et al. 2000; García-Ripoll et al. 2001a,b; Modugno et al. 2003. In elongated systems, like the one we have, the strong radial inhomogeneity is expected to enhance the bending mechanism, with possible effects on the dynamical behaviour of the vortex. In the following I will show that such effects are however small.

5.2.1.1 *Cigar-shaped BEC*

I will now focus on our cigar-shaped system, reporting the results of the experimental observation of single-vortex dynamics.

THEORETICAL MODEL The elliptic trajectories expected for the vortex motion can be parametrized by an *orbit parameter*. The orbit parameter is a dimensionless quantity describing the amplitude of the motion and it is defined as the ratio between the in-trap maximum amplitude of the motion along a given direction and the Thomas-Fermi radius along that direction, i.e, $\chi = x_{\max}/\mathscr{R}_x = y_{\max}/\mathscr{R}_\perp$. Since the real-time imaging of our experiment is limited to the radial horizontal direction, only the axial projection of the vortex motion can be

4 insured in the case of confined homogeneous systems by the vortex image.

followed. The precession can be projected along the axis of the trap using the orbit parameter. The expected axial precession period is:

$$T = \frac{4\left(1-\chi^2\right)\mu}{3\hbar\omega_\perp \ln\left(\mathscr{R}_\perp/\xi\right)} T_x, \tag{5.8}$$

where $T_x = \frac{2\pi}{\omega_x}$ is the axial trapping period, $\xi = \sqrt{\hbar^2/(2m\mu)}$ is the healing length and μ is the total chemical potential. Equation (5.8) was derived through a Lagrangian approach by A. L. Fetter and J.-k. Kim 2001 for a 3D disk-shaped non-axisymmetric condensate at $T = 0$ in Thomas-Fermi approximation, for which the ratio $\mathscr{R}_\perp/\xi \gg 1$. The same result comes from calculations with the hydrodynamic approach in Ku, Ji, et al. 2014. The quantity $\mu\left(1-\chi^2\right)$ is the local chemical potential along the vortex trajectory. From equation (5.8) it is evident that the period of a vortex depends on the amplitude of its motion, through χ, and on the number of particles in the BEC both through the chemical potential μ and the healing length ξ.

EXPERIMENTAL VERIFICATION Experimental observations of the single vortex dynamics through the μ-wave Pulsed Minimaly Destructive imaging technique are consistent with the theoretical predictions for the vortex precession. For a straight vortex line, radially oriented in a non-rotating elongated condensate, theory predicts an elliptic orbit in the plane orthogonal to the vortex line. This trajectory corresponds to an equipotential line in the condensate. Through the μw-PMD technique only the axial projection of the vortex motion can be probed.

Experimental protocol

The experiment is carried on in the tight magnetic trap I_t with frequencies $\omega_x/2\pi = 13\,\mathrm{Hz}$ and $\omega_\perp/2\pi = 131\,\mathrm{Hz}$. At the end of the evaporation ramp the condensate is almost pure ($T < 200\,\mathrm{nK}$ with $T_c \approx 700\,\mathrm{nK}$) with about 1×10^7 atoms. The critical temperature is crossed with a slope of $525\,\mathrm{kHz\,s^{-1}}$, leading to an average number of one vortex per condensate at the initial time of sampling, 250 ms after the transition crossing. The μw-PMD imaging is applied extracting a fixed amount of atoms, equal to $\sim 4\%$ of the total initial number for 20 consecutive times. To study the precession dynamics of the vortex the long sampling framing protocol was used (section 4.2.2), taking a shot every 84 ms. The raw images are fitted with a TF distribution and residuals are calculated. The successive picture of a single condensate are then pasted and displayed in sequences like in figure 5.8, where vortices appear as dark stripes.

Results

The position of the vortex with respect to the condensate was acquired with a Python software[5], written especially to filter the experimental images and to acquire the vortex position. This last task requires a human intervention to manually select the position. Vortex trajectories relative to samples reported in figure 5.8 **(b-c)** are

5 https://github.com/simondona/img-fft-filter-bec-tn

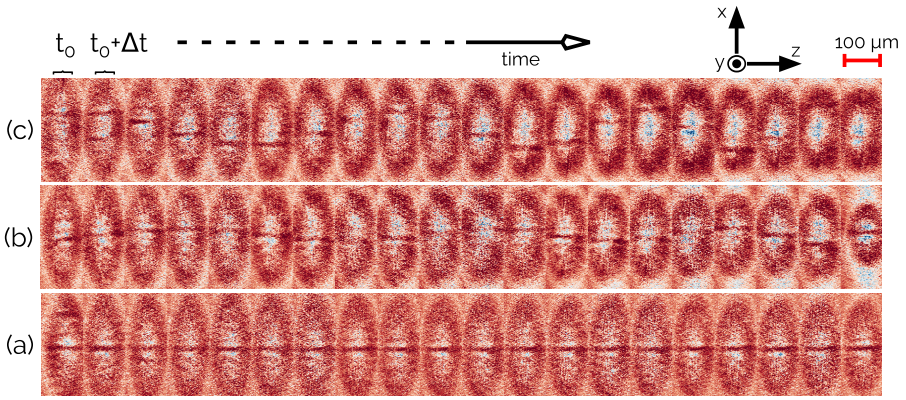

Figure 5.8: Examples of the axial evolution of a quasi-stationary **(a)**, small-amplitude **(b)** and large-amplitude **(c)** vortex, as probed through μw-PMD.

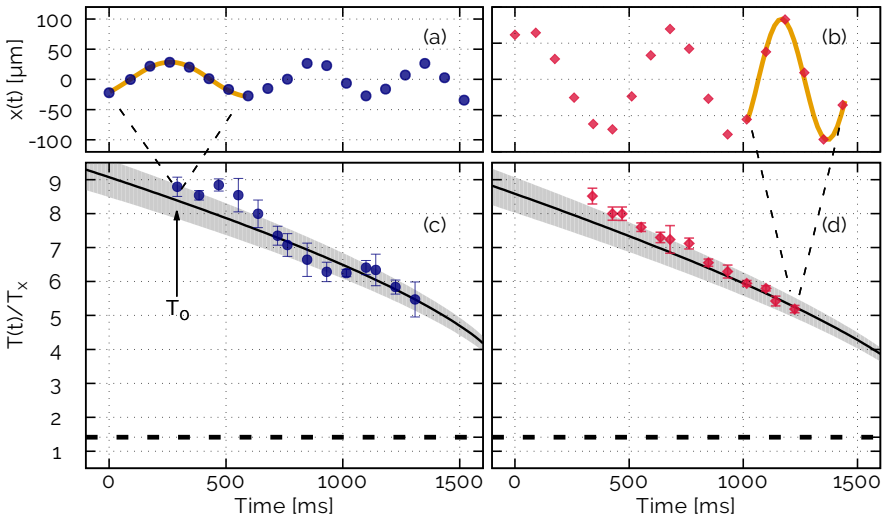

Figure 5.9: Axial trajectories of the vortices reported in figure 5.8 **(b) (a)** and 5.8 **(c) (b)**. The instantaneous period is plotted in panels **(c)** and **(d)** respectively, together with the theoretical prediction.

shown respectively in figure 5.9 **(a-b)**. The position of the vortex in the outcoupled sample reflects its position in the original condensate, with the assumption that χ remains constant during the expansion. This assumption is based on the expectation that all the distances scale in the same way during the slow axial expansion. The axial TF radius after expansion is $\mathscr{R}_x \approx 250\,\mu$m, giving a scale factor of ~ 0.6 between in-situ and expanded lengths. In order to compare the results of the experiments with the theoretical prediction of equation (5.8), the decrease of the BEC atom number frame by frame has to be taken into account. The orbit parameter χ is determined calculating the ratio between the maximum amplitude of the trajectory and the instantaneous axial TF radius after the expansion. The evolution of the atom number during an experimental run with

the μw-PMD was characterized stopping the extraction at different times and measuring the residual atom numbers with a traditional destructive absorption imaging after a long time of flight. The characteristic behaviour of the atom number is reported in green in figure 5.10; the evolution of the atom number without any action is also reported in grey. Data in figure 5.10 was fitted with a second-order polynomial function for estimating the number of atoms at arbitrary times. The extraction of the small sample of atoms from the BEC occurs in a homogeneous way, thus the gradient of the density remains unchanged, and hence also the vortex precession maintains its amplitude unperturbed. As one can see from the plots in figure 5.9 **(a-b)** the amplitude does not change during the observation time. However the total number of atoms $N(t)$ is time dependent, and hence also the chemical potential $\mu \propto N^{2/5}$, the Thomas-Fermi radius $\mathscr{R} \propto \mu^{1/2} \propto N^{1/5}$ and the healing length $\xi \propto \mu^{-1/2} \propto N^{-1/5}$. The reduction of the Thomas-Fermi radius implies that the orbit parameter of a vortex changes in time during the observation through μw-PMD. This effect has to be included in the comparison between theory and experiments. The decrease of the atom number in the condensate with time gives a decrease of the vortex precession period. An instantaneous period at time t can be defined as the period obtained from a sinusoidal fit to the measured vortex position in a time interval centered at t and spanning about one oscillation. In figure 5.9 **(c-d)** the experimental instantaneous period $T(t)$ of trajectories in figure 5.9 **(a-b)** is plotted as a function of time and compared to the theoretical prediction of equation (5.8), taking into account the measured atom number evolution $N(t)$, reported in figure 5.10. The theoretical curve is given inside a shaded area representing an uncertainity in the atom number of 20%, which is the major limitation on the experimental reproducibility from shot to shot. The agreement between theory and experiment is good. The agreement between theory and experiment can also be inspected for a statistical sample of measures looking at the period as a function of the square of the orbit parameter (trajectory amplitude). Considering the period determined from the sinusoidal fit on the first time span T_0 and the orbit parameter χ_0^2 calculated from the corresponding amplitude and the measured TF radius, we obtain the points reported in figure 5.11 **(a)**. In the same plot the theoretical expectations are reported with the black line for an atom number of $N = 9 \times 10^6$ atoms, which is the mean number during the time period on which the fit is performed. No free parameters are used, the

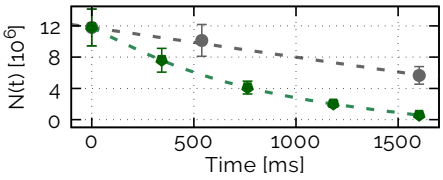

Figure 5.10: Evolution of the atom number with (green) and without (gray) outcoupling.

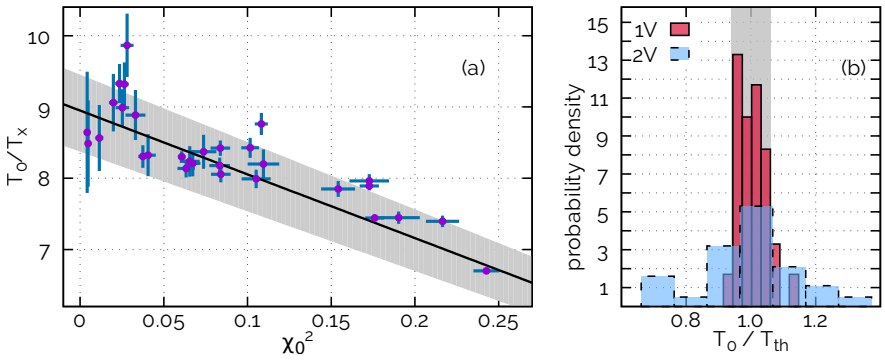

Figure 5.11: **(a)** Period T_0 extracted from experimental vortex trajectories as a function of χ_0^2, solid line is theoretical prediction. **(b)** Probability density of the measured period T_0 vs theoretical one T_{th} for one (red) and two (light blue) vortices.

gray shaded area represents, as before, an uncertainity of 20% on the atom number.

In figure 5.11 **(b)** the histogram of the ratio T_0/T_{th}, where T_{th} is the expected period calculated with equation (5.8), is reported in red for single-vortex trajectories (same points of figure 5.11 **(a)**), and in light blue for trajectories extracted from samples containing two vortices. The number of events is respectively 30 and 27. For the single-vortex case the histogram shows a mean value of $T_0/T_{\text{th}} = 0.97$, with a standard deviation of 0.04.

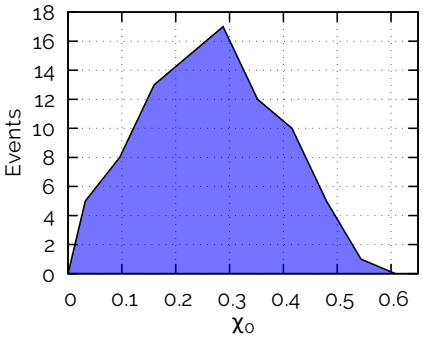

Figure 5.12: Orbit parameter distribution.

This remarkable agreement is not trivial because of the assumptions in the derivation of equation (5.8), i.e., $\chi \ll 1$ and a rigid straight vortex line. In elongated BECs indeed the effect of bending due to the strong radial inhomogeneity is expected to be stronger than in oblate samples, in particular for larger χ. Observations in our experiments show instead that corrections on the period are small, possibly on the order of the logarithmic corrections of equation (5.8). This low impact of bending of the vortex lines could be ascribed to the rather small difference between the length of a straight and a bent vortex, given the same χ, and also to the however similar vortical flow pattern, leading to a small difference of the key quantities entering in the hydrodynamic derivation of equation (5.8) for the two cases. The distribution of the vortices as a function of their initial orbit parameter is reported in figure 5.12.

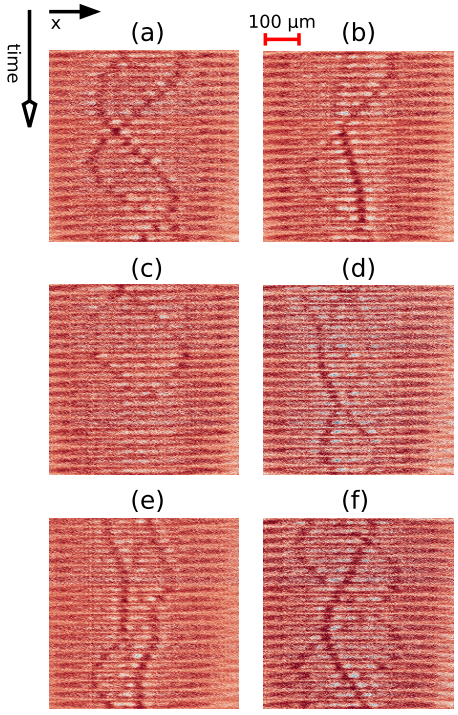

Figure 5.13: Squeezed sequences of multi-vortex samples.

Because of the stochastic method of generation of vortices, sometimes more than one defect are present in the condensate. Some examples of multi-vortex condensates are reported in figure 5.13, where the transverse direction is squeezed with respect to figures reported in figure 5.8 in order to enhance the visibiliy of the trajectory. These images were taken to probe the crossing of vortex trajectories with a refined time resolution: the time interval between adjacent extraction is in this case fixed by the dense sampling protocol, $\Delta t = 28\,\mathrm{ms}$ (section 4.2.2). A closer insight on these cases is the argument of the next chapter. In figure 5.11 **(b)** the histogram of T_0/T_{th} for the case of two vortices appearing in the same sample is reported in light blue, such a distribution shows a mean value of 0.96, compatible with the single vortex case, but with a standard deviation of 0.14, which is 3 times larger. Such a broadening could be linked to an effect of interactions between the two vortices, which slightly modifies trajectories from the ones predicted for single or non-interacting vortices; these modifications affect the determination of the period through the simple model used so far. The broadening of the light blue distribution in figure 5.11 **(b)** can thus be ascribed to interactions occurring between vortices. The role of such interactions will be discussed in the following chapter, where the necessity of a more refined probing technique will be pointed out.

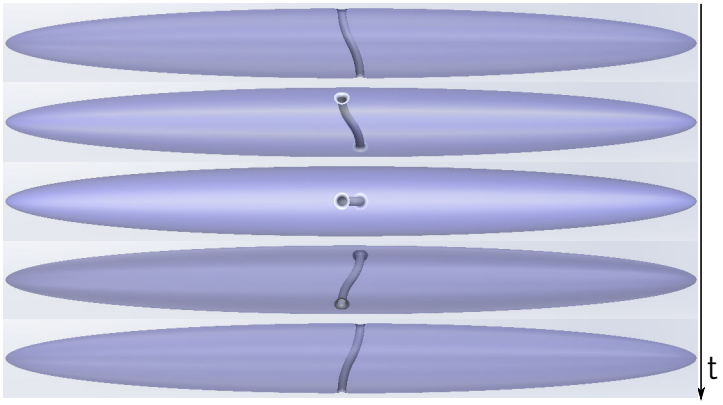

Figure 5.14: A tilted vortex (the tilting angle is exagerated in the figure for clearity) rotates around the axis of the cigar.

5.2.2 Spinning

The presence of a stationary vortex in the center of the trap is a rare event, because of the highly turbulent way in which defects are formed through Kibble-Zurek mechanism. Nevertheless it can happen to observe vortices whose oscillation amplitude vanishes, as reported in figure 5.8 **(a)**. Such a configuration is ideal to study the evolution of the orientation of the vortex line in the radial directions in a clean way, if the orientation angle in this plane can be accessed. The rf-SMD imaging technique permits to do that, as described in section 4.2.3. In the present section I will describe the experimental observation of the radial motion of a transverse vortex. This observation and the experimental characterization of the mapping of the radial orientation on the radial profile done with the particular outcoupling technique introduced in 4.2.3.1 justify the interpretations of the results of the experiment about vortex-vortex interactions reported in chapter 6.

A quasi-static vortex in the center of the condensate can rotate around the axis of the cigar because of the absence of any preferred orientation in the radial plane. Such a rotation, to which I will refer as *spinning*, is schematically depicted in figure 5.14. A straight vortex, exactly centered in the trap and aligned to a radial axis, is stationary, but if there is a tilting of the vortex line by an angle α with respect to the radial direction, as in figure 5.14, then the vortex moves. This tilt indeed implies an increased length of the vortex, and hence of its energy. Interpreting the vortex as a spinning top with an angular momentum given by the quantized vorticity, a tilting in its axis induces a torque which causes a rigid rotation of the vortex line with a fixed tilting α and a precession in the azimuthal angle $\theta = \Omega t$. The torque-induced rotation introduces a classical (non-quantized) angular momentum along the axis of the cigar. Such an angular momentum is conserved because of the rotational symmetry of the BEC around the

x axis. A model to quantify such a phenomenon will be developed in the near future.

The observation of a quasi-stationary vortex with radial spinning is reported in figure 5.15. The presence of spinning is revealed by the oscillating pattern in the residuals, highlighted through a divergent color palette. All the time slices were fitted with the phenomenological expression (4.19) to extract the parameter δ, which encodes the orientation of the vortex line in the radial plane. A few examples of these fits are reported in figure 5.16 for different values of δ. The period of the spinning signal is deduced to be $T_{sp} = 225\,\text{ms}$. All the points are then collapsed into a single period, which spans an orientation angle of 2π. The δ values of each point are plotted as a function of the orientation angle and compared with the expected characteristic curve obtained through the numerical simulation of the sweep outcoupling (section 4.2.3.1). The figure 5.17 reports the spinning-vortex points with cyan squares and the simulations result with a green line. The range in which δ can span is between $-\frac{\pi}{2}$ and $\frac{\pi}{2}$. These extremes correspond to horizontal vortices with different signs. The range of δ is limited to π because a vertical vortex has a velocity field orthogonal to the moving outcoupling surface, thus the effect of the interference discussed in 4.2.3.1 is not present. The sign of a vertical vortex cannot be determined through δ, but only the direction of vorticity can be figured out. The behaviour extracted from the spinning vortex of figure 5.15 is in qualitative agreement with the results of simulations. A systematic effect of saturation at $-\frac{\pi}{2}$ is shown by the experimental points as a plateau. The origin of such a saturation is not yet clear and will be further investigated. Simulations suggest that the pattern (4.19) is extremely sensitive to the direction of the vertical integration of the residual profiles, pointing out that a slight deviation ($\lesssim 1^\circ$) from the vertical, due for example to a non perfect alignement of the camera, can introduce some systematic effects. The misalignement of our camera is measured to be less than 1°, hence some saturation effect can be ascribed to this misalignement[6].

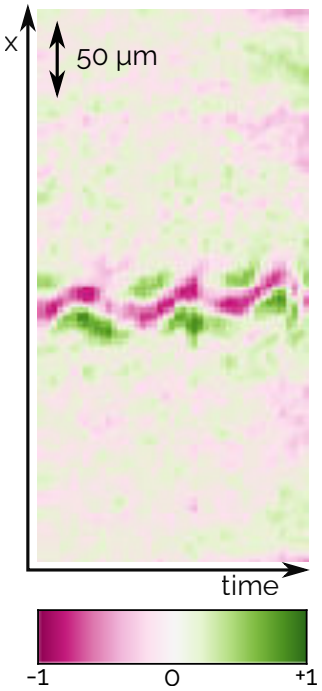

Figure 5.15: The evolution of a stationary spinning vortex observed through rf-SMD technique.

6 The measure is done looking at the free fall of a sample along the vertical direction, determined by the combined action of gravity and trapping magnetic gradients, and measuring the horizontal displacement on the CCD.

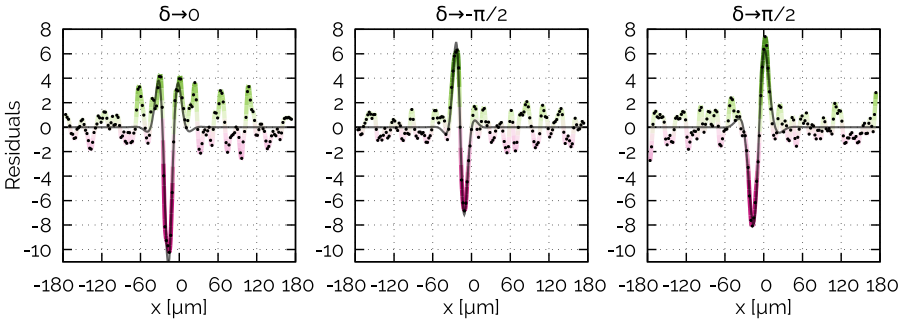

Figure 5.16: Examples of fitting the function (4.19) to three slices of data of image 5.15 showing different asymmetries. Black points are the residuals calculated as described in section 4.2.3.1 and the gray line is the fitted function. The coloured line is just a guide for the eye to recover the profile of figure 5.15 (spline through the points).

5.2.2.1 *Characterization of rf-SMD Vortex-orientation Mapping*

In order to verify the correspondence between the fit parameter δ and the radial orientation angle θ a hybrid imaging technique between rf-SMD and full-expansion multi-axial time of flight was implemented. The technique consists in performing the rf-SMD imaging of the sample 10 times, and finally release the trap and perform a simultaneous absorption imaging of the entire cloud along both the radial and axial directions. The final expansion is done in presence of the magnetic levitation. The limited extraction through rf-SMD permits to have still rather large samples for the full expansion. In this way the radial orientation angle is directly accessible at the end of the evolution time observing the optical density profile integrated along the axis of the trap, while the time evolution of the vortex can be followed during the previous 120 ms through the rf-SMD. If the vortex does not show evident spinning, the mean parameter δ, calculated averaging all the parameters obtained fitting the rf-SMD profiles, can be directly related to the orientation angle θ. Such a orientation angle can be directly determined from the axial imaging. To distinguish between horizontal vortex and antivortex the radial profile can be used simply looking at the kink in the planar expansion of the transverse vortex. The analysis was performed considering only straight vortices, when observed along the trap axis, which also lie in the central region of the condensate, when observed from the radial direction. In this way the determination of the sign can be done looking at the kink orientation in the radially integrated optical density, and the effects of bending of the vortex line, which can modify the residual pattern in a non characterized way, are screened out. The results of these series of measurements are reported with purple circles in figure 5.17, together to the previously described data. The behaviour of the purple data is in qualitative agreement with the spinning vortex and with the numerical simulations, justifying the discrimination between ori-

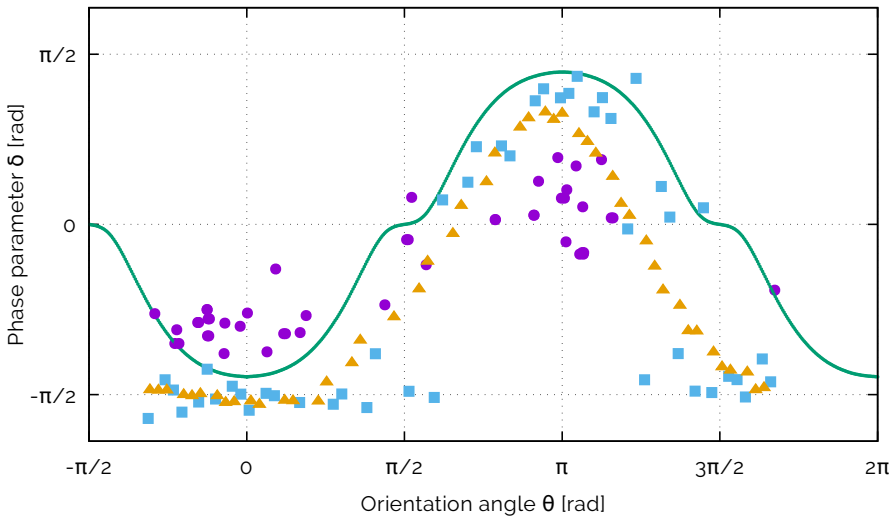

Figure 5.17: Relation between the orientation angle θ, observed along the trap axis, and the fit parameter δ determined from the radially-integrated profiles: **(a)** as calculated from simulations of the outcoupling (section 4.2.3.1) (green line), **(b)** extracted from the spinning vortex collapsing the points on a single period (cyan squares), **(c)** as in **(b)** but averaged on 100 ms (yellow triangles) and **(d)** experimentally characterized through the hybrid technique as described in the text (purple circles).

entations and signs done in the following chapter. A reduced range of variability of the parameter δ is observed, with a wider dynamic range to negative values. Such a reduction of the range can be related to the fact that data obtained through the hybrid technique have the δ parameter mediated on the whole span of the rf-SMD imaging, hence each point mediates the effect of possible spinning on about $\sim$ 100 ms. The results of the spinning vortex are then mediated on a range of 100 ms to permit comparison with the hybrid-imaging data. The mediated data for the spinning vortex are reported in figure 5.17 with yellow triangles. These points actually have a reduced span, as in the case of the purple circles. The significant scattering of the purple points are due to a not optimal signal-to-noise ratio of the residual profiles. Next implementations of rf-SMD need a special attention on SNR for obtaining quantitative information about the radial orientation of the vortex lines.

6 VORTEX INTERACTIONS

CONTENTS

In the present chapter I will focus on the observation and simulation of vortex-vortex interactions in a cigar-shaped condensate. In a first section I will point out the importance of the vortex-vortex interaction mechanisms in many fields of physics, showing the advantage of employing elongated axially symmetric BECs to experimental studies in this context. Then I will introduce some first evidences of interaction between vortices observed through μw-PMD technique, which motivated the developement of the novel rf-SMD imaging. In the last part of the chapter I will report the results we obtained using this last technique, pointing out the observation of some new, unexpected phenomena, wich are also supported by numerical simulations.

6.1 THE ROLE OF VORTEX INTERACTIONS

The interaction among vortices plays a central role in many phenomena, both in the classical and quantum regime. The turbulent flow is indeed a common situation in the problems of fluid dynamics. The approach to complex problems like turbulence is very difficult, both from the experimental and theoretical point of view. A way to tackle such complex phenomena is to reduce them to elementary situations that are easier to handle, and then build up a complete model based on these elementary results. An example of problem reduction is the study of quantum turbulence for shedding light on its classical counterpart. Turbulence is indeed a singular field, where the quantum description is easier than the classical one. The simplification of such a problem in the quantum treatement is due to the quantization of vorticity, which makes vortices well localized objects. In the classical case vorticity is a continuous field which can assume arbitrary values, while in the quantum framework it is concentrated in the region occupied from the vortex tube and can assume only fixed values. There is also no viscosity damping the motion. As pointed out

in the previous chapters a superfluid is like an ideal compressible irrotational fluid.

Descriptions

The description of a quantum fluid is generally given in terms of the Gross-Pitaevskii equation, described in section 1.1.1. Such a description is particularly interesting because vortex quantization naturally appears. The GPE reproduces the Euler equation describing the behaviour of a compressible inviscid fluid, in the large scale, while it includes quantum effects which permits vortex reconnection, at the scale of the healing length. A reconnection is a process occurring when two near vortices exchange their tails with compatible vorticity, as sketched in figure 6.1. When vortices are almost touching each other, a sort of "uncertainity principle" allows the local exchange of the vortex tails. In the classical case reconnection occurs because of the presence of a finite viscosity, which is unnecessary in the quantum case. The Gross-Pitaevskii equation is also known as non-linear Schrödinger equation and plays a role in non-linear optics for the description of optical vortices. The derivation of the GPE is based on the assumption of weakly interacting particles, being it a mean-field result. Its application for the description of a dilute gas is then fully justified, while it can break down in the case of strongly interacting systems. Nevertheless the GPE is often used for the qualitative description of superfluid helium (Roberts et al. 2001). The numerical integration of a 3D GPE for a turbulent system is computationally very demanding. Normally simulations are done through the so called *Biot-Savart* method. Such a method describes a vortex as a wire carrying a current which moves in the magnetic-field-like velocity field induced by the others. This method reproduces the Euler-like dynamics on the large scale but lacks the quantum mechanism for the reconnection. A reconnection mechanism must be introduced when two vortices approach a critical distance (Schwarz 1988). Models for the mechanism of isolated vortex reconnection are then needed. Analysing few-vortex systems through numerical simulations of the GPE or through experiments a deeper understanding of such basic processes can be formulated. Studies can be carried on in superfluid helium or atomic BECs.

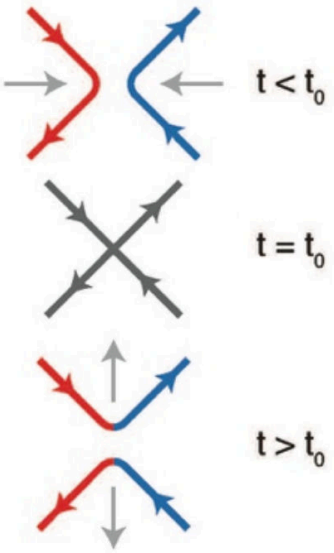

Figure 6.1: Reconnection as tail exchange, from Fonda et al. 2014.

Helium

Typical studies of vorticity in helium consider homogeneous systems far away from boundaries, being this situation the most com-

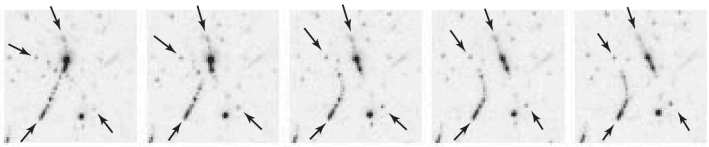

Figure 6.2: Reconnection event in superfluid helium revealed with tracer particles, from Bewley et al. 2008.

mon one for helium, which is contained in large bucketts where the effects of the walls can be neglected. Theoretical (Nazarenko et al. 2003) and numerical (Koplik et al. 1993; De Waele et al. 1994; Tebbs et al. 2011; Kerr 2011; Zuccher et al. 2012) models for the vortex reconnection were proposed. GPE simulations are performed imprinting stationary vortices, with diferent orientation angles, in the uniform solution and then letting the system evolve. Reconnection is shown to occur through a local alignement of the vortex lines in the anti-parallel configuration, forming a planar hyperbola, before exchanging the tails. Such simulations catch the basic physics of the reconnection process but they completely neglect the role of a non-zero relative velocity of the vortex lines, which can play an important role in the process, as will be pointed out in the next section. On the experimental hand the characterization of an isolated reconnection is difficult. Indeed vorticity in helium can be generated through the rotation of the container, by applying a heat current, stirring the fluid or through KZM, generating in each case an extended tangle of vortex lines. The direct imaging of vortex lines in helium is also difficult because of the small value of the healing length, $\xi \sim 1$ Å. Recently vortex reconnections (Bewley et al. 2008) and Kelvin waves (Fonda et al. 2014) were experimentally observed using submicron tracer particles trapped in the vortex core, which permits the direct imaging of the paths of the vortex lines, as depicted in figure 6.2.

Atomic BECs

Atomic BECs are ideal systems for studying many- and few-vortex dynamics, thanks to the variety of vortex production and probing techiques reviewed in chapter 2. Several experimental techniques permit to trap the atomic gas in traps with tunable flat or elongated geometries, where the role of boundaries and density inhomogeneity can be studied in a clean environment.

Interacting quantum vortices have been extensively studied in the context of rotating systems (Madison et al. 2000; Abo-Shaeer et al. 2001; Engels, Coddington, Haljan, and Cornell 2002; Coddington et al. 2003; A. Fetter 2009) and of flat systems (B. P. Anderson, Haljan, Wieman, et al. 2000; Weiler et al. 2008; Neely et al. 2010; Freilich et al. 2010; Middelkamp et al. 2011; Navarro et al. 2013; Kwon, Moon, et al. 2014). Both in rotating and flat systems the vortices align along a preferential direction because of the minimization of the energy. In the case of the rotating system, minimization occurs for vortices parallel to the rotation axis, while for flat system vortices align along the

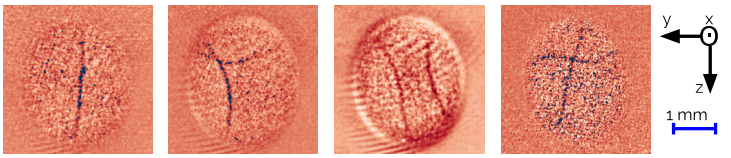

Figure 6.3: Axial view of our condensate after time of flight, showing the random alignement of vortex lines in the radial plane.

shortest direction, which is in this case parallel to the symmetry axis of the sample. The common point of these two kinds of configuration is the long-range nature of the vortex-vortex interaction. Such a long-range interaction is due to the velocity field around the vortex core, that scales as r^{-1}, where r is the distance from the vortex. Such a long-range interaction is responsible, for instance, for the formation of vortex lattices in rotating systems. In the case of few-vortex flat systems the interaction of pairs of vortices was studied, in the cases of corotating vortex pairs (or vortex dipole) and vortex-antivortex pairs (N. Parker 2004). In all these cases vortices behave as pointlike particle interacting via a long-range interaction in a quasi-2D background and the common alignment suppresses the possibility of crossing of the vortex lines.

Novelties in a cigar

Things drastically change in the case of axially symmetric cigar-shaped systems. The least energetic state of vorticity of such systems is the transverse vortex, as described in the previous chapter. The exact cylindrical symmetry introduces a full degeneracy on the orientation of the vortex line in the radial plane, as it is evident from the pictures in figure 6.3, where vortex lines are imaged along the axis of the cigar after a time of flight. The transverse confinement modifies the velocity flux around the vortex core, which then quickly vanishes in the range of the transverse size, as described in section 5.1.1, where the properties of a transverse vortex were investigated. In this way the range in which vortices influence each other is reduced to the order of the transverse size of the sample, hence suppressing the long-range character of the interaction. The radial confinement is thus a tunable parameter permitting to modify the range of the vortex-vortex interaction. If vortices lie on different orbits, which are characterized by different precession velocities, one immediately realizes the richness of the possibilities of different colliding trajectories, in terms of relative angle and relative velocity, in the case of a cigar-shaped sample. The interactions in such a system is a fully 3D one, involving the vortex as a filamentary structure instead of a pointlike particle as in flat systems, where the interaction is essentially 2D for the reasons explained before.

A stochastic method for the generation of the defects, like the Kibble-Zurek mechanism, is suitable for probing vortex-vortex interactions in cigar-shaped condensate if a real-time barely-destructive imaging can be implemented. The randomness of the KZ defects permits to

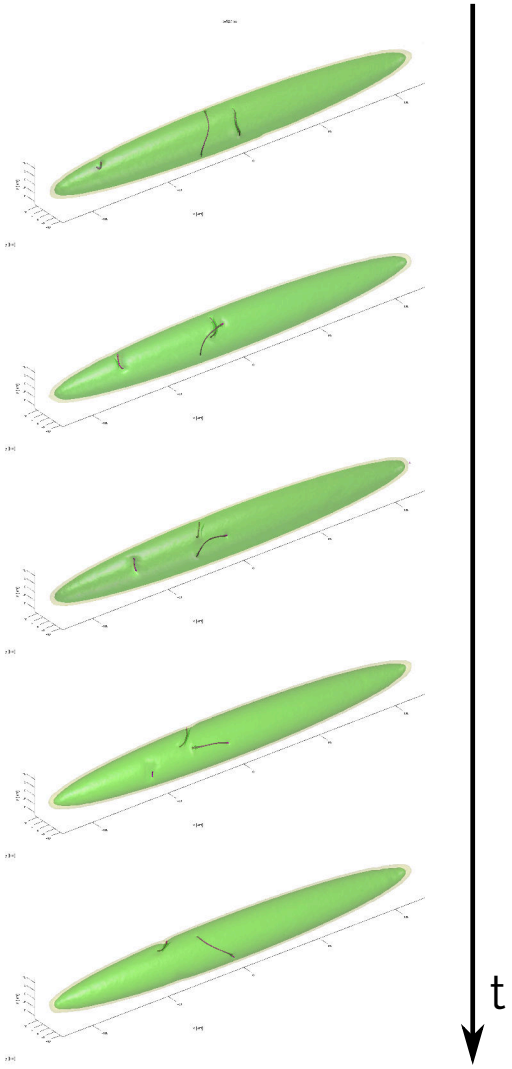

Figure 6.4: Rotational dynamics of vortices, simulation by N. Proukakis 2016.

cover a large number of initial conditions in the repetition of the experiment without any adjustement of the experimental setup. Tuning the duration of the temperature quench across the transition, a suitable average number of defects at the probing time can be generated. The repetition of the experiment many times permits then to cover all the possible orientation angles and relative velocities.

The dimensionality of the interactions open the way to the observation of unexplored mechanisms in the dynamics of vortices in atomic BECs. The degeneracy of the orientations of the vortex line in the radial plane permits the activation of radial motions of the vortex line and the possibility to observe crossing of the vortex lines, making an elongated system an ideal benchmark to test the reconnection mechanism.

RADIAL DYNAMICS The absence of any constraint on the alignement of a vortex in the radial plane introduces the possibility for approaching vortices to rotate around the trap axis. In fact, a torque acting on the vortices can be generated via the interaction, and hence a rotational motion in the radial plane can be activated. Such a behaviour was observed for example in numerical simulations of the post-quench dynamics in an elongated BEC by N. Proukakis 2016. A few snapshots of such simulations are reproduced in figure 6.4, where slowly approaching vortices rotate in the radial plane and avoid the collision. Also an axial stretching of the vortex line, following for example a reconnection, can activate a radial motion because of the action of a torque, as already discussed for the spinning vortex in section 5.2.2.

RECONNECTIONS Another important mechanism, whose appearance is favoured by the elongated and axially symmetric configuration of the sample, is the reconnection. In particular vortices lying on different orbits can impact, showing the effect of a non-zero relative velocity of the vortex pair.

It is worth mentioning that the experimental study of few-vortex dynamics in elongated Bose-Einstein condensates is a major novelty of the present work. The richness of the information that can be obtained from a combined experimental and numerical study on such systems will probably be helpful in improving the comprehension of the basic mechanisms of vortex interactions.

6.2 OBSERVATION OF VORTEX INTERACTIONS

In the present section I will present our experimental results on vortex-vortex interactions by following a historical path. First I will describe some signatures of such interaction mechanisms observed when studying the dynamics of transverse vortices in our cigar-shaped Bose-Einstein condensate. These signatures fed the interest to develop a more robust and precise technique for probing the vortex dynamics. A collaboration with Carlo Barenghi and Luca Galantucci from Newcastle University started in order to provide a more complete insight on the experimental observations through numerical simulations of the 3D Gross-Pitaevskii equation in a system similar to the experimental one.

6.2.1 First Evidences of Interactions

As introduced in the previous chapter, the μw-PMD technique was applied for the characterization of the dynamical properties of a single vortex, but also to follow the dynamics of systems with more

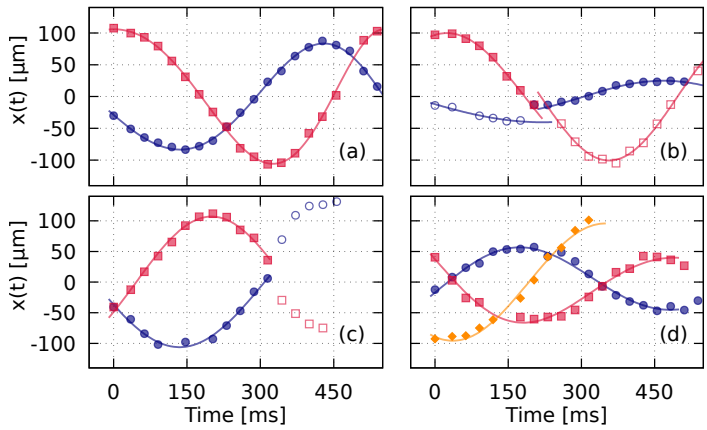

Figure 6.5: Trajectories of the experimental data of figure 5.13, showing many vortices. The full or void points describe respectively high or low visibility of the defect.

vortices, as shown in figure 5.13. The information about such systems is however less precise. Here I will report some effects that can be observed through μw-PMD technique and can be interpreted as signs of vortex-vortex interaction (Serafini et al. 2015).

Evidence of Interactions: Vortex-trajectory

In figure 6.5 **(a-d)** the trajectories inferred respectively from data of figure 5.13 **(a-d)** are reported. The change in the visibility is rendered in the plots with the void points. A first suggestion about the possibility to observe effects driven by the interaction between vortices was the occasional presence of discontinuity in the trajectory of a vortex pair near the point of the minimum axial distance between them, as depicted in figure 6.5 **(b)** in contrast to an unperturbed one like in figure 6.5 **(a)**. The visibility of the defects can also change after that point as in figure 6.5 **(b-c)**. The presence of a discontinuity in the trajectory seems to be related to the relative velocity between vortices, in particular the slower ones give a larger probabilty to observe modified trajectories.

As anticipated in the prevoius chapter, the determination of the instantaneous precession period of vortices in pairs is also characterized by a broader distribution around the expected value with respect to the single-vortex case. This behaviour is evident in the histogram of figure 5.11, where the probability density of the measured period versus the theoretical one is plotted for single-vortex and two-vortex systems, the last being more broadly distributed with respect to the first one. This can be due to the discrepancy between the expected trajectory from the single-vortex precession model and the observed one when more vortices are present in the system. The model of the precession of a single vortex does not fit the data with the same precision, leading to a larger spread in the fit parameters.

Evidence of Interactions: Vortex lifetime

Vortices are excitations that are topologically protected, as introduced in section 1.2.2. Nevertheless they are subject to dissipation

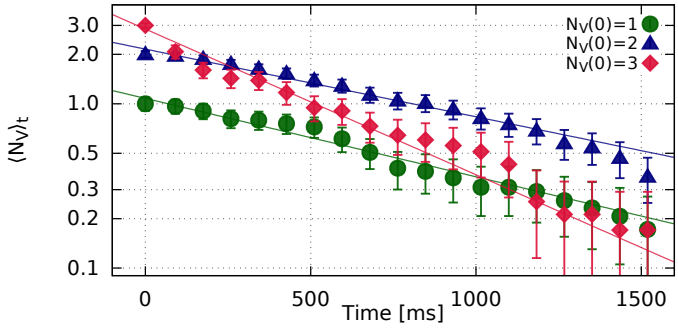

Figure 6.6: Average vortex number, $\langle N_V \rangle$, remaining in a condensate at time t starting from configurations with $N_V = 1$ (circles), 2 (triangles) and 3 (diamonds) at $t = 0$. Solid lines are exponential fits.

processes (N. G. Parker et al. 2007). Such processes can be due to thermal or to hydrodynamic instabilities. The first class is due to the presence of a thermal component in the gas, hence vortices scatter the thermal excitations (phonons), generating a friction acting on the vortex motion. Vortices are subject to a loss of energy, but they cannot simply vanish, because of their topological nature. The loss of energy manifests in a drift of the vortex trajectories toward the outer region of the condensate, where they eventually disappear in the vanishing density edge. Hydrodynamic instabilities are instead temperature independent mechanisms, like sound emission due to Kelvin wave excitations of the vortex tube or due to reconnection processes.

We measured the lifetime of vortices by counting their average number $\langle N_V(t) \rangle$ remaining in the system as a function of time t. This was done for systems starting with different initial number of vortices ($N_V(t = 0) = 1, 2, 3$) in order to point out the effects of the presence of many interacting vortices on the vortex lifetime. Results are reported in figure 6.6. Data of figure 6.6 were fitted with an exponential decay to extract a characteristic lifetime $\tau_{N_V(0)}$. The extracted lifetimes are:

$N_V(0)$	$\tau_{n_V(0)}$
1	910(100) ms
2	1050(100) ms
3	490(100) ms

The result for $N_V(0) = 1$ is compatible with previous measures (Lamporesi, Donadello, Serafini, Dalfovo, et al. 2013; Donadello, Serafini, Tylutki, et al. 2014). The lifetime for $N_V(0) = 2$ is consistent with the one for a single-vortex system, while the case of $N_V(0) = 3$ experiences a faster decay. The consistency between the single-vortex and the two-vortex cases is puzzling because, given the geometry of the system, vortices have a large probability to cross each other, possibly triggering in this way reconnection processes with strong effects on the vortex dynamics.

Interpretation of the lifetime puzzle

Observations about the vortex lifetimes suggest the occurrence of a mechanism that suppresses the reconnection processes, keeping the total number of vortices unchanged. The roles of the relative velocity and of the relative angle in the interaction processes are expected to be important in the cigar-shaped geometry. In Serafini et al. 2015 we suggest the possible role of fly-by dynamics, *i.e.*, the tendency of two nearly parallel or anti-parallel vortices to avoid each other, and of double reconnections, *i.e.*, two consecutive reconnections of the vortices to avoid the stretching of filaments, and hence the associated energy cost, due to a single reconnection process. Double reconnections are predicted by Berry et al. 2012 through a purely cinematic argument, and was recently suggested to play a role in the collision of cosmic string (Verbiest et al. 2011), which shows some analogies with vortices in superfluids (R. L. Davis et al. 1989). Both these mechanisms can depend on the relative velocity of the two vortices, which fixes the duration of the interaction stage. These results triggered the interest to investigate more deeply the physics of two-vortex systems, with the aid of innovative experimental techniques and numerical simulations, as will be described in the next section. In the case of three-vortex systems the enhancement of the decay can be understood observing that the presence of three vortices reduces the possibility for all the vortices to rotate in the radial plane in such a way to avoid the collision. The probability of having a reconnection is then larger. A similar three-body effect was investigated in the case of 2D classical turbulence by Sire et al. 2011. The same is expected for systems with more than three vortices.

KZM Saturation

The enhancement of the decay in systems with more than three vortices can play a key role in the relaxation of turbulent phase of a BEC just after a temperature quench. In particular the decays measured above were used in Donadello, Serafini, Bienaimé, et al. 2016 to give an explanation for the saturation in the counting of Kibble-Zurek defects generated through a fast quench, as one can see from figure 4.2.

Limits of the Stroboscopic Technique

Many critical points limit the applicability of the μw-PMD technique to directly investigate collisions between vortices. The complexity of the implementation, required to keep the control on the effects of mean-field interaction between outcoupled atoms and the condensate, of the excitation of collective modes and of the SNR, makes the experiment not easy to manage and to adjust for different experimental conditions. Another drawback of this technique is the complete loss of information about the dynamics in the radial plane, which instead is crucial for understanding the vortex-vortex interaction mechanisms.

6.2.2 Characterization of 3D Vortex-vortex Interactions

The limits of the μw-PMD imaging technique had been bypassed with the developement and the implementation of the rf-SMD technique described in detail in section 4.2.3.

6.2.2.1 *Experimental Procedure*

For reducing the magnetic field experienced by the outcoupled atoms during their expansion and avoiding the excessive reduction of the absorption cross-section, the experiment was carried on in the shallow magnetic trap I_s, with frequencies $\omega_x/2\pi = 9.2\,\mathrm{Hz}$ and $\omega_\perp/2\pi = 92\,\mathrm{Hz}$. After the quench across the transition for triggering the defect formation (section 4.1.2) a successive decompression is performed as described in section 4.1.3. At this point the condensate contains about 2×10^7 atoms with a negligible thermal fraction ($T < 150\,\mathrm{nK}$, $T_c \approx 500\,\mathrm{nK}$). The quench ramp is chosen to trigger the formation of an average number of two defects during the probing time, starting about 250 ms after the transition ($700\,\mathrm{kHz\,s^{-1}} - 800\,\mathrm{kHz\,s^{-1}}$). The rf-SMD imaging technique is implemented to outcouple a small constant fraction of atoms ($\sim 1 \times 10^5$ atoms), corresponding to about 1% of the initial total number. Outcoupling is performed every 12 ms for 75 times, giving a total probing range of 900 ms. After the filtering and fitting stages, described in section 4.2.3, the experimental sequences reporting the axial dynamics of the vortices and their orientation in the radial plane are obtained. Some representative cases are reported in figure 6.7. The sequences are plotted with a monochromatic palette on the whole range of the residuals to highlight the trajectory of the vortices. Data are also plotted with a palette with different colors according to the sign of residuals in order to highlight the symmetry of the residual patterns, which code the orientation of the vortex.

6.2.2.2 *Numerical Simulations*

Simulations details

In order to provide a clear picture of the physical mechanism that governs the system, some numerical simulations were carried out by Luca Galantucci and Carlo Barenghi from Newcastle University.

Numerical simulations were performed integrating the 3D Gross-Pitaevskii equation at $T = 0$. The atom number in the simulation (4×10^5 atoms) is smaller than the experimental one because of limited computational resources. This implies a reduction of the ratio $\mathscr{R}_\perp/\xi$ by a factor of three with respect to the actual one in the experiment, but the essential features of the vortex-vortex interaction are unchanged. Vortices are imprinted on the wavefunction imposing a Padé density profile and a uniform 2π phase winding. The GPE is then evolved in imaginary time until a stationary solution is reached. Starting from this point the simulation proceeds in real time.

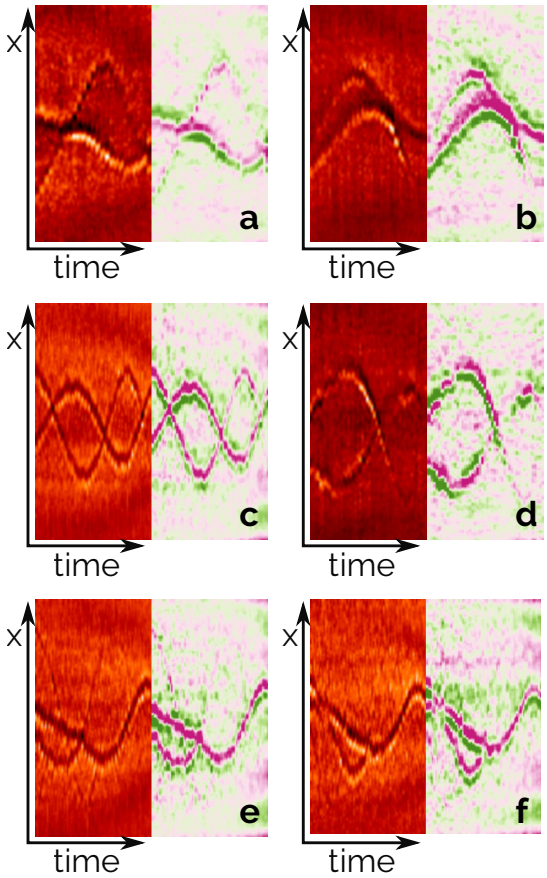

Figure 6.7: Selection of representative experimental sequences obtained through rf-SMD technique, reproducing the axial trajectories in the case of two approaching vortices.

Initial conditions

The initial conditions for the vortices, *i.e.*, their imprinting positions, are chosen to have the maximum dissimilarity with respect to a flat 2D system and to probe the role in the collisions for different values of the vortex relative velocity. The first point can be satisfied imprinting vortices that are initially orthogonal. Vortices are imprinted in radial planes at opposite axial positions $\pm x_0$ from the center. The tuning of the relative velocity can be done changing the value of x_0, corresponding to tune the orbit parameter χ. Simulations with one of the two perpendicular vortices imprinted in the center of the trap and with parallel vortices on different orbits were also performed.

Vortex evolution regimes

In figure 6.8 the results of the numerical simulations with different initial conditions are reported. The left part of figure 6.8 reports some radial and axial snapshots of the GP simulations, while on the right part the trajectories of the center of the two vortices are plotted as a function of the normalised time $\tau = t/T_0$, where T_0 is the precession period in the limit of vanishing amplitude (equation (5.8) in the limit $\chi \to 0$). When two vortices are imprinted in the system, their

evolution can be divided in two regimes, depending on their relative distance d:

- $d > \mathscr{R}_\perp$: the two vortices move almost independently along the elliptic orbit as discussed in section 5.2;
- $d \lesssim \mathscr{R}_\perp$: a significant 3D interaction between the two vortices occurs, the area highlighted with a gray shadow in the plots of figure 6.8 represents this regime.

After interacting the vortices return to move along elliptic orbits as independent vortices. They may be affected after the interaction by excitation of Kelvin waves or by a change of the rotational motion around the trap axis. During the second stage two different motions are present:

- an *axial motion*: axial projection of the precession dynamics, driven by the inhomogeneous density gradient of the sample. It is faster if vortices are closer to the boundary of the condensate (large χ);
- a *radial motion*: because of the tendency of the pair to arrange in the energy-conserving anti-parallel configuration through a rotation of the nodal lines in the radial plane. Such a rotation induces a radial drift of the vortices toward the center of the condensate, in analogy to the self-induced motion of a vortex-antivortex pair in a homogeneous system.

The balance between the two motions mentioned above determines the flavour of the interaction. Such a balance strongly depends on the parameters of the collision, *i.e.*, the entrance relative orientation of the nodal line in the radial plane θ_{rel} and their relative velocity v_{rel}. The effect of the radial motion is evident in figures 6.8 **(a-d)**.

6.2.2.3 *Interpretation of the Results*

The simulations show that in the case of a sufficiently high axial velocity (large χ) the two vortices tend to reconnect before the radial drift reaches the center of the condensate, as can be seen in figure 6.8 **(c)**. In this case the interaction occurs in a region close to the boundaries. On the other hand if the interaction occurs near the axis of the trap, *i.e.*, the two vortices have a small χ, the radial drift can be fast enough for vortices to get past the center of the condensate. In this case the change of the sign of the density gradient reverses the velocity field and the two vortices start to move axially away from each other, as represented in figure 6.8 **(a)**. Vortices with small relative velocity tend thus to *rebound* because of the important action of boundaries. Trajectories, in the case of rebounds, approach without touching, as can be observed in the plot of figure 6.8 **(a)**. Simulations

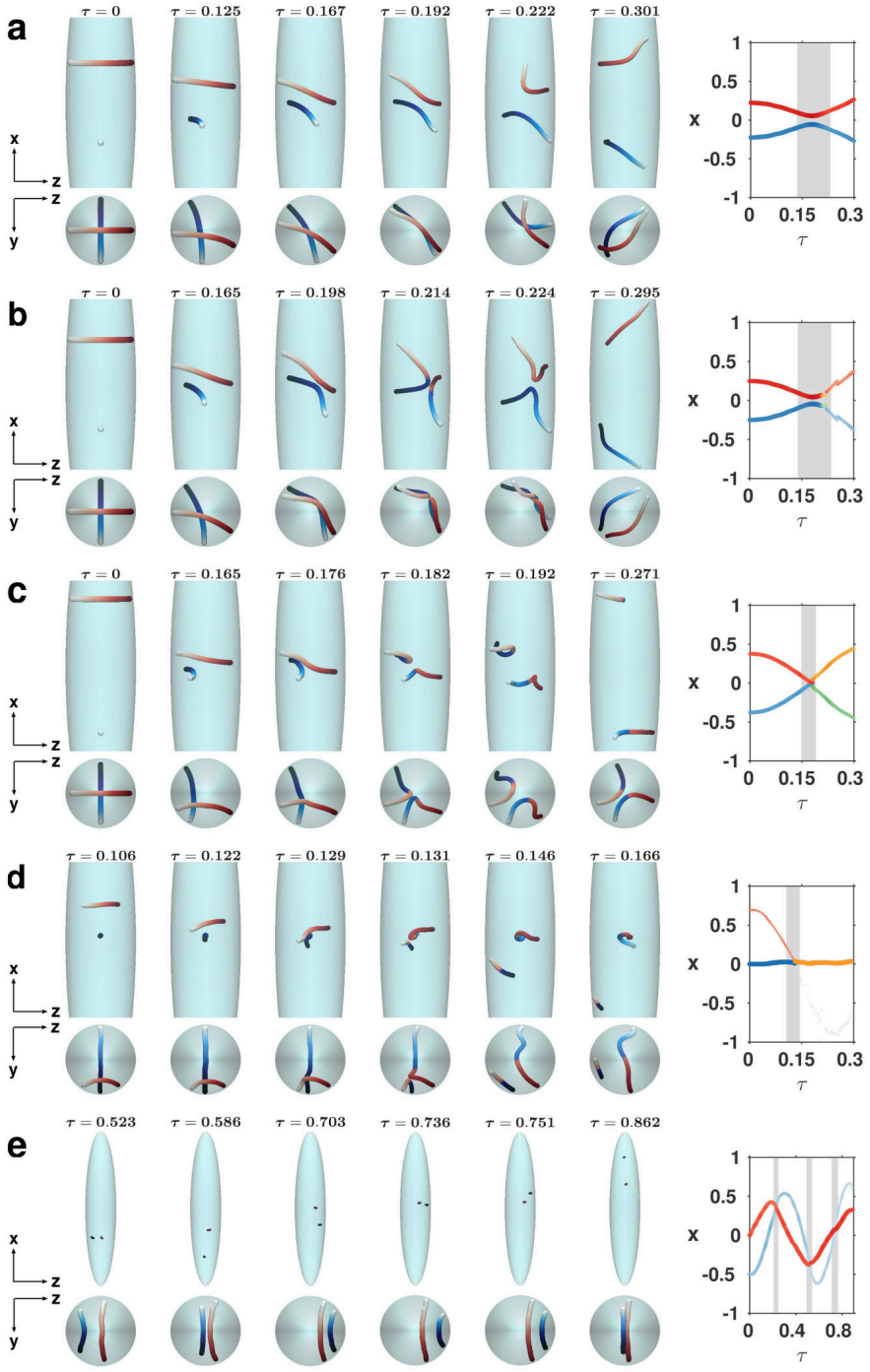

Figure 6.8: Snapshots of the numerical simulations performed by the Newcastle group.

suggest also the occurrence of an intermediate regime, where the interaction produces a *double reconnection* event. In such an event the relative distance between the vortices remains small for a longer time because the interplay of the axial motion and the radial drift. In this way the vortices have not enough time to axially separate after a first reconnection, and they undergo a successive reconnection. From a macroscopic point of view, the fast exchange of the vortex tails during the two successive reconnections makes this event very similar to a rebound, as one can see from the non-touching trajectories in figure 6.8 **(b)**. Multistep processes in the reconnection of vortex lines in a superfluid Fermi gas at unitarity were observed by Bulgac et al. 2011; their description does not however include any discussion about the role of the vortex velocity in these processes.

The link between numerical and experimental results can be done through a direct comparison of the experimental axial trajectories and the relative orientation angle with the numerical cases. Such a comparison is somewhat qualitative because the limited SNR in the residual profiles permits only a qualitative determination of the orientation angle, as pointed out in section 5.2.2.1. A more affordable analysis can be obtained through statistical considerations about the probability to observe a certain behaviour as a function of the relative velocity of the two vortices. The most clear criterion for the interpretation of the experimental sequences in figure 6.7 is the possible avoided crossing of the trajectories, which can be used to discriminate between rebounds and other cases. The experimental discrimination of double reconnections is actually not feasible, because of the similarity of the axial trajectory with rebounds and the impossibility to resolve the trajectories on the short time scale during which the process takes place. Another important feature is the visibility of a defect after an interaction event. An abrupt change of the visibility of the vortex signal after a crossing will be identified as *ejection*. In the numerical simulations of figure 6.8, the information about the visibility is rendered through a modulation of the thickness and the colour of the lines in the axial trajectory plots. Such a modulation is proportional to the TF density at the center of the vortex, which is a qualitative but effective way to map the visibility of a vortex. The information about the orientation of the vortex line in the radial plane cannot actually be extracted with a sufficiently high precision, nevertheless the qualitative information that can be inferred turns out to be useful in the interpretation of some particularly clean cases. The reliability of such an approach is justified on the basis of the analysis reported in section 4.2.3.1, where the qualitative accordance between the vortex orientation inferred from the asymmetric pattern of the residuals and the actual vortex orientation observed through axial imaging is demonstrated.

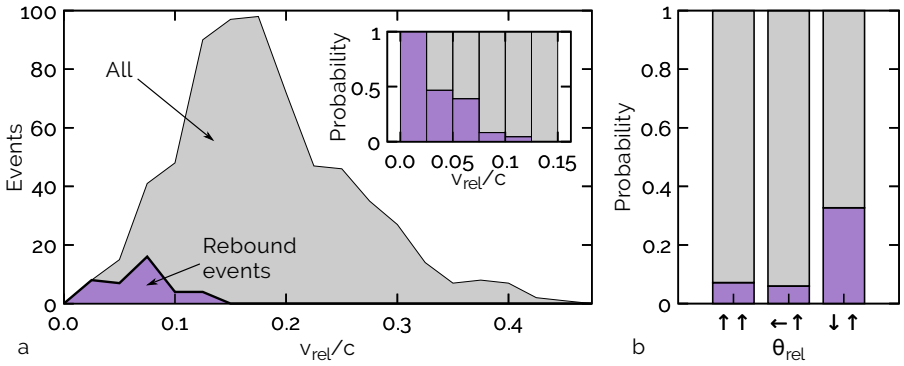

Figure 6.9: Statistical analysis of experimental data regarding rebound events.

REBOUNDS Taking the avoided axial crossing as a criterion for the recognition of rebounds, the cases reported in figure 6.7 **(a-b)** can be interpreted as rebound events. These images are also clear from the point of view of the determination of the relative orientation of the two vortices. In figure 6.7 **(b)** it is evident that, well before the interaction, the upper vortex signal shows a symmetric residual pattern, hence the vortex is vertical, while the lower one shows the asymmetric residual pattern of a horizontal vortex pointing to $-y$. After the interaction both vortices have the asymmetric pattern, but with opposite sign: the lower vortex keeps its orientation while the upper one is now oriented pointing to $+y$. The case of figure 6.7 **(a)** is a simpler event in which there is no rotational dynamics. In fact in this case the two vortices are already in the anti-parallel configuration, as it is evident from the opposite residual patterns. In this case the radial drift, which produces the bouncing, is due to a motion completely similar to the one observed for a vortex-antivortex pair in a flat system (Neely et al. 2010). One can also observe an increasing signal in the interaction region, which can be ascribed to the radial drift of the vortices to the center of the BEC where the density is higher, hence making the contrast stronger.

Statistical analysis

The main quantity that characterizes the occurrence of a rebound is the relative velocity of the two vortices. From the simulations we infer that rebounds are favoured when the axial dynamics is sufficiently slow to permit to the vortices to pass the center of the condensate in their radial drift. Hence rebounds occur more likely in the case of small orbit parameters. All the different experimental realizations were analysed measuring the relative axial velocity between the interacting vortices. They were classified according to the type of event through the trajectory argument introduced above. The results are reported in figure 6.9 **(a)**, where the relative velocity is normalised to the sound velocity in the center of the sample. One can notice that the events that are recognized as rebounds show a small relative velocity as expected, in particular the probability of observing a rebound in-

creases when the relative velocity decreases, as reported in the inset of figure 6.9 **(a)**, where the relative occurrence for each velocity bin is reported. To appreciate the role of the relative orientation angle in the rebound mechanism, the rebound probability as a function of the relative angle is reported in figure 6.9 **(b)**. Here the relative angle is classified into three limiting cases to which the residual pattern can be reduced in a qualitative way, *i.e.*, horizontal parallel vortices (↑↑), orthogonal vortices (←↑) and horizontal anti-parallel vortices (↓↑). The relative angle is qualitatively determined observing the residual pattern just before the interaction, when the two vortices have a relative distance $\sim \mathscr{R}_\perp$. The plot shows that rebounds mostly occur when vortices are anti-parallel, because they reached this situation through rotation in the radial plane or because they enter the collision already in that configuration. Cases of rebounds with different orientations can result from a not yet completed rotational dynamics or to distortions of the residual pattern due to the superposition of the signals relative to the two vortices.

ORBITING DYNAMICS When two vortices are parallel, they precess in the same direction around the center of the condensate. Their motion is only weakly disturbed by the interaction when they reach the minimum distance between the orbits. In this case the vortex signal in the experimental images seems to cross periodically without visible changes of the residual pattern and with at most slight modifications of their trajectories or in their visibility. In reality the vortices lie in opposite sides of the axial plane identified by their orbits. This case can be recognized in the experimental figure 6.7 **(c)**, and in the results of the numerical simulation reported in figure 6.8 **(e)**.

RECONNECTIONS Numerical simulations suggest the occurrence of reconnection when the orbit parameters of the colliding non parallel vortices are large. From figure 6.8 **(c-d)** it is evident that the reconnection processes cause the abrupt deformations of the vortex lines. From the experimental point of view such deformations cause a strong modification of the residual pattern, of the trajectory and of the visibility. The shape of the residual pattern obtained through rf-SMD of a strongly deformed vortex is not known, thus the information extracted after the event cannot be clearly interpreted. Experimental cases related to such a behaviour could be the ones reported in figure 6.7 **(d-e)**.

EJECTIONS An important point that must be addressed is the vanishing visibility (ejection) of the vortex signal that occurs for example in figures 6.7 **(e-f)**. Such a behaviour can be ascribed to the occurrence of an interaction between vortices very near to the condensate boundary. The interaction can cause the pushing of one or both vor-

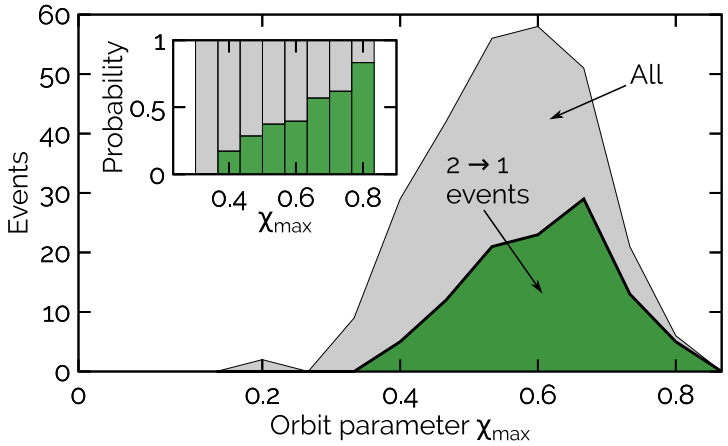

Figure 6.10: Statistical analysis of experimental data regarding ejection events.

tices toward external orbits. These orbits can lie in a region of very low density, and for this reason the visibility of the defects abruptly vanishes. A numerical example of ejection is shown in figure 6.8 **(d)**, where a reconnection process occurs and one of the product vortices lies in a very external orbit. Such a process can be the result both of a reconnection or of an orbiting dynamics, the key point is that the interaction happens in a region near the boundary. The case of figure 6.7 **(e)** is likely due to a reconnection process, because of the strong deviation of the trajectory of the vortex which remains visible after the collision and because the entrance orientation angles are different (symmetric pattern for the upper vortex and horizontal $-y$ for the bottom one). The presence of a third vortex with a very weak signal can be identified, but its presence does not affect the interaction process of the two other vortices because of their distance from it is large. The situation found in figure 6.7 **(f)** can be ascribed to an orbiting-induced ejection. The two vortices indeed show an equal residual pattern (horizontal $-y$).

Statistical analysis

As for the characterization of the rebound mechanism, also the ejection process was the subject of a statistical analysis. In figure 6.10 the distribution of the events as a function of the maximum orbit parameter χ_{max} in the pair of interacting vortices is shown. From such a distribution all the cases where rebounds occur are omitted. The green area represents the subset of events where at least one of the vortices shows a strong and abrubt reduction of visibility. As expected from the simulations and from the physical description of the system, ejection events occur with larger probability for larger χ_{max}. In the inset the relative occurrence of ejection per each bin is reported.

6.3 CONCLUSIONS AND PERSPECTIVES

In conclusion, we developed an innovative experimental technique, rf-SMD, which permits the characterization in real time of the position and the orientation of vortex lines in elongated BECs. Results obtained through this novel imaging method were combined with numerical simulations of the 3D GPE, permitting to recognize novel types of interaction regimes due to the 3D dynamics of vortex lines in an inhomogeneous system in the presence of boundaries. Such effects are, beside the ordinary reconnection, rebounds, double reconnections, unperturbed orbiting dynamics and abrupt changes of orbits with consequent dissipation of the vortex in the low-density region of the condensate (ejections). These processes are expected to be central in the dynamics of complex systems, such as discussed by Tsatsos et al. 2016 in the general framework of turbulence in the presence of boundaries.

A refined implementation of the rf-SMD technique for improving the SNR in the residual pattern will permit a more quantitative characterization of the different kinds of interaction events. Further analysis on the mechanisms of the swept extraction have to be performed through numerical simulations to characterize for example the effects on the pattern of bent vortices.

Part IV

APPENDIX

A SODIUM PROPERTIES

In this appendix some useful physical (tabel A.1) and optical (table A.3) properties relative to the D2 line of sodium can be found. The hyperfine structure of the D2 line is represented in figure A.1. All the data are taken from Steck 2010.

Table A.1: Sodium physical properties.

Quantity	Symbol	Value
Atomic number	Z	11
Total nucleons	$Z+N$	23
Relative natural abundance	$\eta(^{23}\mathrm{Na})$	100 %
Nuclear lifetime	τ_n	stable
Atomic mass	m	$3.817\,540\,35(19)\times10^{-24}$ kg
Density at 25 °C	ρ_m	$0.97\,\mathrm{g\,cm^{-3}}$
Melting point	T_M	97.8 °C
Boiling point	T_B	883 °C
Specific heat capacity	c_p	$1.228\,\mathrm{J\,g^{-1}\,K^{-1}}$
Molar heat capacity	C_p	$28.23\,\mathrm{J\,mol^{-1}\,K^{-1}}$
Vapor pressure at 25 °C	P_v	$2.38(12)\times10^{-11}$ torr
Nuclear spin	I	3/2
Ionization limit	E_I	5.139 076 50(28) eV

Table A.2: Sodium D_2 transition optical properties.

Quantity	Symbol	Value
Frequency	ω_A	$2\pi \cdot 508.848\,716\,2(13)$ THz
Energy	$\hbar\omega_A$	$2.104\,029\,011(51)$ eV
Wavelength in vacuum	λ_A	$589.158\,326\,4(15)$ nm
Wave number in vacuum	$k_A/2\pi$	$16\,973.366\,160(43)$ cm^{-1}
Lifetime	τ	$16.2492(77)$ ns
Natural line width	Γ	$2\pi \cdot 9.7946(46)$ MHz
Recoil velocity	v_{rec}	2.9461 cm s^{-1}
Recoil temperature	T_{rec}	$2.3998\,\mu$K
Doppler temperature	T_D	$235.03\,\mu$K
Dipole matrix element	$\langle J = \frac{1}{2} \Vert er \Vert J' = \frac{3}{2} \rangle$	$2.988\,31(100) \times 10^{-29}$ C m
Saturation intensity cycling transition ($\sigma_\pm$-polarized light)	I_s	$6.2600(21)$ mW cm^{-2}

Table A.3: Sodium D transition magnetic and electric field interaction parameters.

Quantity	Symbol	Value
Electron spin g-factor	g_S	$2.002\,319\,304\,362\,2(15)$
Electron orbital g-factor	g_L	$0.999\,976\,13$
Fine structure Landé g-factor	$g_J(3^2S_{1/2})$	$2.002\,296\,00(70)$
	$g_J(3^2P_{1/2})$	$0.665\,81(12)$
	$g_J(3^2P_{3/2})$	$1.334\,20(20)$
Nuclear g-factor	g_I	$-0.000\,804\,610\,80(80)$
Clock transition Zeeman shift	$\Delta\omega_{\text{clock}}/B^2$	$2\pi \cdot 2.2183$ kHz G^{-2}

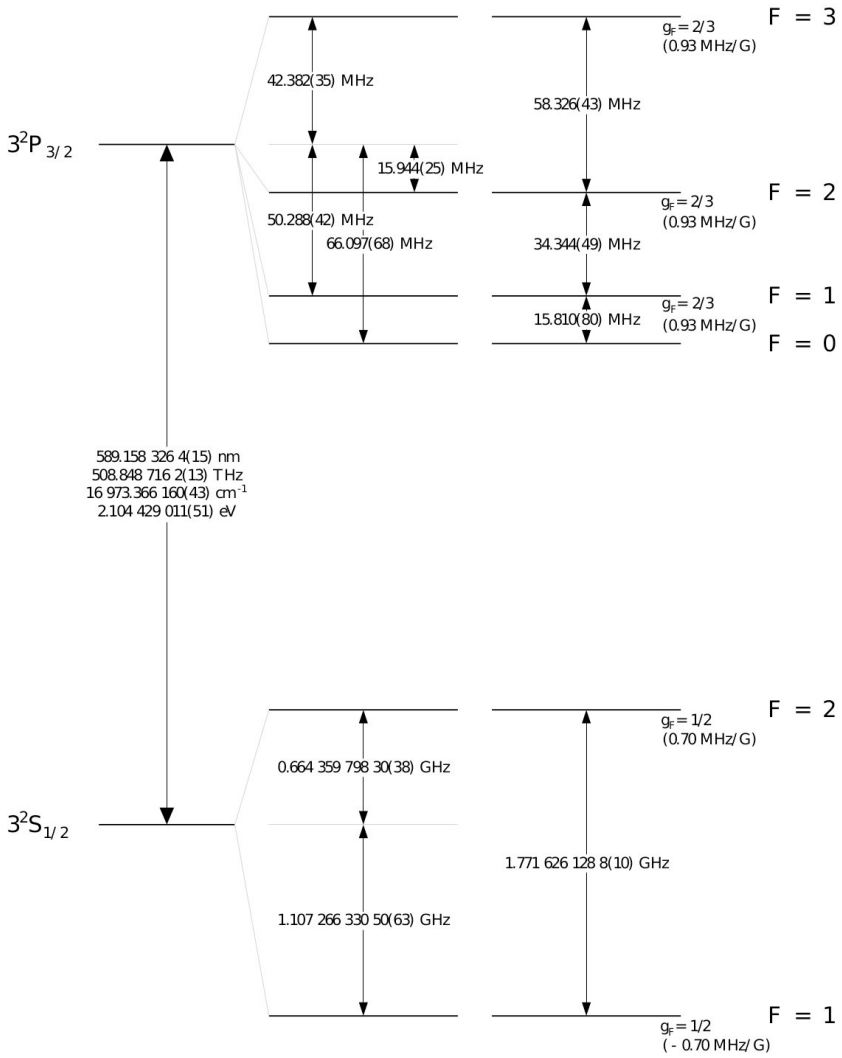

Figure A.1: Hyperfine structure of D_2 line of sodium. The g_F Landé factor for each level is indicated with the corresponding Zeeman shift between adjacent magnetic sublevels. From Steck 2010

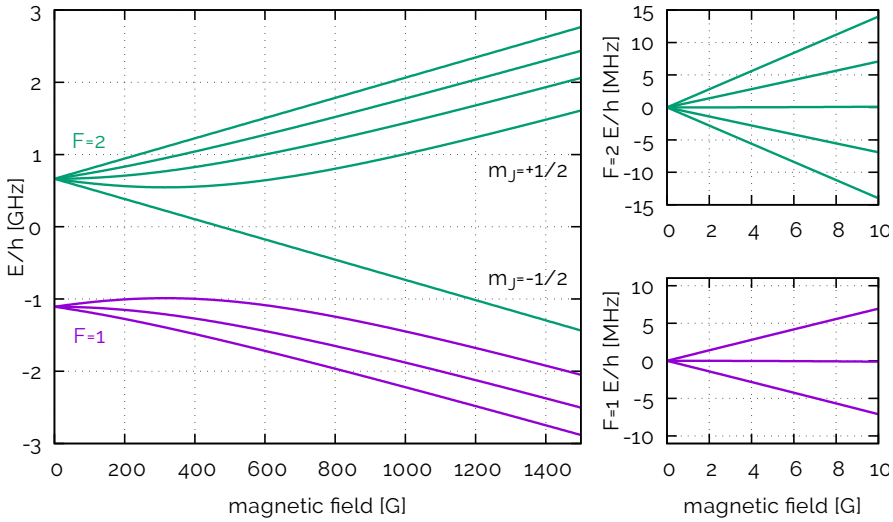

Figure A.2: Hyperfine structure of the $3^2S_{1/2}$ (ground) state of sodium in an exernal magnetic field. On the right the behaviours of the two states in a weak field are highlighted.

B LIST OF PUBLICATIONS

During the three years of the PhD career I co-authored the following articles giving a personal contribuion as detailed:

- Donadello S., Serafini S., Tylutki M., Pitaevskii L.P., Dalfovo F., Lamporesi G. and Ferrari G. "Observation of Solitonic Vortices in Bose-Einstein Condensates", *Phys. Rev. Lett.* **113**, 065302 (2014): preparation of the experimental setup, data acquisition and analysis, discussion of the results and manuscript writing;

- Tylutki M., Donadello S., Serafini S., Pitaevskii L.P., Dalfovo F., Lamporesi G. and Ferrari G. "Solitonic Vortices in Bose-Einstein Condensates", *Eur. Phys. J. Special Topics* **224**, 577 (2015): preparation of the experimental setup, data acquisition and analysis and discussion of the results;

- Serafini S., Barbiero M., Debortoli M., Donadello S., Larcher F., Dalfovo F., Lamporesi G. and Ferrari G. "Dynamics and interaction of vortex lines in an elongated Bose-Einstein condensate", *Phys. Rev. Lett.* **115**, 170402 (2015): preparation of the experimental setup, data acquisition and analysis, discussion of the results and manuscript writing;

- Colzi G., Durastante G., Fava E., Serafini S., Lamporesi G. and Ferrari G. "Sub-Doppler cooling of sodium atoms in gray molasses", *Phys. Rev. A* **93**, 023421 (2016): assistance in technical preparation of the experimental setup and discussion of the results;

- Donadello S., Serafini S., Bienaimé T., Dalfovo F., Lamporesi G. and Ferrari G. "Creation and counting of defects in a temperature quenched Bose-Einstein Condensate", *Phys. Rev. A* **94**, 023628 (2016): assistance in data acquisition and discussion of the results;

- Bienaimé T., Fava E., Colzi G., Mordini C., Serafini S., Qu C., Stringari S., Lamporesi G, and Ferrari G. "Spin-Dipole Oscillation and Polarizability of a Binary Bose-Einstein Condensate near the Miscible-Immiscible Phase Transition", *Phys. Rev. A* **94**, 063652 (2016): assistance in technical preparation of the experimental setup and discussion of the results.

- Serafini S., Galantucci L., Iseni E., Bienaimé T., Bisset R.N., Barenghi C.F., Dalfovo F., Lamporesi G. and Ferrari G. "Vortex reconnections and rebounds in trapped atomic Bose-Einstein Condensates", arXiv:1611.01691 preprint (2016): preparation of the experimental setup, data acquisition and analysis, discussion of the results and manuscript writing.

BIBLIOGRAPHY

Abo-Shaeer, J.R. et al. (2001). "Observation of Vortex Lattices in Bose-Einstein Condensates". In: *Science* 292, pp. 476–479 (cit. on pp. 22, 107).

Agrawal, G. P. (2002). *Fiber Optic Communication Systems*. Wiley (cit. on p. 39).

Allen, J. F. and A. D. Misener (1938). "Flow of Liquid Helium II". In: *Nature* 141, p. 75 (cit. on pp. ix, 10).

Andersen, M. F. et al. (2006). "Quantized Rotation of Atoms from Photons with Orbital Angular Momentum". In: *Phys. Rev. Lett.* 97 (17), p. 170406 (cit. on p. 23).

Anderson, B. P., P. C. Haljan, C. A. Regal, et al. (2001). "Watching Dark Solitons Decay into Vortex Rings in a Bose-Einstein Condensate". In: *Phys. Rev. Lett.* 86 (14), pp. 2926–2929 (cit. on p. 24).

Anderson, B. P., P. C. Haljan, C. E. Wieman, et al. (2000). "Vortex Precession in Bose-Einstein Condensates: Observations with Filled and Empty Cores". In: *Phys. Rev. Lett.* 85 (14), pp. 2857–2860 (cit. on p. 107).

Anderson, M. H. et al. (1995). "Observation of Bose-Einstein condensation in a dilute atomic vapor". In: *Science* 269.5221, pp. 198–201 (cit. on p. 4).

Andrews, M. R. et al. (1997). "Propagation of Sound in a Bose-Einstein Condensate". In: *Phys. Rev. Lett.* 79 (4), pp. 553–556 (cit. on pp. 29, 60).

Anglin, J. R. (2002). "Vortices near surfaces of Bose-Einstein condensates". In: *Phys. Rev. A* 65 (6), p. 063611 (cit. on pp. 88, 94).

Berry, M. V. and M. R. Dennis (2012). "Reconnections of wave vortex lines". In: *Eur. J. Phys.* 33.3, p. 723 (cit. on p. 113).

Bewley, G. P. et al. (2008). "Characterization of reconnecting vortices in superfluid helium". In: *Proc. Natl. Acad. Sci. U.S.A.* 105, p. 13707 (cit. on p. 107).

Bloch, I., J. Dalibard, and S. Nascimbène (2012). "Quantum simulations with ultracold quantum gases". In: *Nat. Pyhs.* 8, p. 267 (cit. on p. 5).

Bloch, I., T. W. Hänsch, and T. Esslinger (1999). "Atom Laser with a cw Output Coupler". In: *Phys. Rev. Lett.* 82 (15), pp. 3008–3011 (cit. on p. 72).

– (2000). "Measurement of the spatial coherence of a trapped Bose gas at the phase transition". In: *Nature* 403.6766, pp. 166–170 (cit. on p. 75).

Bolda, E. L. and D. F. Walls (1998). "Detection of Vorticity in Bose-Einstein Condensed Gases by Matter-Wave Interference". In: *Phys. Rev. Lett.* 81 (25), pp. 5477–5480 (cit. on pp. 29, 60).

Brand, J. and W. P. Reinhardt (2002). "Solitonic vortices and the fundamental modes of the snake instability: Possibility of observation in the gaseous Bose-Einstein condensate". In: *Phys. Rev. A* 65 (4), p. 043612 (cit. on pp. 84, 85).

Bulgac, A. et al. (2011). "Real-Time Dynamics of Quantized Vortices in a Unitary Fermi Superfluid". In: *Science* 332.6035, pp. 1288–1291 (cit. on p. 118).

Carr, L. D. and J. Brand (2007). "Multidimensional Solitons: Theory". In: *Chapter 7 in "Emergent Nonlinear Phenomena in Bose-Einstein Condensates: Theory and Experiment," edited by P. G. Kevrekidis, D. J. Frantzeskakis, and R. Carretero-Gonzalez* (cit. on p. 85).

Carusotto, I. and C. Ciuti (2013). "Quantum fluids of light". In: *Rev. Mod. Phys.* 85 (1), pp. 299–366 (cit. on p. 4).

Castin, Y. and R. Dum (1996). "Bose-Einstein Condensates in Time Dependent Traps". In: *Phys. Rev. Lett.* 77 (27), pp. 5315–5319 (cit. on pp. 59, 90).

Chevy, F. (2007). "Vortices in Bose–Einstein Condensates: Experiments". In: *Chapter 10 in "Emergent Nonlinear Phenomena in Bose-Einstein Condensates: Theory and Experiment," edited by P. G. Kevrekidis, D. J. Frantzeskakis, and R. Carretero-Gonzalez* (cit. on pp. 22, 30).

Chevy, F., K. W. Madison, V. Bretin, et al. (2001). "Interferometric detection of a single vortex in a dilute Bose-Einstein condensate". In: *Phys. Rev. A* 64 (3), p. 031601 (cit. on pp. 29, 61).

Chevy, F., K. W. Madison, and J. Dalibard (2000). "Measurement of the Angular Momentum of a Rotating Bose-Einstein Condensate". In: *Phys. Rev. Lett.* 85 (11), pp. 2223–2227 (cit. on p. 31).

Choi, J., S. W. Seo, and Y. Shin (2013). "Observation of Thermally Activated Vortex Pairs in a Quasi-2D Bose Gas". In: *Phys. Rev. Lett.* 110 (17), p. 175302 (cit. on p. 24).

Chomaz, L. et al. (2015). "Emergence of coherence via transverse condensation in a uniform quasi-two-dimensional Bose gas". In: *Nat. Commun.* 6, p. 6162 (cit. on p. 25).

Coddington, I. et al. (2003). "Observation of Tkachenko Oscillations in Rapidly Rotating Bose-Einstein Condensates". In: *Phys. Rev. Lett.* 91 (10), p. 100402 (cit. on p. 107).

Cohen-Tannoudji, C. and D. Guéry-Odelin (2011). *Advances in Atomic Physics, An Overview*. Singapore: World Scientific (cit. on pp. 5, 17, 37, 53).

Colzi, G. et al. (2016). "Sub-Doppler cooling of sodium atoms in gray molasses". In: *Phys. Rev. A* 93.023421 (cit. on p. 53).

Corman, L. et al. (2014). "Quench-Induced Supercurrents in an Annular Bose Gas". In: *Phys. Rev. Lett.* 113 (13), p. 135302 (cit. on pp. 25, 29, 30).

Dalfovo, F. et al. (1999). "Theory of Bose-Einstein condensation in trapped gases". In: *Rev. Mod. Phys.* 71 (3), pp. 463–512 (cit. on pp. 5, 10, 16).

Davis, K. B. et al. (1995). "Bose-Einstein Condensation in a Gas of Sodium Atoms". In: *Phys. Rev. Lett.* 75 (22), pp. 3969–3973 (cit. on pp. 4, 37).

Davis, R. L. and E. P. S. Shellard (1989). "Global strings and superfluid vortices". In: *Phys. Rev. Lett.* 63 (19), pp. 2021–2024 (cit. on p. 113).

De Waele, A.T.A.M. and R.G.K.M. Aarts (1994). "Route to vortex reconnection". In: *Physical Review Letters* 72.4, p. 482 (cit. on p. 107).

Demokritov, S. O. et al. (2013). "Bose-Einstein condensation of quasi-equilibrium magnons at room temperature under pumping". In: *Nature* 443, pp. 430–433 (cit. on p. 4).

Denschlag, J. et al. (2000). "Generating Solitons by Phase Engineering of a Bose-Einstein Condensate". In: *Science* 287.5450, pp. 97–101 (cit. on p. 24).

Dobrek, Ł. et al. (1999). "Optical generation of vortices in trapped Bose-Einstein condensates". In: *Phys. Rev. A* 60 (5), R3381–R3384 (cit. on pp. 60, 61).

Donadello, S., S. Serafini, T. Bienaimé, et al. (2016). "Creation and counting of defects in a temperature-quenched Bose-Einstein condensate". In: *Phys. Rev. A* 94 (2), p. 023628 (cit. on pp. 25, 54, 86, 113).

Donadello, S., S. Serafini, M. Tylutki, et al. (2014). "Observation of Solitonic Vortices in Bose-Einstein Condensates". In: *Phys. Rev. Lett.* 113 (6), p. 065302 (cit. on pp. 84, 87, 91, 92, 112).

Engels, P., I. Coddington, P. C. Haljan, and E. A. Cornell (2002). "Nonequilibrium Effects of Anisotropic Compression Applied to Vortex Lattices in Bose-Einstein Condensates". In: *Phys. Rev. Lett.* 89, p. 100403 (cit. on p. 107).

Engels, P., I. Coddington, P. C. Haljan, V. Schweikhard, et al. (2003). "Observation of Long-Lived Vortex Aggregates in Rapidly Rotating Bose-Einstein Condensates". In: *Phys. Rev. Lett.* 90 (17), p. 170405 (cit. on p. 23).

Fetter, A. L. and J.-k. Kim (2001). "Vortex precession in a rotating nonaxisymmetric trapped Bose-Einstein condensate". In: *J. Low Temp. Phys.* 125.5/6, p. 239 (cit. on pp. 95, 96).

Fetter, A. L. and A. A. Svidzinsky (2001). "Vortices in a trapped dilute Bose-Einstein condensate". In: *Journal of Physics: Condensed Matter* 13.12, R135 (cit. on p. 87).

Fetter, A.L. (2009). "Rotating trapped Bose-Einstein condensates". In: *Rev. Mod. Phys.* 81, p. 647 (cit. on pp. 18, 95, 107).

Feynman, R. P. (1982). "Simulating Physics with Computers". In: *International Journal of Theoretical Physics* 21 (6-7), pp. 467–488 (cit. on p. 5).

Feynman, R.P., R.B. Leighton, and M.L. Sands (1963). *The Feynman Lectures on Physics*. The Feynman Lectures on Physics v. 1. Addison-Wesley (cit. on p. x).

Fonda, E. et al. (2014). "Direct observation of Kelvin waves excited by quantized vortex reconnection". In: *Proc. Nat. Acad. Sci.* 111.Supplement 1, pp. 4707–4710 (cit. on pp. 15, 106, 107).

Freilich, D. V. et al. (2010). "Real-Time Dynamics of Single Vortex Lines and Vortex Dipoles in a Bose-Einstein Condensate". In: *Science* 329, p. 1182 (cit. on pp. 25, 28, 64, 65, 107).

García-Ripoll, J.J. and V.M. Pérez-García (2001a). "Vortex bending and tightly packed vortex lattices in Bose-Einstein condensates". In: *Phys. Rev. A* 64, p. 053611 (cit. on p. 95).

– (2001b). "Vortex nucleation and hysteresis phenomena in rotating Bose-Einstein condensates". In: *Phys. Rev. A* 63, 041603(R) (cit. on p. 95).

Georgescu, I. M., S. Ashhab, and F. Nori (2014). "Quantum simulation". In: *Rev. Mod. Phys.* 86 (1), pp. 153–185 (cit. on p. 5).

Gott, Y. V., M. S. Ioffe, and V. G. Telkovsij (1962). In: *Nuclear Fusion Supplement* 3.1045 (cit. on p. 42).

Hadzibabic, Z. et al. (2006). "Berezinskii–Kosterlitz–Thouless crossover in a trapped atomic gas". In: *Nature* 441.7097, pp. 1118–1121 (cit. on pp. 29, 31).

Haljan, P. C. et al. (2001). "Use of Surface-Wave Spectroscopy to Characterize Tilt Modes of a Vortex in a Bose-Einstein Condensate". In: *Phys. Rev. Lett.* 86 (14), pp. 2922–2925 (cit. on p. 22).

Hodby, E., G. Hechenblaikner, et al. (2001). "Vortex Nucleation in Bose-Einstein Condensates in an Oblate, Purely Magnetic Potential". In: *Phys. Rev. Lett.* 88 (1), p. 010405 (cit. on p. 22).

Hodby, E., S. A. Hopkins, et al. (2003). "Experimental Observation of a Superfluid Gyroscope in a Dilute Bose-Einstein Condensate". In: *Phys. Rev. Lett.* 91 (9), p. 090403 (cit. on p. 31).

Inouye, S. et al. (2001). "Observation of Vortex Phase Singularities in Bose-Einstein Condensates". In: *Phys. Rev. Lett.* 87 (8), p. 080402 (cit. on pp. 23, 29, 61).

Jackson, B., J.F. McCann, and C.S. Adams (1999). "Vortex line and ring dynamics in trapped Bose-Einstein condensates". In: *Phys. Rev. A* 61, p. 013604 (cit. on p. 95).

Kapitza, P. L. (1938). "Viscosity of Liquid Helium below the -Point". In: *Nature* 141, p. 74 (cit. on pp. ix, 10).

Kerr, R. M. (2011). "Vortex stretching as a mechanism for quantum kinetic energy decay". In: *Physical review letters* 106.22, p. 224501 (cit. on p. 107).

Ketterle, W., K.B. Davis, et al. (1993). "High densities of cold atoms in a dark spontaneous-force optical trap". In: *Physical review letters* 70.15, pp. 2253–2256 (cit. on p. 52).

Ketterle, W., D. S. Durfee, and D. M. Stamper-Kurn (1999). "Making, probing and understanding Bose-Einstein condensates". In: *Bose-Einstein Condensation in Atomic Gases*. Ed. by M. Inguscio, Stringari S., and C. E. Wieman. Proceedings of the International School of Physics "Enrico Fermi", Course CXL (cit. on pp. 3, 23, 26, 42, 54).

Kevrekidis, P.G., D.J. Frantzeskakis, and R. Carretero-González (2007). *Emergent Nonlinear Phenomena in Bose-Einstein Condensates: Theory and Experiment*. Springer Series on Atomic, Optical, and Plasma Physics. Springer Berlin Heidelberg (cit. on p. 19).

Kibble, T.W.B. (1976). "Topology of cosmic domains and strings". In: *J. Phys. A* 9.8, p. 1387 (cit. on p. 24).

Komineas, S. and N. Papanicolaou (2003). "Solitons, solitonic vortices, and vortex rings in a confined Bose-Einstein condensate". In: *Phys. Rev. A* 68 (4), p. 043617 (cit. on pp. 84, 85).

Koplik, J. and H. Levine (1993). "Vortex reconnection in superfluid helium". In: *Phys. Rev. Lett.* 71 (9), pp. 1375–1378 (cit. on p. 107).

Kozuma, M. et al. (1999). "Coherent Splitting of Bose-Einstein Condensed Atoms with Optically Induced Bragg Diffraction". In: *Phys. Rev. Lett.* 82 (5), pp. 871–875 (cit. on p. 61).

Ku, M. J. H., W. Ji, et al. (2014). "Motion of a Solitonic Vortex in the BEC-BCS Crossover". In: *Phys. Rev. Lett.* 113 (6), p. 065301 (cit. on pp. 24, 95, 96).

Ku, M. J. H., B. Mukherjee, et al. (2016). "Cascade of Solitonic Excitations in a Superfluid Fermi gas: From Planar Solitons to Vortex Rings and Lines". In: *Phys. Rev. Lett.* 116 (4), p. 045304 (cit. on p. 86).

Kwon, W. J., J. H. Kim, et al. (2016). "Observation of von Kármán Vortex Street in an Atomic Superfluid Gas". In: *Phys. Rev. Lett.* 117 (24), p. 245301 (cit. on p. 23).

Kwon, W. J., G. Moon, et al. (2014). "Relaxation of superfluid turbulence in highly oblate Bose-Einstein condensates". In: *Phys. Rev. A* 90 (6), p. 063627 (cit. on pp. 23, 107).

Lamporesi, G., S. Donadello, S. Serafini, F. Dalfovo, et al. (2013). "Spontaneous creation of Kibble-Zurek solitons in a Bose-Einstein condensate". In: *Nat. Phys.* 9.10, pp. 656–660 (cit. on pp. 25, 83, 84, 86, 112).

Lamporesi, G., S. Donadello, S. Serafini, and G. Ferrari (2013). "Compact high-flux source of cold sodium atoms". In: *Rev. Sci. Instrum.* 84.6, p. 063102 (cit. on pp. 41, 55).

Leanhardt, A. E. et al. (2002). "Imprinting Vortices in a Bose-Einstein Condensate using Topological Phases". In: *Phys. Rev. Lett.* 89 (19), p. 190403 (cit. on p. 23).

Lighthill, M. J. (1956). "Physics of gas flow at very high speeds". In: *Nature* 178.4529, p. 343 (cit. on p. ix).

Madison, K. W. et al. (2000). "Vortex Formation in a Stirred Bose-Einstein Condensate". In: *Phys. Rev. Lett.* 84 (5), pp. 806–809 (cit. on pp. 22, 107).

Majorana, E. (1932). "Atomi orientati in campo magnetico variabile". In: *Nuovo Cimento* 9.43 (cit. on p. 42).

Mason, P., N. G. Berloff, and A. L. Fetter (2006). "Motion of a vortex line near the boundary of a semi-infinite uniform condensate". In: *Physical Review A* 74.4, p. 043611 (cit. on p. 94).

Massignan, P. and M. Modugno (2003). "One-dimensional model for the dynamics and expansion of elongated Bose-Einstein condensates". In: *Phys. Rev. A* 67 (2), p. 023614 (cit. on p. 90).

Matthews, M. R. et al. (1999). "Vortices in a Bose-Einstein Condensate". In: *Phys. Rev. Lett.* 83 (13), pp. 2498–2501 (cit. on p. 21).

Meystre, P. (2001). *Atom Optics*. New York: Springer (cit. on p. 42).

Middelkamp, S et al. (2011). "Guiding-center dynamics of vortex dipoles in Bose-Einstein condensates". In: *Phys. Rev. A* 84, 011605(R) (cit. on p. 107).

Migdal, A. B. (1959). "Superfluidity and the moments of inertia of nuclei". In: *Nuclear Physics* 13 (5), pp. 655–674 (cit. on p. 4).

Modugno, M., L. Pricoupenko, and Y. Castin (2003). "Bose-Einstein condensates with a bent vortex in rotating traps". In: *Eur. Phys. J. D* 22.2, pp. 235–257 (cit. on p. 95).

Muniz, S. R., D. S. Naik, and C. Raman (2006). "Bragg spectroscopy of vortex lattices in Bose-Einstein condensates". In: *Phys. Rev. A* 73 (4), p. 041605 (cit. on pp. 29, 32).

Muñoz Mateo, A. and J. Brand (2014). "Chladni Solitons and the Onset of the Snaking Instability for Dark Solitons in Confined Superfluids". In: *Phys. Rev. Lett.* 113 (25), p. 255302 (cit. on pp. 85, 86).

Navarro, R. et al. (2013). "Dynamics of a Few Corotating Vortices in Bose-Einstein Condensates". In: *Phys. Rev. Lett.* 110 (22), p. 225301 (cit. on p. 107).

Navon, N. et al. (2015). "Critical dynamics of spontaneous symmetry breaking in a homogeneous Bose gas". In: *Science* 347.6218, pp. 167–170 (cit. on p. 25).

Nazarenko, S. and R. West (2003). "Analytic solution for nonlinear Schrödinger vortex reconnection". In: *J. Low Temp. Phys.* 132 (1/2), p. 1 (cit. on p. 107).

Neely, T. W. et al. (2010). "Observation of Vortex Dipoles in an Oblate Bose-Einstein Condensate". In: *Phys. Rev. Lett.* 104 (16), p. 160401 (cit. on pp. 23, 107, 119).

Nevsky, A.Yu. et al. (2008). "A narrow-line-width external cavity quantum dot laser for high-resolution spectroscopy in the near-infrared and yellow spectral ranges". English. In: *Applied Physics B* 92 (4), pp. 501–507 (cit. on p. 38).

Nikuni, T. et al. (2000). "Bose-Einstein Condensation of Dilute Magnons in $TlCuCl_3$". In: *Phys. Rev. Lett.* 84 (25), pp. 5868–5871 (cit. on p. 4).

Parker, N. (2004). "Numerical Studies of Vortices and Dark Solitons in Atomic Bose-Einstein Condensates". PhD thesis. University of Durham (cit. on pp. 84, 85, 89, 95, 108).

Parker, N. G. et al. (2007). "Vortices in Bose–Einstein Condensates: Theory". In: *Chapter 9 in "Emergent Nonlinear Phenomena in Bose-Einstein Condensates: Theory and Experiment," edited by P. G. Kevrekidis, D. J. Frantzeskakis, and R. Carretero-Gonzalez* (cit. on pp. 15, 112).

Pitaevskii, L. and S. Stringari (2016). *Bose-Einstein Condensation and Superfluidity*. Oxford University Press (cit. on p. 5).

Pitaevskii, L.P. (2013). "Hydrodynamic theory of motion of quantized vortex rings in trapped superfluid gases". In: *arXiv:1311.4693v1* (cit. on p. 95).

Pritchard, D. E. (1983). "Cooling Neutral Atoms in a Magnetic Trap for Precision Spectroscopy". In: *Phys. Rev. Lett.* 51 (15), pp. 1336–1339 (cit. on p. 42).

Proukakis, N. (2016). "Private communication" (cit. on pp. 55, 86, 109, 110).

Proukakis, N. P. (2007). "Beyond Gross-Pitaevskii Mean-Field Theory". In: *Chapter 18 in "Emergent Nonlinear Phenomena in Bose-Einstein Condensates: Theory and Experiment," edited by P. G. Kevrekidis, D. J. Frantzeskakis, and R. Carretero-Gonzalez* (cit. on p. 17).

Ramanathan, A. et al. (2012). "Partial-transfer absorption imaging: A versatile technique for optimal imaging of ultracold gases". In: *Review of Scientific Instruments* 83.8, 083119 (cit. on pp. 28, 64).

Roberts, P. H. and N. G. Berloff (2001). "The nonlinear Schrödinger equation as a model of superfluidity". In: *Quantized vortex dynamics and superfluid turbulence*. Springer Berlin Heidelberg, pp. 235–257 (cit. on p. 106).

Scherer, D. R. et al. (2007). "Vortex Formation by Merging of Multiple Trapped Bose-Einstein Condensates". In: *Phys. Rev. Lett.* 98 (11), p. 110402 (cit. on p. 24).

Schwarz, K. W. (1988). "Three-dimensional vortex dynamics in superfluid ^{4}He: Homogeneous superfluid turbulence". In: *Phys. Rev. B* 38 (4), pp. 2398–2417 (cit. on pp. 17, 106).

Schweikhard, V., S. Tung, and E. A. Cornell (2007). "Vortex Proliferation in the Berezinskii-Kosterlitz-Thouless Regime on a Two-Dimensional Lattice of Bose-Einstein Condensates". In: *Phys. Rev. Lett.* 99 (3), p. 030401 (cit. on p. 24).

Seo, S. W. et al. (2016). "Probing 2D Quantum Turbulence in Atomic Superfluid Gas using Bragg Scattering". In: *arXiv preprint arXiv:1610.06635* (cit. on pp. 29, 32).

Serafini, S. et al. (2015). "Dynamics and interaction of vortex lines in an elongated Bose-Einstein condensate". In: *Phys. Rev. Lett.* 115.17, p. 170402 (cit. on pp. 84, 111, 113).

Sheehy, D.E. and L. Radzihovsky (2004). "Vortices in spatially inhomogeneous superfluids". In: *Phys. Rev. A* 70, p. 063620 (cit. on p. 94).

Sire, C., P. Chavanis, and J. Sopik (2011). "Effective merging dynamics of two and three fluid vortices: Application to two-dimensional decaying turbulence". In: *Phys. Rev. E* 84 (5), p. 056317 (cit. on p. 113).

Stam, K. M. R. van der et al. (2007). "Large atom number Bose-Einstein condensate of sodium". In: *Review of Scientific Instruments* 78.1, 013102 (cit. on p. 37).

Steck, D. A. (2010). *Sodium D Line Data*. revision 2.1.4, 23 December 2010. URL: http://steck.us/alkalidata (cit. on pp. 125, 127).

Stringari, S. (2001). "Superfluid Gyroscope with Cold Atomic Gases". In: *Phys. Rev. Lett.* 86 (21), pp. 4725–4728 (cit. on p. 31).

Svidzinsky, A.A. and A.L. Fetter (2000). "Stability of a Vortex in a Trapped Bose-Einstein Condensate". In: *Phys. Rev. Lett.* 84, p. 5919 (cit. on p. 95).

Tebbs, R., A. J. Youd, and C. F. Barenghi (2011). "The approach to vortex reconnection". In: *Journal of Low Temperature Physics* 162.3-4, pp. 314–321 (cit. on p. 107).

Tsatsos, M. C. et al. (2016). "Quantum turbulence in trapped atomic Bose–Einstein condensates". In: *Physics Reports* 622, pp. 1–52 (cit. on p. 122).

Tylutki, M. et al. (2015). "Solitonic vortices in Bose-Einstein condensates". In: *Eur. Phys. J. Special Topics* 224.3, pp. 577–583 (cit. on p. 88).

Verbiest, G. J. and A. Achúcarro (2011). "High speed collision and reconnection of Abelian Higgs strings in the deep type-II regime". In: *Phys. Rev. D* 84 (10), p. 105036 (cit. on p. 113).

Weiler, C. N. et al. (2008). "Spontaneous vortices in the formation of Bose-Einstein condensates". In: *Nature* 455, pp. 948–952 (cit. on pp. 25, 107).

Wright, K. C. et al. (2013). "Driving Phase Slips in a Superfluid Atom Circuit with a Rotating Weak Link". In: *Phys. Rev. Lett.* 110 (2), p. 025302 (cit. on p. 23).

Yefsah, T. et al. (2013). "Heavy solitons in a fermionic superfluid". In: *Nature* 499, p. 426 (cit. on p. 84).

Zambelli, F. and S. Stringari (1998). "Quantized Vortices and Collective Oscillations of a Trapped Bose-Einstein Condensate". In: *Phys. Rev. Lett.* 81 (9), pp. 1754–1757 (cit. on p. 31).

Zobay, O. and B. M. Garraway (2001). "Two-Dimensional Atom Trapping in Field-Induced Adiabatic Potentials". In: *Phys. Rev. Lett.* 86 (7), pp. 1195–1198 (cit. on p. 67).

Zuccher, S. et al. (2012). "Quantum vortex reconnections". In: *Phys. of Fluids* 24, p. 125108 (cit. on p. 107).

Zurek, W. H. (1985). "Cosmological experiments in superfluid liquid helium?" In: *Nature* 317, pp. 505–508 (cit. on p. 24).

– (2009). “Causality in Condensates: Gray Solitons as Relics of BEC Formation”. In: *Phys. Rev. Lett.* 102 (10), p. 105702 (cit. on p. 83).